

Probing Microstructure and Optical Properties of Organic Semiconductor Thin Films

Shubham Bhagat

A Thesis
In the Department of
Physics

Presented in Partial Fulfillment of the Requirements
For the Degree of
Doctor of Philosophy (Physics) at
Concordia University
Montréal, Québec, Canada

November 2024

©Shubham Bhagat, 2024

CONCORDIA UNIVERSITY
SCHOOL OF GRADUATE STUDIES

This is to certify that the thesis prepared

By: Shubham Bhagat

Entitled: Probing Microstructure and Optical Properties of
Organic Semiconductor Thin Films

and submitted in partial fulfillment of the requirements for the degree of

Doctor of Philosophy (Physics)

complies with the regulations of the University and meets the accepted standards with respect to originality and quality.

Signed by the final examining committee:

_____Chair
Dr. Louis Cuccia

_____External Examiner
Dr. Fabio Cicoira

_____Examiner
Dr. Christine DeWolf

_____Examiner
Dr. Laszlo Kalman

_____Examiner
Dr. Pablo Bianucci

_____Thesis Supervisor
Dr. Ingo Salzmann

Approved by _____
Dr. Pablo Bianucci, Graduate Program Director

December 19, 2024 _____
Dr. Pascale Sicotte, Dean of the Faculty of Arts and Sciences

Abstract

Probing Microstructure and Optical Properties of Organic Semiconductor Thin Films

Shubham Bhagat, Ph.D.
Concordia University, 2024

The immense success of conjugated organic molecules (COMs) in the multi billion-dollar OLED industry has equally raised the interest in conjugated polymers (CPs) for organic electronics. This is largely due to their flexibility and scalable, solution-based processing using cost-efficient methods. In most applications, the utility of such organic semiconductors (OSCs) in electronics relies heavily on tuning their electronic properties via doping. Unlike COMs, which can easily form highly ordered films via vacuum deposition, CPs are thermally fragile, thus, typically requiring solution processing. This often results in films with less-defined microstructures influenced by various experimental conditions. Further, CPs are susceptible to structural and chemical defects that reduce their conjugation length. This thesis employs the unconventional method of high-vacuum electrospray deposition (HV-ESD) to create poly(3-hexylthiophene) (P3HT) films under minimal solvent influence otherwise only applicable for COMs. Conventional solution-processed P3HT is typically semi-crystalline, comprising crystalline and amorphous regions as shown by X-ray diffraction. In contrast, it is found in this work that HV-ESD yields highly amorphous films. This technique allows therefore studying CP films without the complexity of mixed crystalline and amorphous regions, which is important in analyzing properties like the doping of P3HT, where these regions respond differently to doping and information gathered thereon is generally convoluted. Further, this thesis focuses on COMs exploring the optical and structural properties of blends created by the rod-like molecules α -sexithiophene (6T) and para-sexiphenyl (6P), which are prototypical OSCs. Vacuum co-deposited films yield a mixed crystal structure, confirmed by grazing-incidence X-ray diffraction, and unique optical properties. The blends show green emission alongside the characteristic red and blue emissions of pure 6T and 6P explained by J- and H-type aggregation. Additionally, this work includes studies addressing the molecular doping of oligomers to examine transitions between distinct doping phenomenologies based on the conjugation length, and the yet to be fully understood doping of P3HT by Lewis acids as alternative dopants. These studies are nearing publication.

Overall, by commissioning HV-ESD as a tool to deliberately establish amorphous OSC films, and by assessing OSC blends and molecularly doped OSCs in thin films, this thesis contributes a broad view on the interplay between structural and optoelectronic properties of this important material class.

Acknowledgements

I would like to express my heartfelt gratitude to my PhD supervisor, Dr. Ingo Salzmann for his unwavering support, motivation, and invaluable guidance throughout my research journey. His mentorship has been instrumental in my academic growth and success. Thank you.

I gratefully acknowledge the financial support from Concordia University, which funded this research through the Concordia University Graduate Fellowship and the Concordia International Tuition Award of Excellence. Additionally, I am grateful for the research bursary provided by my supervisor, made possible through funding from the Natural Sciences and Engineering Research Council of Canada (NSERC), the Fonds de recherche du Québec-Nature et technologies (FRQNT), and the Government of Canada's New Frontiers in Research Fund (NFRF).

Complex ideas flourish when nurtured by diverse perspectives and constructive criticism. I am deeply grateful to Dr. Christine Dewolf and Dr. Laszlo Kalman, members of my supervisory committee, for their invaluable insights and guidance throughout this research process. Special thanks are also extended to Dr. Josef Simbrunner, Sebastian Hofer, and Dr. Roland Resel at Graz University of Technology, Austria, for their contributions in recording and analyzing the specular X-ray and GIXRD data presented in chapter 5. My sincere thanks to Melissa Berteau-Rainville (Institut National de la Recherche Scientifique, Canada) for performing reference FTIR experiments and for the DFT modeling data presented in chapter 4. I also appreciate the enjoyable experiences we shared during our experiments at beamtimes, working together made the process both productive and enjoyable.

I would like to thank my amazing colleagues Dr. Hannes Hase, Zahra Alinia, Janet Gaba and Nazli Jodaeeasl for being a constant source of support, guidance, and solutions, both in research and beyond. I especially appreciate Dr. Hannes Hase, for being the 'rubber-duck' whenever I needed to bounce ideas around. Our discussions has made a real difference in my research journey. I would like to acknowledge my colleague So-maiyeh Charoughchi for her support during my time in PhD.

Part of the research described in this thesis was performed at the Canadian Light Source, a national research facility of the University of Saskatchewan, which is supported by the Canada Foundation for Innovation (CFI), the Natural Sciences and Engineering Research Council (NSERC), the National Research Council (NRC), the Canadian Institutes of Health Research (CIHR), the Government of Saskatchewan, and the University of Saskatchewan. On behalf our research team, I acknowledge the invaluable experimental support by Dr. Beatriz Diaz Moreno and Dr. Chang-Yong Kim at the Brockhouse Low En-

ergy Wiggler Beamline. Additional computational support for DFT modeling was kindly provided by Calcul Québec (calculquebec.ca) and the Digital Research Alliance of Canada (alliancecan.ca). I acknowledge DORIS (HASYLAB, Hamburg) for providing access to its synchrotron radiation facilities at W1 beamline.

Further, I wish to convey my appreciation to Dr. Laszlo Kalman for providing access to the UV-vis/NIR spectrometer, Dr. Marek B. Majewski for provision of the photoluminescence spectrophotometer, Integrated Platform for Biomolecular Function, Interactions and Structure (BIOFINS) facility at Concordia University for FTIR access, and the Centre for NanoScience Research (CeNSR) for access to the AFM equipment. I am also grateful to William Chicoine from Concordia's Science Technical Center for his assistance with laboratory equipment construction and repairs.

Finally, I extend my heartfelt gratitude to my family, my friends in Montreal, and those across the continent, for their unwavering support and love throughout my PhD journey. Your belief in me has been my strength.

Last but not the least, a special mention goes to my cat, Lyla, whose gentle nudges and playful distractions, made this journey not only possible but also enjoyable. Thank you for reminding me to take breaks and find joy in the little things.

Contribution of Authors

Chapter 4 is a manuscript published by myself, Melissa Berteau-Rainville, Stephanie Beram, and Dr. Ingo Salzmann. While all authors reviewed the final manuscript and approved of the contents, the original draft was written by myself and in-depth revisions were done together with MBR and IS. Grazing-incidence x-ray diffraction data was acquired by myself at the Canadian Light Source Saskatoon, SK, Canada (data depicted in figures 4.4 and 4.9, 4.10 and 4.11.) MBR conducted references for GI-FTIR experiments, including the DFT modeling (data in figure 4.12). Note that the GI-FTIR data was analyzed by myself. SBe established and tested the custom software for ESD data acquisition shown in figure 4.2 and figures 4.6(a) and (b). AFM data presented in figures 4.7 and 4.8 was collected and analyzed by myself. UV-vis/NIR data in figure 4.3 and figure 4.6(c).

Chapter 5 is a manuscript published by myself, William D Leal, Dr. Marek B Majewski, Dr. Josef Simbrunner, Dr. Sebastian Hofer, Dr. Roland Resel and Dr. Ingo Salzmann. The manuscript was approved by all the authors for publication, after in-depth revisions by myself, IS and RR. XRD data in figure 5.2 and 5.7 was collected and analyzed by JS, SH, RR and IS. The crystal structure calculations was done by JS, SH and RR (data in table 5.1). FTIR (figure 5.3, table 5.1) and UV-vis/NIR (figure 5.4) was collected and analyzed by myself. PL data acquisition was handled by WL. However, all PL data was analyzed by myself (figures 5.5, 5.6, 5.9, 5.10, 5.11 and tables 5.3, 5.4 and 5.5).

Table of Contents

List of Figures	x
List of Tables	xvii
List of Associated Works	xviii
List of Abbreviations	xxii
1 Introduction	1
2 Fundamentals of Organic Semiconductors	7
2.1 Organic Semiconductors	7
2.1.1 Inorganic <i>versus</i> Organic Semiconductors	7
2.1.2 Electronic Structure of Organic Semiconductors: From Molecules to Solids	8
2.1.3 Optical Properties of Organic Semiconductors	10
2.2 Structural to Energetic Disorder in Organic Semiconductors	14
2.3 Doping of Organic Semiconductors	15
2.3.1 Doping with Molecular Dopants	16
3 Methods	19
3.1 Sample Preparation	19
3.1.1 Vacuum Sublimation of Organic Molecules	19
3.1.2 High Vacuum Electrospray Deposition of Conjugated Polymers	20
3.1.2.1 Taylor's cone formation.	21
3.1.2.2 Jet formation.	21
3.1.2.3 Formation of gas phase ions.	21
3.2 Experimental Methods	22
3.2.1 X-Ray Diffraction (XRD)	22
3.2.1.1 Basic theory	22
3.2.1.2 Experimental setup	26
3.2.1.3 Data acquisition and treatment	26
3.2.2 Optical Absorption Spectroscopy (UV-vis/NIR)	27
3.2.2.1 Basic theory	27
3.2.2.2 Experimental setup	28

3.2.2.3	Data acquisition and treatment	28
3.2.3	Photoluminescence Spectroscopy (PL)	29
3.2.3.1	Basic theory	29
3.2.3.2	Data acquisition and treatment	31
3.2.4	Fourier-Transform Infrared Spectroscopy (FTIR)	31
3.2.4.1	Basic theory	31
3.2.4.2	Experimental setup	33
3.2.4.3	Data acquisition and treatment	34
3.2.5	Atomic Force Microscopy (AFM)	34
3.2.5.1	Basic theory	34
3.2.5.2	Data acquisition and treatment	36
4	Amorphous Poly(3-hexylthiophene) (P3HT) Thin Films by Vacuum Electro-spray Deposition	37
	Abstract	37
4.1	Introduction	38
4.2	Experimental Details	40
4.2.1	Materials	40
4.2.2	Sample preparation	40
4.2.3	Sample nomenclature	40
4.2.4	Grazing incidence X-ray diffraction	41
4.2.5	Absorption spectroscopy	41
4.2.6	Atomic force microscopy	42
4.3	Results and Discussion	42
4.3.1	Optimizing deposition parameters	42
4.3.2	Assessing pre-aggregation in solution	44
4.3.3	Structure by grazing incidence X-ray diffraction	46
4.4	Summary	49
4.5	Supplementary Data	49
4.5.1	Optimization of HV-ESD parameters	49
4.5.1.1	Substrate requirement	50
4.5.1.2	Solution Concentration	50
4.5.2	GIXRD reciprocal space maps	53
4.5.3	GIXRD line scans with baseline correction	56
4.5.4	GI-FTIR spectroscopy	57
5	Aggregate Formation in Crystalline Blends of α-Sexithiophene and Para-Sexiphenyl	58
	Abstract	58
5.1	Introduction	59
5.2	Methods	59
5.3	Results	61
5.3.1	Structural properties by X-ray diffraction	61
5.3.2	Fourier transform infrared spectroscopy (FTIR)	64
5.3.3	UV-vis/NIR spectroscopy	65

5.3.4	Photoluminescence spectroscopy (PL)	67
5.4	Conclusions	71
5.5	Supplementary Data	71
5.5.1	Additional experimental information	71
5.5.2	Additional experimental data	72
5.5.2.1	FTIR peak positions	72
5.5.2.2	Additional Photoluminescence Spectroscopy Data	72
5.5.3	Structure Modelling	75
6	Ongoing and Future Research Directions	76
6.1	p-Doping of Oligothiophenes with F4CTNQ	76
6.2	p-Doping of BTBT Derivatives with Molecular Dopants	80
6.3	Doping with Lewis Acids	84
7	Summary, Conclusions, and Outlook	87
	Bibliography	89
A	Chemical Structures of Supplementary Materials	117

List of Figures

2.1	Diagram illustrating the energy levels of σ and π -bonds formed from the atomic orbitals of carbon atoms in ethene. For clarity, the $2sp^2$ orbitals involved in σ -bonding with hydrogen atoms are not shown. The energy scale represents the kinetic energy of a free electron, thus orbital energy levels are displayed as negative values corresponding to their binding energies. Figure taken from [1] A. Köhler and H. Bässler, <i>Electronic Processes in Organic Semiconductors: An Introduction</i> . Weinheim: Wiley-VCH, 2015. Copyright 2015 Wiley-VCH Verlag GmbH & Co. KGaA.	8
2.2	Potential energy curves of a molecule described as a function of the normal mode coordinate Q , showing the vibrational levels within the energy levels. Each energy level ($S_0, S_1 \dots S_n$) has vibrational sub-levels ($\nu_0, \nu_1 \dots \nu_n$) that are represented by the horizontal lines.	11
2.3	Figure visually representing the energy levels of the ground (GS) and excited states (ES) for both two isolated molecules (M_1 and M_2) and a pair of electronically coupled molecules (M_1M_2). For M_1M_2 coupled molecules, the ES splits into a lower ES (E_-) and higher ES (E_+) (not marked in the figure). The coupled molecules are depicted in three distinct spatial arrangements: (a) side-by-side representing H-aggregates, (b) head-to-tail leading to J-aggregates, and (c) a case for oblique alignment of isolated molecules relative to each other. For each configuration, the figure highlights the relative alignment of the excited state transition dipoles, potential optical transitions, and the magnitude of the resulting total transition dipole moment. Figure taken from [1] A. Köhler and H. Bässler, <i>Electronic Processes in Organic Semiconductors: An Introduction</i> . Weinheim: Wiley-VCH, 2015. Copyright 2015 Wiley-VCH Verlag GmbH & Co. KGaA.	13
2.4	Illustration showing energy levels during IPA and CTC formation in p-doping of OSC.	17
2.5	Skeletal structures of regioregular poly(3-hexylthiophene-2,5-diyl) (P3HT), α -quaterthiophene.	17
3.1	Schematic showing three different thin film growth modes during vacuum thermal sublimation.	20

3.2	Illustration of high vacuum electrospray deposition technique. The parts are labeled by numbers and are named as- (1) metallic emitter capillary, (2) inlet or entrance capillary, (3) roughing pump at stage I, (4) roughing pump at stage II, (5) turbo pump at stage III, (6) high vacuum (HV) chamber.	22
3.3	Representation of X-ray diffraction from crystalline lattice planes, showing the incoming (\vec{k}_i) and outgoing (\vec{k}_f) wavevectors, the Bragg angle (θ), the lattice-plane spacing (d), and the scattering vector (\vec{q}).	24
3.4	Illustration of grazing-incidence X-ray diffraction (GIXRD) geometry, showing the incoming (\vec{k}_i) and outgoing (\vec{k}_f) wavevectors beams, Bragg angle (θ), grazing incidence angle α_i and components of scattering vector (\vec{q}), parallel (q_z) and perpendicular q_{xy} to film surface.	26
3.5	A simplified illustration showcasing the key components of a dual-beam UV-vis/NIR spectrometer, comprising a <i>light source</i> , a <i>diffraction grating</i> to split the light from the lamp into its constituent wavelengths, <i>slit</i> for controlling the wavelength resolution, a <i>chopper mirror</i> that alternatively directs the incident wavelength towards the sample and reference beam path, a <i>detector</i> for recording the light intensity that passes through <i>reference</i> and <i>sample</i> and a computer with <i>acquisition software</i> to generate corresponding absorption spectrum.	27
3.6	Inert atmosphere sample holder used for measuring optical absorption spectroscopy spectrum of thin film samples. The compartment is sealed onto the base plate using the KF o-ring. For UV-vis/NIR spectroscopy measurements, an inert sample holder with quartz windows in used.	29
3.7	Jablonski diagram for photoluminescence, highlighting the pathways of absorption, vibrational relaxation, and fluorescence emission. Diagram shows ground state (S_0) and n^{th} excited state (S_n) energy levels of a molecule along with their vibrational levels from ν_0 to ν_n .	30
3.8	Conceptual outline of a transmission-mode FTIR spectrometer employing an IR source, a detector, a sample and a Michelson interferometer. The beamsplitter (B), fixed mirror (M), and moving mirror (M') are the components of a Michelson interferometer.	32
3.9	Schematic of an AFM; a sharp probe mounted on a cantilever, scans the surface of the thin film deposited on a substrate. A laser and a photodiode records cantilever deflections, resulting from probe-sample atomic interactions. A feedback loop monitors these movements and apply a constant force on the cantilever using piezo elements, to generate an image of sample's topography.	35
4.1	(a) Ion current versus time for the mixed-solvent system of toluene: methanol in 6:1 ratio (no P3HT added), with varying nominal injection rates of 15 mL/hr, 10 mL/hr and 5 mL/hr. (b) Same but with variable high voltage applied to the emitter (10 mL/hr nominal injection rate). The ion current values are recorded against a metal sample holder and the current corresponding to solvent spray are highlighted in yellow.	43

4.2	(a) Ion current versus time for pure methanol (no P3HT added) and (b) pure chloroform using 10 mL/hr nominal injection rate; the high voltage applied to emitter is given in the figure, data recorded against a metal sample holder.	43
4.3	Comparison of absorption spectra from solution of P3HT in (a) toluene: methanol (6:1) and chloroform. (b) toluene and toluene: methanol (6:1)	45
4.4	Grazing incidence X-Ray diffraction results from P3HT films deposited <i>via</i> HV-ESD on SiO _x substrates from (a), series TM-a using toluene: methanol as solvent without inlet heater (b), series TM-b with toluene: methanol applying the inlet heater, (c) series CF-a using chloroform without inlet heater, and (d) series CF-b using chloroform applying the inlet heater; the peak corresponding to the (100) lattice planes has been omitted here for better visualization of peaks showing weaker intensity.	46
4.5	Grazing incidence X-Ray diffraction results from dropcast P3HT films deposited on SiO _x wafers from (a) series TM using toluene: methanol as the solvent, (b) series CF using chloroform. The solid black curve represents the reference data at room temperature, dark and light grey dashed curve indicate data recorded on films heated <i>in-situ</i> under helium atmosphere to 100°C and 150°C, respectively; the solid grey curve corresponds to post-annealed films allowed to cool down from 150°C to room temperature. . .	48
4.6	Ion current versus time plot for HV-ESD P3HT dissolved in toluene: methanol (6:1) using a nominal injection rate of 5 mL/hr and a voltage between 2.5 kV and 3 kV on (a) quartz and (b) ITO substrates. (c) Comparison of the absorption spectra a HV-ESD film of P3HT from in toluene: methanol (6:1) and of a spin-coat film of P3HT (from chloroform) as reference, both on quartz substrates.	50
4.7	AFM images of HV-ESD P3HT films from series TM deposited on SiO _x using a nominal injection rate of 10 mL/hr without inlet heater in (a, b), and of 5 mL/hr without inlet heater in (c).	51
4.8	AFM images of HV-ESD P3HT films from series CF deposited on SiO _x using an injection rate of (a) 10 mL/hr without inlet heater, (b) 10 mL/hr with inlet heater, (c) 5 mL/hr without inlet heater, (d) 5 mL/hr with inlet heater. The inset in (a) shows a cross section of a characteristic morphology feature of the adsorbate, where vertical dimensions in the 10-30 nm, and lateral dimensions in the 1-2 μm regions are found.	52
4.9	GIXRD reciprocal space maps from which the line scans in the main text are generated by intensity integration along $q = (q_{xy}^2 + q_z^2)^{1/2}$: Drop cast P3HT film from toluene: methanol at, (a) room temperature (b) during annealing <i>in-situ</i> under helium atmosphere at 100°C, and (c) 150°C, (d) post-annealed drop cast film allowed to cool down from 150°C to room temperature. HV-ESD P3HT films from series TM deposited on SiO _x using a nominal injection rate of, (e) 10 mL/hr without inlet heater, (f) 10 mL/hr with inlet heater, (g) 5 mL/hr without inlet heater, (h) 5 mL/hr with inlet heater, (i) 2.5 mL/hr without inlet heater, (j) 2.5 mL/hr with inlet heater; colors correspond to the square root of the recorded intensity.	54

4.10 GIXRD reciprocal space maps from which the line scans in the main text are generated by intensity integration along $q = (q_{xy}^2 + q_z^2)^{1/2}$: Drop cast P3HT film from chloroform at (a), room temperature, (b), during annealing *in-situ* under He at 100°C, (c) 150°C, and (d) post-annealing allowed to cool down room temperature. HV-ESD P3HT films from series CF on SiO_x using a nominal injection rate of, (e) 10 mL/hr without inlet heater, (f) 10 mL/hr with inlet heater, (g) 5 mL/hr without inlet heater, (h) 5 mL/hr with inlet heater, (i) 2.5 mL/hr without inlet heater, (j) 2.5 mL/hr with inlet heater; black saturation corresponds to the square root of the recorded intensity. 55

4.11 Left: Integrated linescan data (solid lines) for the reciprocal space maps shown in figure 4.10 together with baselines (dashed curves). Curves are shown for the samples established using the inlet heater; nomenclature as used throughout the main text. Right: Same curves but baseline corrected; the are of the amorphous halo is highlighted in yellow. All films were measured under He atmosphere, the dropcast film was heated *in-situ* to 100°C and 150°C and then let cool down again to room temperature (RT). This cooling cycle shows the expected shift of the Bragg peaks to higher values of q due to thermal expansion together with an increase in diffraction intensity of the amorphous halo at elevated temperature; post annealing, the Bragg peaks are again observed at their initial position. Notably, the ESD films also show the amorphous halo but no indication of Bragg peaks which evidences no detectable crystalline order; no change was observed upon annealing the ESD films (not shown). Importantly, the diffraction intensities shown in the figure are raw data, all curves have been recorded using identical experimental parameters (primary-beam footprint, integration time, synchrotron ring current due to top-up mode at the Canadian Light Source), therefore, the scattering intensities of the amorphous halos are indicative of the relative amount of amorphous P3HT present in the samples. 56

4.12	(a) GI-FTIR data recorded for the samples established by HV-ESD from toluene:methanol (series TM-a, TM-b) and (b) from chloroform (series CF-a, CF-b), together with data of the drop-cast reference. To interpret the data, a DFT-calculated vibrational spectrum (for a geometry-optimized 3-hexylthiophene heptamer calculated at the ω B97X-D[2]/6-31+g(d,p) level of theory in Gaussian 09 rev. E.01[3]) and an IR spectrum collected in transmission mode (for a dropcast sample on undoped silicon) are additionally shown. These reference data demonstrate the correspondence between the GI-FTIR data recorded on the HV-ESD films and the expected vibrations of P3HT. The vibrations in 1700- 800 cm^{-1} region are the most characteristic for P3HT[4]: According to literature reports and in line with our DFT modeling, the peak at $\sim 820 \text{ cm}^{-1}$ represents the out-of-plane C–H vibration of the thiophene ring,[5] that at $\sim 1377 \text{ cm}^{-1}$ is assigned to methyl deformation,[4] while the vibrations around 1520- 1440 cm^{-1} are due to symmetric and anti-symmetric vibrations of C=C in thiophene.[4, 5] The peak positions recorded in GI-FTIR data are 819 cm^{-1} , 1377 cm^{-1} and 1446 cm^{-1} , respectively, and thus agree well with the literature values, the peak positions obtained for FTIR in transmission, as well as the results of the DFT calculations. In analogy to the GIXRD data shown in figure 4.11, all GI-FTIR data are recorded under identical experimental conditions (grazing angle of the IR beam: 6.3°) and are not normalized, therefore, the relative intensities qualitatively allow assessing the relative P3HT content of the films, which turns out to be highly similar in all investigated samples.	57
5.1	Chemical structure of (a) para-sexiphenyl (6P) and (b) α -sexithiophene (6T)	60
5.2	Structural analysis of 6T+6P films. (a) XRD on SiO_x and HOPG substrates, calculated peak positions for pure 6P (cell choice II) [6, 7] are indicated by vertical dotted lines for the (–111) reflection on HOPG and the (003) peak on SiO_x ; the asterisk marks a second order contribution by the substrate. (b) Reciprocal space map obtained by GIXRD on the film grown on HOPG showing the experimental data together with calculated reflections of pure 6P for (–111) orientation (white) and (–112) texture (magenta); diffraction intensity due to the HOPG substrate is labelled by ‘H’. (c) GIXRD data for the film on SiO_x (bottom) and plotted together with Debye–Scherrer rings calculated for the strongest reflections based on our structure solution (top), which highlights the occurrence of vertical Bragg rods and the similarity of the mixed crystal structure on both substrates.	62
5.3	FTIR spectra of pure 6T (red curve), 6P (blue) and codeposited 6T+6P (magenta) films grown on SiO_x	65
5.4	UV-vis/NIR spectra of pure 6T (red curve), pure 6P (blue), and codeposited 6T+6P (magenta) films on quartz; features discussed in the text are labelled.	66

5.5	Photoluminescence spectra from pure 6T (red curve), 6P (blue) and codeposited 6T+6P (magenta) films on SiO _x . For better comparison, PL emission of pure 6T and the codeposited and 6P film has been normalized to 0-1 emission peak of pure 6P.	68
5.6	(a) PL data for ‘interfacial 6T’ extracted from Ref. [8] and fitted with four Voigt functions (green curves). (b) Corresponding PL data recorded for the 6T+6P film on HOPG; data is fitted with ‘interfacial 6T’ peaks [positions taken from (a)] and bulk 6T peaks (orange curves). (c) PL data recorded for the 6T+6P film on SiO _x again fitted with the peaks from ‘interfacial 6T’, bulk 6T, and with peaks assigned to 6P (blue curves); the fits of the pure spectra (bulk 6T, 6P) are provided as figures 5.9 and 5.10 in the section 5.5; peak positions are provided in tables 5.4 and 5.5.	69
5.7	Sketch of the two extreme cases of interlayer arrangement that can occur for 6T+6P films on SiO _x together with the crystallographic unit cell suggested for the mixed structure and the proposed orientation of the molecules within the unit cell (the angle between the long molecular axes of 6P and 6T is smaller than 1°); the calculated GIXRD intensities for this tentative structure solution are shown together with the reciprocal space map of 6T+6P on HOPG in the section 5.5 figure 5.12.	70
5.8	Illustration of co-deposition by physical vapour deposition in ultra-high vacuum (UHV) chamber.	72
5.9	Fitted PL spectra of (a) 6T on quartz and (b) on SiO _x ; peaks fitted using Voigt functions.	73
5.10	Fitted PL spectra of (a) 6P on quartz and (b) on SiO _x ; peaks fitted using Voigt functions.	73
5.11	Comparison of absorption and emission spectra of (a) pure 6P, (b) pure 6T on quartz and SiO _x substrates, and (c) of the PL data recorded for codeposited 6T+6P films on SiO _x (black curve) and HOPG (grey curve) as substrate; see also figure 5.6 of the main text.	74
5.12	Reciprocal space map obtained by GIXRD on the 6T+6P film grown on HOPG showing the experimental data together with calculated reflections [(-111) texture] of the refined unit cell with parameters a=5.696Å, b=7.836Å, c=26.888Å, α=83.62°, β=86.42°, γ=89.44°(cf. table 5.1 in the main text). The map shows the indices which have been used for the unit cell determination following an indexation method developed recently [9–11]. Circle diameters correspond to intensities calculated for a tentative model structure comprising one molecule of each species in the unit cell (see illustration of the structure in figure 5.7 of the main text).	75
6.1	(a) UV-vis/NIR spectra of pristine H _x Ts (x= 5, 7, 9, 11) films, (b) a plot of extrapolated absorption onset versus 1/n where n is the number of thiophene repeat units. The absorption onset values of H4T, H6T, H8T and H10T are taken from Ref. [12, 13] for comparison.	77

6.2	UV-vis/NIR spectra of thin-film of HxTs ($x = 5$ to 11) and P3HT upon doping with F4TCNQ at a dopant molar ratio of 9% per thiophene-ring; the vertical lines mark the peak positions assigned to the HOMO-LUMO transition of the CTC in doped HxTs ($x= 5$ to 8). The dashed lines mark the position of peaks characteristic to F4TCNQ $^{\bullet-}$. In ref. [12, 13] peaks ‘A’ and ‘B’ are interpreted as indicators of H10T $^{\bullet+}$ (labeled as B) and the CTC related transition in H10T-F4TCNQ (A), respectively. The optical absorption spectra of doped H6T, H8T, H10T and P3HT were taken from ref. [12, 13] for comparison.	78
6.3	UV-vis/NIR absorption spectra of pristine BTBTx-films and mixed films of BTBTx and TCNQ derivatives in a nominal mixing ratio of 1:1, see the IE and EA values for the OSCs and dopants, respectively, in table 6.1 together with the nomenclature of the BTBT derivatives. (a)–(f) Equimolar mixed films showing CTC formation which is marked as peaks T1 and T2, (g)–(i) Systems without CTC formation due to phase separation, as shown by supporting GIXRD measurements (diffraction data not shown in this thesis). The spectrum of BTBT8:F4TCNQ film is highlighted because of the significant difference in the absorption peaks in the low energy region (see detailed discussion in the text).	82
6.4	FTIR spectra of thin-films of BTBT1, BTBT5 and BTBT7 doped with F2TCNQ and F4TCNQ, in a nominal mixing ratio of 1:1. The IR data from pristine F2TCNQ and F4TCNQ films is shown at as bottom curves, for reference. Note that data in the region of only C \equiv N-stretching mode is shown. The wavenumber used for analysis is marked by a tick.	83
6.5	UV-vis/NIR spectra of P3HT doped with BCF, BC3F, BC2F and BCOF (a) before stirring, (b) after stirring. The dashed line shows the polaronic feature of P3HT and the solid line shows the fundamental absorption of P3HT. The inset images highlights the P3HT polaronic features.	84
A.1	Chemical structure of [left] regioregular P3HT versus [right] regiorandom P3HT.	117
A.2	Sketetal structure of (a) benzothieno[3,2-b][1]benzothiophene (BTBT) derivatives, (b) p-dopant 7,7,8,8-tetracyanoquinodimethane (TCNQ) and its flourinated derivatives (FxTCNQ), (c) hexylated oligothiophenes (HxT) with even number of thiophene repeat units, with $m= 1$ to 4, (d) hexylated oligothiophenes (HxT) with odd number of thiophene repeat units, with $m= 1$ to 4.	117
A.3	Skeletal structure of a series of Lewis acids, (a) tris(pentafluorophenyl)borane (BCF), (b) tris(trifluorophenyl)borane (BC3F), (c) tris(diafluorophenyl)borane (BC2F) and (d) tris(pentafluorophenyl)borate (BCOF)	118

List of Tables

5.1	Comparison of the unit cell parameters refined for the equimolar mixed film and pristine 6P	63
5.2	Comparison between fundamental vibration peaks of 6P and 6T (values in cm^{-1}).	72
5.3	Summary of intensity ratios of $(0 - 1)/(0 - 0)$ and $(0 - 2)/(0 - 1)$ peaks in pure 6P, 6T and codeposited films on SiO _x , and the Huang-Rhys factors (S) calculated for the different pure (S _P) and codeposited (S _C) films.	73
5.4	Absorption and emission maxima for pure 6P, 6T and codeposited film.	73
5.5	Summary of deconvoluted peak position for 6P and 6T (interfacial and bulk) films deposited on Si substrate (values in eV).	74
6.1	DFT calculated values for the ionisation energy of the donor and the electron affinity of the acceptor materials.	80

List of Associated Works

[14] **Dipolar Substitution Impacts Growth and Electronic Properties of Para-Sexiphenyl Thin Films**

J. Hu, N. Aghdassi, S. Bhagat, Y. Garmshausen, R. Wang, N. Koch, S. Hecht, S. Duhm and I. Salzmann

Advanced Materials Interfaces, vol. 7, Art. no. 3, 2020.

Investigating the impact of non-symmetrical substitution of 6P on the structure, energy levels and the morphology of thin films of this prototypical molecule. I deposited pristine 6P films via vacuum sublimation that were then used to acquire the reference specular XRD and GIXRD data.

[15] **Chemical Doping of Organic Semiconductors**

S. Bhagat, H. Hase and I. Salzmann

in *Organic Flexible Electronics - Fundamentals, Devices and Applications, 2nd Edition*, P. Cosseddu and M. Caironi, Ed. Woodhead Publishing, 2021, pp. 107-141.

A review chapter on molecular doping in organic semiconductors. For a comprehensive overview of the broader field, including topics beyond the scope of this work, readers are encouraged to consult this publication on this subject. This publication is a carefully revised and updated version of [16] H. Hase and I. Salzmann, 2019. Doping in organic semiconductors. In: Ostroverkhova, O. (Ed.), Handbook of organic materials for electronic and photonic devices, second ed., Woodhead Publishing, pp. 349–383

[17] **Aggregate Formation in Crystalline Blends of α -Sexithiophene and Para-Sexiphenyl**

S. Bhagat, W. Leal, M. Majewski, J. Simbrunner, S. Hofer, R. Resel, and I. Salzmann

in *Electronic Structure*, vol. 3, p. 34004, 2021.

A study on structural and optical properties of the equimolar crystalline blends of 6T and 6P molecules. In this thesis as chapter 5.

- [18] **Macromolecularly Engineered Thermoreversible Heterogeneous Self-Healable Networks Encapsulating Reactive Multidentate Block Copolymer-Stabilized Carbon Nanotubes**

G. Zhang, T. Patel, P. N. Pothanagandhi, S. Bhagat, H. Hase, A. Jazani, I. Salzmänn, Z. Ye, and J. K. Oh

Macromolecular Rapid Communications, vol. 42, p. 2000514, 2021.

I was involved in depositing films of materials used in this work and performing conductivity measurements on the deposited films.

- [19] **Sterically-Hindered Molecular p-Dopants Promote Integer Charge Transfer in Organic Semiconductors**

S. Charoughchi, J. T. Liu, M. Berteau-Rainville, H. Hase, M. S. Askari, S. Bhagat, P. Forgione, and I. Salzmänn

Angewandte Chemie International Edition, vol. 62, no. 31, p. e202304964, Aug. 2023.

I was involved in atomic force microscopy measurements on poly(3-hexylthiophene-2,5-diyl) thin-films doped with the novel dopant presented in that work. I did the surface roughness analysis on the thin-films.

- [20] **Amorphous Poly (3-hexylthiophene)(P3HT) Thin Films by Vacuum Electro-spray Deposition**

S. Bhagat, M. Berteau-Rainville, S. Beram and I. Salzmänn

Crystal Growth & Design, vol. 24, Art. no. 15, 2024.

This study focuses on deposition of P3HT films under minimal influence of solvent and the structural characteristics of the deposited films. In this thesis as chapter 4.

- [21] **Tuneable Low Gap Mixed-Stack Charge-Transfer Crystals**

S. Bhagat, M. Berteau-Rainville, A. Optiz, H. Mendez, A. Jung, K. Sauer, B. Wegner, P. Beyer, K. Matte, H. Hase, N. Koch, G. Heimel, I. Salzmänn and Y. Greetz
To be submitted.

A study on CTC formation between benzothieno[3,2-b][1]benzothiophene (BTBT) derivatives and FxTCNQ, that covers a wide range of IE (for BTBTs) and EA (for FxTCNQ). I was involved in UV-vis/NIR and FTIR experiments, collecting GIXRD data and drafting of this publication.

[22] **Degradation-assisted doping of organic semiconductors: a new strategy enabled by Lewis acids**

M. Berteau-Rainville, T. P. L. Cosby, S. Bhagat, A. E. Latuski, E. Orgiu, T. Baumgartner, C. B. Caputo and I. Salzmann

To be submitted.

A study on doping of P3HT with a series of Lewis acids, aiming to provide insights into the mechanism of doping by Lewis acids. I was involved in performing UV-vis/NIR and FTIR experiments on thin-films of P3HT doped with an array of Lewis acids of varying electron affinity.

List of Abbreviations

4T	α -quarterthiophene
6P	para-sexiphenyl
6T	α -sexithiophene
6T+6P	codeposited equimolar film of α -sexithiophene and para-sexiphenyl
AFM	atomic force microscope
BCF	tris(pentafluorophenyl)borane
B2CF	tris(diafluorophenyl)borane
B3CF	tris(trifluorophenyl)borane
BCOF	tris(pentafluorophenyl)borate
BTBT	benzothieno[3,2-b][1]benzothiophene
BTBTx	benzothieno[3,2-b][1]benzothiophene derivatives
CF	chloroform
COM	organic molecules
CP	conjugated polymer
CTC	charge-transfer complex
DOS	density of states
DFT	density function theory
DC	dropcast
EA	electron affinity
ESD	electrospray deposition
FCT	fractional charge transfer
FTCNQ	2-fluoro-7,7,8,8-tetracyanoquinodimethane
F2TCNQ	2,5-difluoro-7,7,8,8-tetracyanoquinodimethane
F4TCNQ	2,3,5,6-tetrafluoro-7,7,8,8-tetracyanoquinodimethane
F _x TCNQ	tetracyanoquinodimethane and its fluorinated derivatives
FTIR	Fourier-transform infrared spectroscopy
GI-FTIR	grazing incidence Fourier-transform infrared spectroscopy
GIXRD	grazing incidence X-ray diffraction
HOMO	highest occupied molecular orbital in the ground state
H _x Ts	oligothiophenes with hexylated side chains, x = 4 to 11
HV	high vacuum
ICT	integer charge transfer
IPA	ion pair
IE	ionization energy
IR	infrared
ISC	inorganic semiconductor
ITO	indium tin oxide

LA	Lewis acids
LUMO	lowest unoccupied molecular orbital in the ground state
OLED	organic light emitting diode
OSC	organic semiconductor
P3HT	poly(3-hexylthiophene-2,5-diyl)
PL	photoluminescence spectroscopy
SiO _x	silicon substrate with a native oxide layer
TCNQ	7,7,8,8-tetracyanoquinodimethane
TM	mixture of toluene and methanol solvents in 6:1 ratio
UHV	ultra-high vacuum
UV-vis/NIR	optical absorption spectroscopy in the range of ultraviolet radiation (UV), visible light (vis), and the near infrared (NIR)
XRD	X-ray diffraction

Chapter 1

Introduction

Organic semiconductors (OSCs), composed of conjugated polymers (CPs) and organic molecules (COMs), have gained significant attention in recent decades due to their unique combination of desirable properties. A key advantage of OSCs lies in their facile large-scale processability, enabling deposition on a variety of substrates, including flexible ones [23–26] for application in wearable electronics [27, 28], biomedical devices [29–32], or flexible displays [33, 34]. Furthermore, the optoelectronic properties of OSCs can be readily tuned through chemical design, that is their substitution with functional groups, e.g., to modify the frontier molecular orbital energies, or modifications to the conjugation length which modify their fundamental optical gap [35–37]. This remarkable ability of OSCs to tailor their properties through chemical design and processing techniques, coupled with their compatibility with flexible substrates, positions them as promising materials for a wide range of emerging electronic and optoelectronic devices [25, 29–31, 33, 34]. This adds to their application potential in OLEDs [38–40], a multi-billion market today, in organic thermoelectrics [41, 42] to convert waste heat into electric energy in future sustainable applications, in organic photovoltaics [43–45], and organic field effect transistors [25, 46, 47] for low-cost, flexible circuitry.

The performance of organic electronic devices is, however, limited by an intrinsically low charge carrier concentration of OSCs at room temperature due to their large fundamental gap typically much larger than that of silicon. Therefore, this necessitates the need for doping, like in inorganic semiconductors (ISCs) to achieve practical conductivity levels. Doped OSCs are employed as transport layers in optoelectronic devices capitalizing on an increased conductivity and on the ability to tailor injection barriers for charge carriers at metal electrodes interfaces [48]. Like in ISCs, mobile charge carriers are also generated via doping in OSCs, however, the doping mechanism is significantly different from that of ISCs [49, 50]. For instance, in ISCs, impurity *atoms* are introduced directly into the crystal lattice of the host, e.g., adding boron or phosphorus atoms to silicon, for p-type or n-type doping, respectively, and these impurities form covalent bonds with the ISC host. Meanwhile, in OSCs, dopant *molecules* are used as electron acceptors or donors for p-type or n-type doping, respectively, to facilitate charge transfer and generate mobile charge carriers. Due to the non-covalent nature of interaction between COMs and CPs in the solid state, doping relies on electron transfer between the OSC and dopant frontier molecular orbitals, which can be inefficient and require doping concentrations in

the range of several percent. In contrast, *doping efficiencies*, defined as mobile charge carriers generated per dopant added, in inorganic semiconductors are often close to unity, as dictated by Fermi-Dirac statistics, where all available dopant sites are readily ionized at room temperature [51]. Typically, for OSCs they are less than one for typical oxidative or reductive dopants.

The charge transport properties of OSCs differ significantly from their inorganic counterparts due to fundamental differences in their electronic structure and intermolecular interactions. Unlike ISCs, OSCs are held together by comparably weak Van der Waals interaction, predominantly inhibiting band-like carrier transport*, and the solid state structures of OSCs tend to be defect rich.

The film microstructure plays a crucial role in the doping efficiency of OSCs as it defines the mutual position of dopant and host species [53]. Films of COMs can exhibit significantly well-defined structures and form crystalline films of remarkable quality when processed *in-vacuo* via thermal sublimation. There, the chemical composition and temperature of the substrate [54–57] along with stable and precisely adjustable deposition rates [56, 58, 59], are crucial for achieving high-quality films. However, CPs, on the other hand, are thermally fragile through their longer conjugated backbone and, therefore, cannot be processed by thermal sublimation in vacuum, as this would result in their chemical degradation, e.g., breaking of the CP backbone or losing the substituents such as alkyl-sidechains, which are typically added to increase solubility [60].

Solution processing, the primary method for CPs, introduces a multitude of variables that impact film morphology [61–64], including solvent properties [65–68], evaporation rate [69], and substrate characteristics [70–72]. This often results in ‘ill-defined’ microstructures [73] with limited control, e.g., for doped OSCs, over the dopant-host interaction. There, several studies suggest that enhancing structural order in CPs can improve the doping efficiency [74–78] where the choice of solvent, processing temperature, and other parameters can significantly influence the final film morphology [76, 78–83].

Doping is undoubtedly crucial for enhancing the conductivity of OSCs as the performance of organic semiconductors is intricately linked to the doping process, which intends to introduce free-charge carriers into the material. The impact of doping is clearly demonstrated in the advancement of OLED technology, where it has played a key role in enabling the development of high-performance OLEDs [84–86]. In the doping of OSCs, using molecular donors or acceptors as n-type or p-type dopants, respectively, two fundamentally distinct phenomena can be observed, namely– *fractional* charge transfer (FCT) as a result of the formation of ground-state *charge-transfer complexes* (CTCs) and *integer* charge transfer (ICT) which leads to spatially separated *ion-pairs* (IPAs) [53, 87]. CTC formation arises from the hybridization of the frontier molecular orbitals, the highest molecular orbital (HOMO) of the electron donor and the lowest unoccupied molecular orbital (LUMO) of the acceptor, to generate new states, a new doubly ‘occupied’ HOMO and an ‘empty’ LUMO states within the CTC, that is, *bonding* and *antibonding* supramolecular hybrid orbitals. The extent of hybridization between interacting orbitals and the resulting energy separation between the *newly* formed states depend critically on several factors,

*In many organic crystals and highly ordered thin films, the charge transport can be described in a band-like regime similar to that observed in inorganic semiconductors [52].

including the energetic and spatial overlap of the interacting orbitals, and on the energy difference between the donor's HOMO and the acceptor's LUMO [53, 87]. Integer charge transfer becomes energetically favorable when the electron affinity (EA) of the acceptor equals or exceeds the ionization energy (IE) of the donor [50, 53]. According to common notion, ICT is generally preferred due to its ability to directly generate free charge carriers, which translates into increased *conductivity*, mobile hole generation upon CTC formation requires ionization of the CTC instead, which is a significantly worse dopant than the pristine doping agent. Further, this process leads to the formation of deep traps for charges, requiring additional energy for ionization, thus, hindering efficient charge transport [53, 88–90].

In the organic semiconductor scientific community, it was believed for a long time that if $EA_{acceptor} > IE_{donor}$ condition is not satisfied, then, due to unfavourable energy offset, doping takes place via CTC formation, i.e., it is one or the other pathway for p-doping of OSC [53, 87, 91]. For example, when p-type doping of CPs like, poly(3-hexylthiophene) (P3HT⁺) with the strong electron acceptor dopant 2,3,5,6-Tetrafluoro-tetracyanoquinodimethane (F4TCNQ[‡]), the initial literature reports demonstrated primarily IPA formation [76, 88–90, 92] for this host–dopant system. However, recent reports confirmed that CTC and IPA can co-exist within doped P3HT [93], and the ratio of one over the other can be preferentially tuned depending on processing conditions, doping concentration and microstructural order [78, 80]. Although, what conditions exactly favour one mechanism over the other is still a topic of ongoing research. It has been suggested that factors such as molecular weight [94], doping concentration, crystallinity [78] and the presence of different polymorphs [80], i.e., the microstructure of the films, directly impact the degree of charge transfer and whether IPA or CTC formation is favoured [76, 78, 80, 95].

Structural disorder affect the local energetic environment (see section 2.2 for further details), influencing dopant distribution and the overall doping efficiency. For instance, Jacobs et al. reported a polymorph-dependent degree of charge transfer in P3HT–F4TCNQ blended films due to different processing conditions. A new polymorph was found when the temperature of the processing solution was increased from 60°C to 80°C, causing a shift from IPA to CTC formation. This mixed crystal polymorph is characterized by a cofacial stacking of F4TCNQ and the thiophene units of the P3HT backbone, leading to shorter out-of-plane stacking distances (in P3HT of edge-on orientation on the substrate) than films that predominantly showed IPA formation [80], where the dopants are intercalated in the alky-chain region of the polymer. Furthermore, Neelamraju et al. argued that structural disorder of the host film influences the degree of charge transfer [78]. There, the authors compared the doping of regioregular against regiorandom P3HT (chemical structure in figure A.1) by F4TCNQ at different doping concentrations and attributed the observed differences in doping behavior between regioregular and regiorandom P3HT, to variations in the local energetic environment caused by the different polymer chain arrangements. Specifically, the density of states (DOS)-onset (IE) of re-

[†]see chemical structure in figure 2.5. Note that P3HT in this thesis refers specifically to regioregular P3HT, unless stated otherwise.

[‡]see figure 2.5 for chemical structure.

gioregular P3HT is energetically favourable for ICT with F4TCNQ. This onset is defined by the low-IE crystalline states. However, as the states form merely a ‘tail’ to the DOS of regiorandom P3HT, its onset is practically shifted to higher IE, rendering ICT with F4TCNQ effectively unfavourable [78]. Their analysis suggests that in semi-crystalline films, F4TCNQ preferentially dopes the crystalline regions due to their lower IE and the close backbone packing that limits dopant diffusion into amorphous phases [78].

The microstructure of the OSC has been reported to influence the overall doping efficiency and, hence, the electrical conductivity of the doped film [74–77]. Semi-crystalline polymers, such as P3HT, have distinct values for energy gaps and ionization potentials between their amorphous and crystalline domains as a result of variation in conjugation length [96]. P3HT with mainly amorphous domains, like in regiorandom P3HT, is characterized by a wider energy gap and higher ionization energy, and is, therefore, less prone to ionization compared to their crystalline counterparts, such as in regioregular P3HT [74, 97]. Consequently, charge carriers tend to localize preferentially within the crystalline regions. Tie-chains, or inter-connected polymer chains that link adjacent crystalline domains, facilitates charge transport in CP films by providing a physical connection between them [74, 97]. The influence of processing techniques on microstructure and subsequent doping efficiency is evident from a study by Jacobs et al. where films established from common P3HT–F4TCNQ solution and sequentially doped films, i.e., P3HT films exposed to the dopant from orthogonal solution relying on interdiffusion of the dopant, show significantly distinct microstructures [76]. There, sequential doping retains the higher structural film quality. Furthermore, charge transport in P3HT is highly anisotropic, with mobility primarily governed by the degree of order within the π -stacking direction, rather than along the alkyl side-chains [74, 97]. This anisotropy highlights the importance of understanding the relationship between molecular packing and charge transport pathways.

While previous studies provide valuable insights into doping and charge transport in semi-crystalline P3HT, decoupling the specific contributions of amorphous and crystalline phases remains a challenge [78, 80, 98]. Understanding the interplay between doping mechanisms, microstructure, and charge transport is crucial for optimizing the performance of organic semiconductors. Hence, controlled processing techniques that allow for the fabrication of CP films with well-defined morphologies are essential. Importantly, such techniques typically focus on *increasing* structural quality, e.g., by post-fabrication thermal annealing [99], solvent-vapor annealing, [100] epitaxial growth on anisotropic substrates, [101] self-seeded growth, [102], high-temperature rubbing (HTR) [103], or by exploiting the CP molecular weight, [104], of the semi-crystalline polymer, while deliberately *minimizing* structural order to establish amorphous films is no common approach followed in literature. Having purely amorphous P3HT samples would be, however of great use to, e.g., disentangle the doping phenomenology of semi-crystalline films. Chapter 4 of this thesis aim towards controlling the microstructure of P3HT film via *high-vacuum electrospray deposition* (HV-ESD, see section 3.1.2 for working principle), which is a highly unconventional technique for CP deposition. Section 4.1 of chapter 4 provides a comprehensive discussion on advantages of HV-ESD technique over conventional solution processing techniques, such as spin coating, for depositing CP thin films.

In addition to investigating the microstructure of P3HT deposited by HV-ESD, this

thesis also delves into exploring the structural and optical properties of OSCs and OSC blends. Complementing the overarching theme of microstructure control in organic semiconductors, we focused on vacuum co-evaporated equimolar blends of rod-like COMs, specifically α -sexithiophene (6T) and para-sexiphenyl (6P), both of which are among the most widely studied OSCs. Building upon previous reports [8, 105–111] of mixed crystal growth and unique emission properties in layered heterostructures of these molecules, we investigated whether similar phenomena translate into vacuum co-crystals. This study provides insights into the influence of molecular packing and intermolecular interactions on the optical properties of COM blends, here, for highly crystalline structures, contrasting the other extreme of amorphous P3HT established by HV-ESD.

There are three specific aims of this thesis, that are summarized as below-

1. **Establishing a reliable protocol for HV-ESD of CPs:** HV-ESD is a highly unconventional method for depositing CP thin films compared to well-established solution-processing techniques such as spin-coating, dip-coating, and inkjet printing, among others. ESD was a new technique in our lab, therefore, the first milestone in my research work was to commission the experiment and establish a reliable protocol for depositing CPs in-vacuo. There, it was key to investigate the impact of numerous experimental parameters such as solvent type, injection rate, applied voltage, substrate nature, solution concentration, and film deposition time on the resulting film properties in HV-ESD. This aim is a part of chapter 4.
2. **Investigating the microstructure of polymer thin films deposited via HV-ESD:** After establishing a reliable protocol for film deposition by HV-ESD, our next goal is to investigate the microstructure of P3HT films that were deposited from gas phase ions under minimum solvent influence via HV-ESD. This has again been highlighted in chapter 4.
3. **Exploring the structural and optical properties of a co-evaporated equimolar blend of rod-like organic molecules:** The reports on heterostructures of rod-like COMs of similar shape and size, such as 6P and 6T, indicated mixed crystal growth in equimolar blends [112]. The emission properties of 6P/6T hetero-stacks were reported to depend on the stacking distance. Because of this, their emission could be tuned from yellow and red via white to blue [8, 105, 106]. Such an emission behaviour is observed because of spectral overlap between 6P emission and 6T absorption. This results in resonant energy transfer between these molecules. The charge transfer between 6T and 6P in their hetero-stacks was excluded based on photoemission spectroscopy [106]. Here, we aimed to investigate if similar mixed crystal growth is seen in co-evaporated films. More importantly, the optical properties, seen in layered stacks of 6T and 6P, also translate into their vacuum codeposited co-crystals. The results from this study have been presented in chapter 5

The structure of this thesis is as follow:

Chapter 2 explores the fundamental concepts of organic semiconductors, introducing their optoelectronic properties and doping mechanisms, as well as the effect of microstructure. This chapter aims to establish a robust theoretical framework that supports the discussions that follow.

Chapter 3 details practical aspects of sample preparation methods used to fabricate thin films of COMs and CPs throughout the thesis. This chapter also explains the experimental techniques employed to analyze and characterize the structural and optical properties of the films.

Chapters 4 and **5** discuss the main results and findings of the thesis, which have been published as first-author manuscripts in peer-reviewed journals [17, 20]. Chapter 4 delves into depositing P3HT films minimizing solvent influences by using HV-ESD and investigates the microstructure of vacuum-electrosprayed P3HT films. Chapter 5 probes the optical and structural properties of crystalline blends of 6T and 6P.

Chapter 6 showcases the results of ongoing research related to the current theme of this thesis, which have not yet been published. This chapter delves into additional research on the p-doping of OSCs which I have done during the past years, thus complementing the core focus of this thesis and outlining future directions. The chapter explores the relationships between chemical structure, electronic properties and structural properties in the molecular electrical p-doping of various conjugated systems including oligothiophenes, benzothieno[3,2-b]benzothiophene derivatives, and P3HT, with molecular dopants like FxTCNQ (lesser fluorinated derivatives of F4TCNQ[§]), and Lewis acids[¶]. These investigations are ongoing and provide valuable new insights into these aspects and will be subject of future publications planned for the near future to which I will contribute.

Finally, the significant findings and insights derived from this research are comprehensively summarized in **chapter 7**.

[§]see chemical structure in figure A.2

[¶]refer to figure A.3 for chemical structure

Chapter 2

Fundamentals of Organic Semiconductors

2.1 Organic Semiconductors

OSCs are hydrocarbon based compounds that may contain other heteroatoms such as nitrogen, oxygen, sulphur, phosphorus or fluorine among others. OSCs are characterized by their π -conjugated system, which entails the delocalization of electrons across overlapping p-orbitals. This delocalization is often represented as alternating single and double bonds, primarily dictated by the sp^2 hybridization of the carbon atoms in conjugated systems [51, 113]. OSCs are sub-divided into two main groups depending on their chain length, organic molecules (COMs) and conjugated polymers (CPs).

2.1.1 Inorganic *versus* Organic Semiconductors

Inorganic semiconductors (ISC) such as silicon, are composed of atoms that are bonded by strong covalent or ionic bonds, forming a rigid crystalline lattice with periodic unit cells. This strong bonding results in distinct energy band dispersion and high carrier mobilities in ISCs. In contrast, weaker Van der Waals and electrostatic forces responsible for the OSC packing result in less ordered structures with much weaker electronic coupling between the molecules, which in turn leads to typically very low energy band dispersion and much lower charge carrier mobilities [51, 114]. Additionally, ISCs are composed of isotropic atoms, while most OSCs consist of anisotropic molecules. This anisotropy significantly influences the packing arrangement and orientation of molecules within the (bulk) material and accordingly impacts charge transport properties in OSCs which can be also be highly anisotropic [74, 97, 115]. For example, different polymorphs of the same OSC could exhibit dramatically different charge carrier mobilities because of the different molecular packing [116, 117].

ISCs are dominated by strong covalent bonds between neighbouring atoms, which make these materials typically hard, brittle and thermally stable, while the OSC packing due to Van der Waals and electrostatic forces make them softer, more flexible and is reflected in much lower melting points [1, 51]. These differences in the nature of organic

and inorganic semiconductors bring advantages and disadvantages to each of the two material classes. For example, the high charge carrier mobilities and thermal stability of ISCs are beneficial for high-performance device applications, whereas the flexibility, low-temperature and solution processibility as well as tunable optoelectronic properties through chemical modifications of OSCs make them attractive for applications in flexible and printed electronics.

2.1.2 Electronic Structure of Organic Semiconductors: From Molecules to Solids

The interference of electronic wavefunctions of the individual atomic orbitals and their linear combinations forms molecular orbitals. Constructive interference leads to *bonding* molecular orbitals (σ or π), characterized by increased electron density between the bonding nuclei. Conversely, destructive interference results in *anti-bonding* molecular orbitals (σ^* or π^*), with reduced electron density between nuclei, resulting in increased electrostatic repulsions. Therefore, the bonding orbitals have lower energy and participate in the ‘bonding’ between the atoms while anti-bonding molecular orbitals are found at higher energy and do not contribute to the ‘bonding’ process [1, 118]. For organic semiconductors, sp^2 hybridization of carbon is of great relevance. The ground state elec-

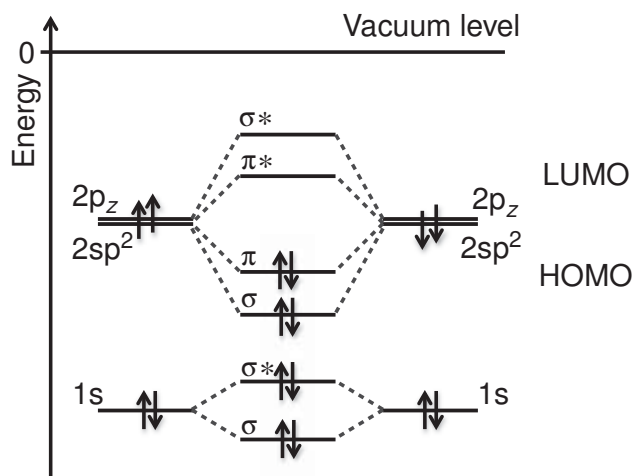


Figure 2.1: Diagram illustrating the energy levels of σ and π -bonds formed from the atomic orbitals of carbon atoms in ethene. For clarity, the $2sp^2$ orbitals involved in σ -bonding with hydrogen atoms are not shown. The energy scale represents the kinetic energy of a free electron, thus orbital energy levels are displayed as negative values corresponding to their binding energies.

Figure taken from [1] A. Köhler and H. Bässler, *Electronic Processes in Organic Semiconductors: An Introduction*. Weinheim: Wiley-VCH, 2015. Copyright 2015 Wiley-VCH Verlag GmbH & Co. KGaA.

tronic configuration of carbon is expressed as $1s^2 2s^2 2p^2$, with four valence electrons occupying the 2s and 2p (further detailed as $2p^1_x$, $2p^1_y$, and $2p^0_z$) orbitals. This allows the carbon atoms to readily undergo hybridization by combining its 2s and 2p orbitals.

In sp^2 hybridization, one 2s orbital and two 2p orbitals of carbon hybridize to form three coplanar degenerate sp^2 orbitals separated by 120° degrees, leaving a third unhybridized p_z orbital in a direction perpendicular to sp^2 hybridized plane. When two sp^2 hybridized carbon atoms approach each other, one sp^2 orbital from each atom overlaps directly, to form a strong σ -bond. Simultaneously, the non-hybridized p_z orbitals from each carbon atom, extending above and below the plane, overlap sideways to create a π -bond. The electrons in the π -bond are delocalized over the entire system of overlapping p_z orbitals. This delocalized electron density is a key characteristic of *conjugated* systems [118, 119]. In sp^2 hybridized carbon atoms, the weaker overlap between p_z orbitals results in smaller energy difference between *bonding* π and *anti-bonding* π^* orbitals compared to the larger difference between *bonding* σ and *anti-bonding* σ^* orbitals. Figure 2.1 shows the σ and π -bond formation between the carbon atoms of ethene. In the ground state, *bonding* π and *anti-bonding* π^* orbitals are known as the *highest occupied molecular orbital* (HOMO) and *lowest unoccupied molecular orbital* (LUMO), respectively for OSCs [113, 120]. The HOMO and LUMO are termed frontier molecular orbitals as the energy difference between HOMO and LUMO constitutes the energy gap of OSCs, they are crucial to essentially all relevant optical and electronic properties of OSCs exploited in applications. Furthermore, the experimentally determined ionization energy (IE) is connected with the energy required to remove an electron from the HOMO of a molecule. Likewise, the electron affinity (EA) is linked with the energy gained when adding an electron to the LUMO of a molecule [48, 121, 122]. When electron-donating or electron-withdrawing substituents are attached to the conjugated portion of the OSCs, they can either raise or lower the HOMO or LUMO levels, respectively [120, 121]. Consequently, substitution provides the ability to tune the energy gap of OSCs. The energy gap of OSCs is also influenced by the *conjugation length* of COMs and CPs. Specifically, increasing the length of the π -conjugated system decreases the energy gap, as observed, e.g., in the acene series [51] (benzene, naphthalene, anthracene, etc.) or for oligo- to polythiophene as recently shown in our group [12]. While this inverse relationship between *conjugation length* and the energy gap is straightforward in COMs, in CPs, this would imply the absence of a bandgap due to their infinitely large number of sp^2 hybridized carbon atoms. Contrary to this, CPs do not show any metal-like behaviour, due to a phenomenon called *Peierls distortion* [123]. For example, If we consider polyacetylene in its ‘trans’ configuration, then *Peierls distortion* results in alternating shorter and longer bond lengths, schematically drawn as alternating single and double bonds. Accordingly, the initially half-filled π -band splits into two sub-bands, π and π^* , where the π sub-band would be filled, and π^* sub-band would be empty, thus introducing a finite energy gap ~ 1.5 eV in trans-polyacetylene. Hence, the *Peierls distortion* imparts semiconducting properties to CPs [123]. Moreover, several factors can interrupt the conjugation length– which dictates the spatial extent over which the π -electron can delocalize coherently [1], along the polymer backbone. These factors include– chemical impurities, torsional disorder, chemical defects and the presence of different conformations. The effective conjugation length of CPs influences their semiconducting behaviour [1].

2.1.3 Optical Properties of Organic Semiconductors

In the previous subsection 2.1.2 we discussed the electronic structure of OSCs. Now in this subsection, we will consider their optical properties that are intricately related to their electronic structure. Beyond their electronic structure, molecules also possess vibrational and rotational energy levels, arising from the relative motion (rotation, vibration and translational) of their constituent nuclei, relative to one another [1, 113, 124]. The nuclei are oscillating around their equilibrium position with energy $E_{vib} = \left(n + \frac{1}{2}\right)\hbar\omega$, where n is the number of excited quanta, ω is the frequency of vibration and \hbar is the reduced Planck's constant [113, 121]. Now, by using *Born-Oppenheimer* approximation, it is possible to approximate the total wavefunction (ψ_{tot}) of a molecular state*, as the product of electronic[†] (ψ_{el}), spin[‡] (ψ_{spin}), vibrational[§] (ψ_{vib}) and rotational[¶] (ψ_{rot}) wavefunctions [1, 113]:

$$\psi_{tot} = \psi_{el} \psi_{spin} \psi_{vib} \psi_{rot} \quad (2.1)$$

Accordingly, the total energy of a molecular state can be given as:

$$E_{tot} = E_{el} + E_{spin} + E_{vib} + E_{rot} \quad (2.2)$$

where E_{el} , E_{spin} , E_{vib} and E_{rot} are the energies of electronic, spin, vibrational and rotational states, respectively. The energy difference between electronic states is typically $\sim 1\text{--}5\text{ eV}$ and between vibrational states is $\sim 100\text{--}300\text{ meV}$ [1]. The contributions from E_{rot} (relevant in the gas phase only) and E_{spin} are very small therefore they are generally neglected in equation 2.2. Thus, each electronic state has a set of vibrational states and within each vibrational states, there exists a set of rotational states [1, 113, 121]. The oscillations of atoms within a molecule can be thought of as a system of coupled oscillators, which is mathematically described using normal mode coordinates (Q_i). These coordinates are derived from the individual nuclear coordinates (R_i) and represent collective motions where all atoms vibrate at the same frequency. If a slice is taken through the potential energy surface along a specific normal mode coordinate (Q_i), we get a potential energy curve for each electronic state and the quantized vibrational states are then represented as horizontal lines on this slice [118, 125], as illustrated in figure 2.2. As a result of *Born-Oppenheimer* approximation, the optical transitions between the potential energy curves, of ground and excited states, are indicated by vertical straight lines; implying that the nuclei position stays stationary during these transitions. This is known as the *Franck-Condon principle* [125].

When a molecule absorbs a photon, it can undergo a transition from the lowest vibrational level of its electronic ground state to various vibrational levels of an excited electronic state. The probability of a particular transition is dictated by the overlap between

*This description of ψ_{tot} is possible by *Born-Oppenheimer* approximation because electrons move faster than the nuclei as a result of relatively large mass difference between them; therefore the wavefunctions of the electrons and nuclei can be described separately in very good approximation.

[†]electronic wavefunction is a function of electron's spatial coordinates and the nuclei.

[‡]spin wavefunction is a function of electron's spin.

[§]vibrational wavefunction describes the vibrational motion of the nuclei.

[¶]rotational wavefunction is a function of rotational motion of a molecule as a whole.

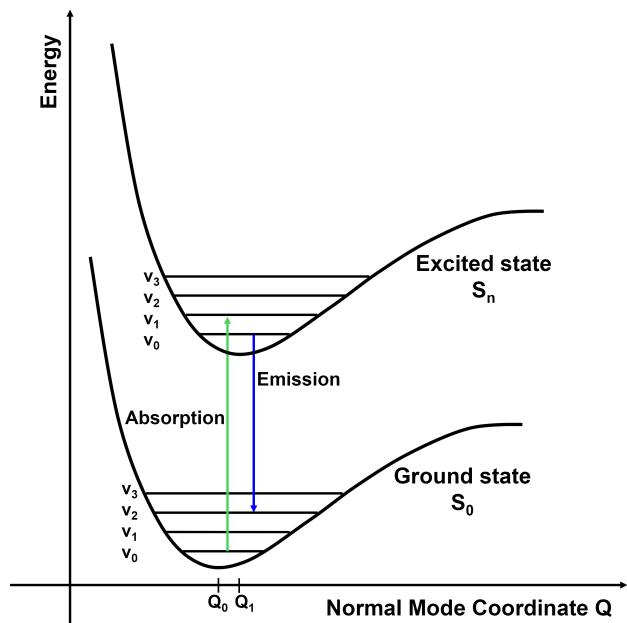


Figure 2.2: Potential energy curves of a molecule described as a function of the normal mode coordinate Q , showing the vibrational levels within the energy levels. Each energy level ($S_0, S_1 \dots S_n$) has vibrational sub-levels ($\nu_0, \nu_1 \dots \nu_n$) that are represented by the horizontal lines.

the vibrational wavefunctions of the initial and final electronic states [1, 118]. Following the excitation, the molecule is likely to undergo rapid vibrational relaxation, involving transition from the higher to the lowest vibrational level of the excited electronic state. From that relaxed state, the molecule can return to the electronic ground state by emitting a photon. This phenomenon is known as fluorescence; where the emitted photon generally has lower energy (longer wavelength) than the absorbed photon. According to *Kasha's rule* [126], fluorescence usually takes place from the lowest vibrational level of the excited state, which is why the transitions in the emission spectrum terminate on a various vibrational levels in the electronic ground state [125–127]. The distinct transition pathways for absorption and emission are governed by the *Franck-Condon principle* and *Kasha's rule* and together they give rise to the *Stokes shift*. This shift represents the energy difference between the peak maxima in the absorption and emission spectra. Typically, the emission spectrum appears at lower energies (longer wavelengths) compared to the absorption spectrum [125, 127].

The rate of absorption or emission transition (k_{if}) between the initial (i) and final (f) electronic states is given by the number of transitions occurring per second. Using the quantum mechanical approach, if we consider a system initially described by a Hamiltonian \hat{H}_0 , which experiences a small perturbation \hat{H}' , then the rate of transition (k_{if}) between an initial state (Ψ_i) and a final state (Ψ_f) [1, 118, 125] can be given by *Fermi's Golden rule* [128, 129] as:

$$k_{if} = \frac{2\pi}{\hbar} |\langle \Psi_f | \hat{H}' | \Psi_i \rangle|^2 \rho \quad (2.3)$$

where \hbar is the reduced Planck constant, $|\langle\Psi_f|\hat{H}'|\Psi_i\rangle|^2$ represents the strength of the coupling between the initial and final states due to the perturbation, ρ is the density of final states available for the transition. In the context of transitions resulting from the absorption or emission of light, the perturbation stems from the interaction between the molecule's electric dipole moment and the oscillating electric field of electromagnetic radiation [1, 118]. Therefore, we can express the perturbation Hamiltonian using the electric dipole operator, $\hat{\mu} = e\hat{r}$, where e is the elementary charge and \hat{r} is the position operator. For a molecule, as illustrated by equation 2.1, the total wavefunction can often be separated into electronic, vibrational, and spin components. Therefore, using equation 2.1 and considering that the electric dipole operator primarily affects the electronic wavefunction, equation 2.3 can be written [1, 118, 121] as:

$$k_{if} = \frac{2\pi}{\hbar} \rho |\langle\Psi_{el,f}|e\hat{r}|\Psi_{el,i}\rangle|^2 |\langle\Psi_{vib,f}|\Psi_{vib,i}\rangle|^2 |\langle\Psi_{spin,f}|\Psi_{spin,i}\rangle|^2 \quad (2.4)$$

This equation reveals that the rate of an optical transition between the initial and final states would be higher if there is a significant overlap between the orbitals involved in the transition, between the vibrational wavefunctions and if the spin of the two states remains conserved during these transitions [1, 113, 118]. Transitions between states of different parity (odd–even or even–odd) and different spin (singlet–triplet states) are forbidden. If any factor in the expression becomes zero, the corresponding transition is deemed ‘forbidden’ [1, 113].

So far, we have considered the electronic transitions of a single molecule. However, if two or more molecules are close together, such as in molecular aggregates, their electronic states can interact and lead to significant changes in their optical properties, e.g., giving rise to excited states that are delocalized over more than one molecule through excitonic coupling [130–134]. The absorption or emission of light by a molecule involves the interaction of its transition dipole moment with the electromagnetic field. Not surprisingly, when two molecules, each with an equal magnitude of transition dipole moment $\vec{\mu}$, are in close proximity, their transition dipole moments $\vec{\mu}$ can interact constructively or destructively relative to each other [130–133]. This translates into a net transition dipole moment for the system, which is the vector sum of the individual molecular transition dipole moments. The magnitude and direction of $\vec{\mu}_{net}$ are critically dependent on the relative orientation of the interacting molecules. Depending on the relative orientation of the individual dipole moments, two extreme cases of molecular aggregates, *H-aggregates* and *J-aggregates*, and an intermediate case of *oblique orientation* of transition dipoles arise, each characterized by distinct optical properties [113, 130–133].

According to the molecular exciton model [135], electronic interactions between two identical molecules (M_1 and M_2) lead to the splitting of their excited state. This splitting arises from the coupling of their transition dipole moments [113, 130, 131, 133, 136], as illustrated in figure 2.3. We can label these new energy sub-levels as higher energy E_+ and lower energy E_- . In *H-aggregates*, the molecules are arranged in a coplanar, stacked configuration, often described as a side-by-side arrangement [134]. In such an arrangement [figure 2.3(a)], the transition dipole moments align antiparallel relative to each other, for the E_- state, resulting in a ‘zero’ net transition dipole moment. Conversely, E_+ state exhibits parallel orientation of individual transition dipole moments, leading to a net

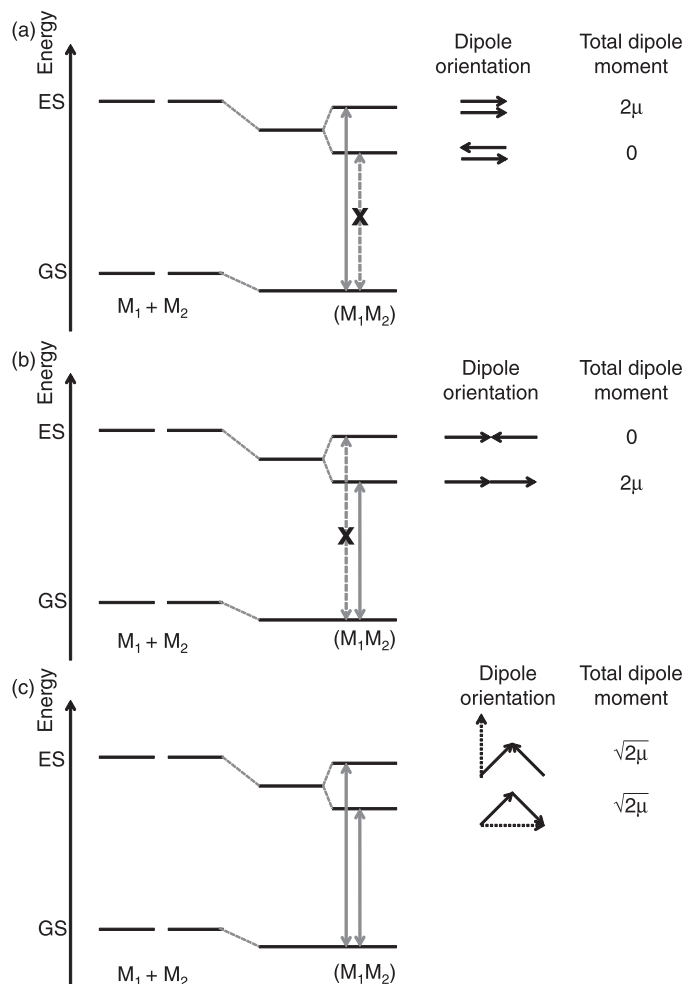


Figure 2.3: Figure visually representing the energy levels of the ground (GS) and excited states (ES) for both two isolated molecules (M_1 and M_2) and a pair of electronically coupled molecules (M_1M_2). For M_1M_2 coupled molecules, the ES splits into a lower ES (E_-) and higher ES (E_+) (not marked in the figure). The coupled molecules are depicted in three distinct spatial arrangements: (a) side-by-side representing H-aggregates, (b) head-to-tail leading to J-aggregates, and (c) a case for oblique alignment of isolated molecules relative to each other. For each configuration, the figure highlights the relative alignment of the excited state transition dipoles, potential optical transitions, and the magnitude of the resulting total transition dipole moment.

Figure taken from [1] A. Köhler and H. Bässler, *Electronic Processes in Organic Semiconductors: An Introduction*. Weinheim: Wiley-VCH, 2015. Copyright 2015 Wiley-VCH Verlag GmbH & Co. KGaA.

transition dipole moment of $2\vec{\mu}$, i.e. twice the magnitude of individual dipole moment [113, 130, 131, 133, 136]. As dictated by the selection rule, any optical transition for which the product of ψ_{el} , ψ_{vib} and ψ_{spin} would be zero (see equation 2.4) is forbidden [1]. Consequently, any transition to and from E_- would be forbidden. In contrast, transitions involving the E_+ state are allowed. Absorption in *H-aggregates* occurs primarily

at the higher energy E_+ state, leading to a *hypsochromic* shift (blue shift) in the absorption spectrum compared to the isolated molecule [130, 131, 133, 134, 136]. Emission from *H-aggregates* is typically weak or absent. This quenching arises because relaxation after excitation usually leads to the lowest excited state (E_-). Since transitions from E_- are forbidden, radiative decay is suppressed, and energy dissipation occurs primarily through non-radiative pathways [1, 113, 130, 131, 133, 134, 136].

On the other hand, *J-aggregates* are characterized by a sequential, co-linear, and parallel arrangement of molecules or, in other words, end-to-end arrangement of molecules [134]. In this configuration, the parallel alignment of transition dipole moments would result in a net dipole moment of $2\vec{\mu}$ for E_- ; while the net dipole moment for E_+ would be zero due to antiparallel orientation of the dipole moment [see figure 2.3(b)]. Consequently, absorption in *J-aggregates* occurs predominantly to the E_- state [113, 130, 131, 133, 136], resulting in a *bathochromic* shift (redshift) in the absorption spectrum compared to the isolated molecule. Furthermore, *J-aggregates* often display enhanced and red-shifted emissions [134, 137–139].

When π -bonded molecules are arranged at arbitrary angles, their interactions differ from the extreme cases of *H-aggregates* and *J-aggregates*. In such instances, the absorption spectrum of isolated molecules (M_1 and M_1) often splits into a doublet, as both higher and lower energy transitions gain a certain degree of oscillator strength where the intensity ratio of these doublet components depends on the vector sum of the monomer moments [1, 113] [refer to figure 2.3(c)]. For this type of aggregates, the emission spectrum typically originates from the lower energy state of this dimer and exhibits a lifetime one to two orders of magnitude longer than that of the individual isolated molecules [1, 113].

2.2 Structural to Energetic Disorder in Organic Semiconductors

One key difference between OSCs and their inorganic counterparts are the discrete energy levels of the former, which is a direct consequence of the weak Van der Waals interactions responsible for their solid state packing, that renders the electronic structure of the solid molecule-like, and band dispersion is only observed in rare cases [140, 141]. Further, this makes them prone to exhibit structural disorder sensitive to the preparation conditions [142]. This disorder profoundly influences the energetic landscape of OSCs, directly impacting charge transport and, ultimately, the performance of organic electronic devices.

Charge transport in disordered OSCs is well described by a thermally activated hopping mechanism, where charge carriers move through the material by hopping between neighboring molecules (i.e., their adjacent molecular orbitals). [115, 143, 144]. The efficiency of charge transport is dictated by the electronic coupling between neighboring molecules [77, 115]. In a disordered system, where the molecules would be randomly arranged w.r.t. each other, consequently, their intermolecular distances and orientations would be randomly distributed. These variations directly impact the degree of wavefunction overlap of molecular orbitals, leading to a distribution of electronic coupling

strengths [77, 115]. Therefore, structural disorder results in a heterogeneous landscape for charge transport, structural disorder translates into energetic disorder of the solid [77, 145].

The inherent flexibility of most OSC molecules, particularly conjugated polymers, leads to variations in conjugation length. As previously discussed in subsection 2.1.2, torsional disorder and chemical defects in the molecular backbone disrupt the extent of delocalization of the π -electron cloud, creating segments with varying conjugation lengths and, consequently, different energy gaps between HOMO and LUMO. This results in a broadened density of states (DOS) with a Gaussian distribution of the HOMO and LUMO DOS, as a testimony of energetic disorder [93, 146]. Beyond creating a broadened DOS, structural disorder can introduce deep traps for charge carriers that are highly localized, i.e., low-energy states that can trap charge carriers for extended periods [115, 147]. These traps, also arising from significant chemical defects or impurities [145, 147], act as bottlenecks for charge transport, further hindering device performance [148–150].

The presence of charge carriers induces electrostatic polarization in the surrounding molecular environment, influencing the energy levels of nearby molecules. In disordered OSCs, the irregular molecular arrangement, thus, leads to variations in local polarizability. This variation in polarization response further contributes to energetic disorder, as charge carriers experience different polarization energies depending on their location. [1]

Understanding processing conditions that cause energetic disorder and mitigating it is crucial in optimizing OSC-based devices. Therefore, controlling the nano- and microstructure of OSC films, particularly by minimizing structural defects and enhancing molecular ordering, is paramount [142]. Minimizing energetic disorder enables more efficient charge transport, ultimately paving the ways to unlocking the full potential of OSCs in a wide range of electronic applications. For a detailed discussion on the microstructure–property relationship, interested readers are encouraged to refer to the review article by Rivnay et al. [142].

2.3 Doping of Organic Semiconductors

Doping in ISCs played a crucial role in the development of the bipolar transistor and the creation of p-n junctions. In ISCs, doping is achieved by adding controlled amounts of atomic impurities, for example, adding atomic impurities like boron in Si, is a well-known process for p-type doping in Si, where the majority of the carriers are holes. Doping in ISCs allows tuning of Fermi level, charge carrier concentration and precisely controlling their conductivity. Thus, doping was a significant breakthrough in the evolution of ISC technology. The success of doping in ISCs led researchers to apply a similar approach to the emerging field of OSCs. However, due to their weaker intermolecular interactions, doping in OSCs has its challenges. Unlike in ISCs, the dopants are not covalently bonded in OSCs; therefore, the small atomic dopants have the tendency to diffuse through the layers of OSCs. Consequently, the devices based on doped OSC films suffer from instability and degradation of device performance. For this reason, OSCs are preferably doped with larger molecular dopants. Due to their larger size, molecular dopants are not as prone to diffusion as small atomic dopants, thus leading to enhanced device stability.

Molecular dopants engage in charge transfer interactions with the host OSC molecules to generate mobile charge carriers (holes for p -type doping and electrons for n -type doping). Just like in ISCs, the overall goal of doping in OSCs is to tune their electronic properties for desired applications, even though the fundamental doping mechanisms in ISCs and OSCs are entirely different. Nonetheless, the doping mechanism in OSCs is an active area of research and is less well-established than the mechanisms of doping in crystalline ISCs.

2.3.1 Doping with Molecular Dopants

Molecular dopants have been found to dope OSCs by two distinct mechanisms: (i) *fractional* charge transfer (FCT) between OSC and dopant as the result of formation of ground-state *charge-transfer complexes* (CTCs), (ii) the formation *ion-pairs* (IPAs), i.e. spatially separated OSC–dopant ions due to integer charge transfer (ICT). Here, both these mechanisms will be explained in light of p -doping in OSCs. During IPA formation, an electron is accepted into the $LUMO_{dopant}$ from $HOMO_{host}$. Consequently, a (mobile) hole is generated in the host matrix, and a localized charge remains on the dopant. Therefore, the condition that arises for IPA is that the EA_{dopant} must be greater than or at least equal to IE_{host} . In contrast, upon CTC formation, the frontier molecular orbitals of host and dopant overlap to form a new set of supramolecular hybrid orbitals. The *new* hybridized HOMO (CTC_{HOMO}) is doubly occupied while the *new* LUMO (CTC_{LUMO}) is unoccupied, where CTC_{LUMO} lies at *lower* binding energy than the dopant LUMO. The IPA and CTC formation phenomena of p -doping of OSC are shown in figure 2.4. In terms of IE and EA this means that, e.g., while $IE_{host} = EA_{dopant}$, the IE of CTC_{HOMO} is at lower binding energy than EA_{dopant} whereas the EA of CTC_{LUMO} is at higher binding energy than both the IE_{host} and EA_{dopant} . Accordingly, the transition between CTC_{HOMO} and CTC_{LUMO} is of lower energy and observed as sub-gap absorption appearing regarding the fundamental energy gap of the host OSC. As both electrons reside in CTC_{HOMO} , CTC formation results in an energy barrier that needs to be overcome to generate a mobile charge carrier, that is, promoting an electron into CTC_{LUMO} from the HOMO of the surrounding OSC matrix. In other words, the CTC takes over the role of the dopant, but its EA is lower than that of the pristine dopant and represents therefore a parasitic process that must be inhibited for optimizing OSC doping. We showed recently that this can be achieved by exploiting steric hindrance, that was introduced by adding bulky sidegroups to a dopant functional core to reduce intermolecular coupling [19].

For this reason, CTC formation is considered to be detrimental to doping efficiency. While the formation of CTCs in doped systems has historically been considered as generally undesirable, recent literature suggests that moderate CTC concentrations, relative to IPA, can actually be beneficial for device performance. The reports claim that carefully controlled CTC-to-IPA ratios can lead to improvements in the performance of organic thermoelectric devices [151], organic field-effect transistors [152] and organic light-emitting diodes [153]. Both IPA and CTC formation can be identified from their signature in ultraviolet-visible-near infrared (UV-vis/NIR) spectroscopy (due to the new absorptions in the sub-gap), and Fourier transform infrared (FTIR) spectroscopy (due to characteristic changes in vibrational modes of the charged dopant). For example, the pro-

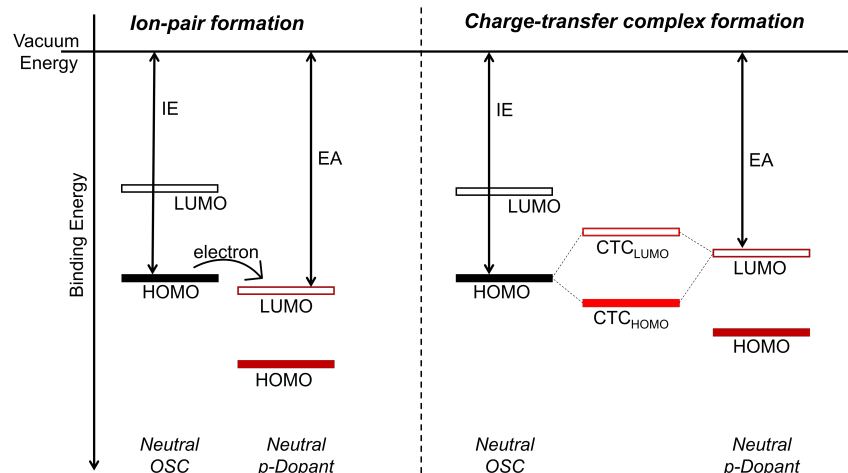


Figure 2.4: Illustration showing energy levels during IPA and CTC formation in p-doping of OSC.

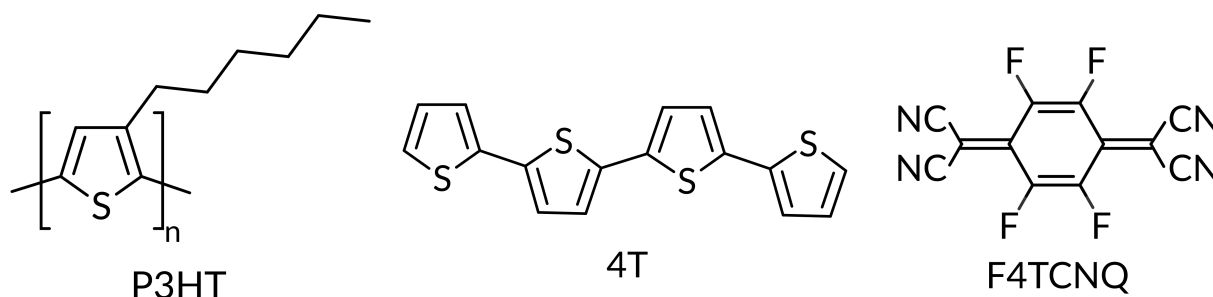


Figure 2.5: Skeletal structures of regioregular poly(3-hexylthiophene-2,5-diyl) (P3HT), α -quaterthiophene.

totypically studied host-dopant system for p-doping is P3HT and strong electron acceptor molecular dopant F4TCNQ. The chemical structure of P3HT and F4TCNQ is depicted in figure 2.5. In the case of IPA, the UV-vis/NIR spectrum shows characteristic peaks from the F4TCNQ radical anion around 1.6 eV, 1.4 eV and broad polaronic features (cations on a segment of the P3HT chains) below 1.8 eV [53, 154]. The C \equiv N stretching vibrations of F4TCNQ are known to be very sensitive to its intermolecular environment [155, 156] and charged state. From FTIR, the degree of charge transfer (δ) between the host and dopant can therefore be estimated by calculating the shift ($\delta\nu$) of C \equiv N stretching vibration of F4TCNQ via:

$$\delta = \frac{2\delta\nu}{\nu_0} \left[1 - \frac{\nu_1^2}{\nu_0^2} \right]^{-1}, \quad (2.5)$$

where ν_0 and ν_1 is the frequency of C \equiv N mode in neutral and negatively charged state of F4TCNQ, respectively [157]. The neutral F4TCNQ, C \equiv N stretching vibrations appear at 2227 cm $^{-1}$ which shifts to 2194 cm $^{-1}$ when it's negatively charged (in the presence of P3HT). This gives $\delta=1.0$ meaning 1 electron is transferred from P3HT to F4TCNQ. Thus,

IPA is responsible for generating mobile charge carriers in doped OSCs and leads to *integer charge transfer* between host HOMO and dopant LUMO [53, 90, 154]. Note, however, that shifts in the C≡N stretching vibrations can be influenced by external influences such as the molecular environment and using above relation can be misleading for some systems, which has been analyzed by density-functional theory (DFT) based modeling recently in our group for a number of p-dopants [158].

In contrast, for the case of CTC formation, like in α -quaterthiophene (4T) (chemical structure in figure 2.5) doped with F4TCNQ, a sub-gap absorption below 1 eV is observed, which comprise the $S_0 \rightarrow S_1$ transition of the CTC. FTIR reveals that the complex between 4T and F4TCNQ corresponds to a degree of charge transfer of $\delta = 0.2$ electrons to F4TCNQ [90]. So, CTC formation leads to *fractional charge transfer* between the host and the dopant, which is not desirable due to the modified electronic structure (see above) that makes charge transfer to the CTC_{LUMO} energetically less favorable than for the pristine dopant.

A simple Hückel-like model can capture the experimentally observed values for the modified gap of the CTC well [90]. There, the CTC energy gap E_{gap}^{CTC} , i.e., the energy separation between CTC_{HOMO} and CTC_{LUMO} is dependent on the energies of host HOMO (E_{HOMO}^{host}), dopant LUMO (E_{LUMO}^{dopant}) and resonance integral ' β '-

$$E_{gap}^{CTC} = \frac{E_{HOMO}^{host} + E_{LUMO}^{dopant}}{2} \pm \frac{1}{2} \sqrt{(E_{HOMO}^{host} - E_{LUMO}^{dopant})^2 + 4\beta^2}, \quad (2.6)$$

where ' β ' defines the extent of electronic coupling between the host and dopant frontier molecular orbitals. Therefore, CTC formation can, in principle, occur if E_{LUMO}^{dopant} is lower or higher than E_{HOMO}^{host} . In other words, better overlap between $HOMO_{host}$ and $LUMO_{dopant}$ implies that the system will be more susceptible to CTC formation. Recently, it was reported that by changing the processing conditions, CTC formation could be induced in systems like P3HT doped with F4TCNQ, which were earlier known to show exclusively IPA formation, here, mediated by a unique microstructure of cofacially aligned dopant and polymer backbone. [80] Accordingly, CTC and IPA formation are two competing mechanisms where which factors favours one over the other, are subject to ongoing research efforts in the community.

Chapter 3

Methods

This chapter showcases the physical processes involved in the techniques employed for preparing the thin films of COMs and CPs. Later on, the experimental techniques used to characterize the thin films (of CPs and COMs) will be explained.

3.1 Sample Preparation

The thin films of COMs and CPs used in chapters 5 and 4 were deposited in *in-vacuo* using thermal sublimation and electrospray deposition techniques, respectively. Details about specific deposition parameters could be found in the respective chapters. For the chemical structure of P3HT, 6T and 6P refer to figure 2.5 and 5.1, respectively.

3.1.1 Vacuum Sublimation of Organic Molecules

Vacuum thermal sublimation, also sometimes referred to as molecular beam deposition, is a widely used technique for depositing thin films of organic molecules, with film thicknesses ranging from a few to hundreds of nanometers. The schematic of vacuum thermal deposition is shown in figure 5.8. In this technique, a (quartz) crucible containing the source material is resistively heated through a *constant* current flow. The rate of film deposition can be modified by changing the intensity of the current. A substrate is strategically positioned in the path of the molecular beam, where the evaporated molecules undergo condensation, forming a thin film. The rate and thickness of film can be precisely controlled with sub-Å precision using a *quartz-crystal microbalance*. The microbalance operates on the principle of mass-dependent variation in the resonant frequency of a ‘quartz crystal’. The material arriving onto the ‘quartz crystal’, induces a shift in its resonant frequency, which is directly proportional to the additional mass of the molecules arriving at the quartz crystal. The thin film growth via thermal sublimation is a dynamic, non-equilibrium process characterized by the simultaneous occurrence of several molecular-level events. These include, *nucleation, surface diffusion, dissociation* and *re-evaporation* [159]. During nucleation, the molecules aggregate to form a stable nuclei, that serve as the ‘seed’ for film growth. The movement of molecules across the substrate and growing film surface, which influences island formation and layer uni-

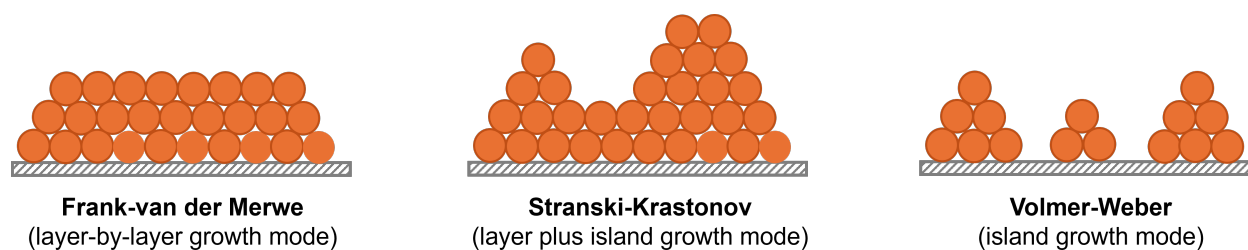


Figure 3.1: Schematic showing three different thin film growth modes during vacuum thermal sublimation.

formity is termed surface diffusion, whereas the potential breakdown of molecular assemblies that can impact the film morphology and properties is called dissociation. The desorption of molecules from the substrate or film surface into the vacuum is called re-evaporation and it has a direct effect on the growth rate [159]. The precise growth mode observed during thermal sublimation is primarily dictated by the substrate–molecule and molecule–molecule interactions, and typically three primary growth modes are observed—*Frank–van der Merwe* (‘layer-by-layer’ film deposition), *Volmer–Weber* (‘island growth’) and *Stranski–Krastanov* (‘layer-plus-island’) [160]. The schematic showing these three growth modes is shown in figure 3.1. In the *Frank–van der Merwe* or *layer-by-layer* growth mode, the dominant substrate–molecule interactions lead to the formation of complete closed layers—hence the name. However, if strong molecule–molecule interactions dominate to drive nucleation and growth of three-dimensional islands on a substrate, then this mode is called *Volmer–Weber*. Finally, in *Stranski–Krastanov*, layer-by-layer growth transitions to island mode after a few monolayers, termed as *wetting layer*. This intermediate mode occurs when substrate–molecule interactions decrease in strength with increasing film thickness and is quite common in the deposition of organic molecules on substrates with moderate interaction strengths. For example, on glass substrate and Ag(111), vacuum sublimated α -sexithiophene grows by Frank-van der Merwe mode up to two layers and then transforms to Stranski–Krastanov mode upon further addition of molecular flux [161, 162]. Similarly, p-sexiphenyl films deposited in-vacuo are known to grow by both Stranski–Krastanov and Volmer–Weber on single crystal substrates such as KCL and mica [163]. These molecules are used in chapter 5 of this thesis. The dynamic interplay among these molecular processes and growth modes illustrates the complexity of thin film deposition via thermal evaporation. Understanding these fundamental mechanisms is crucial for achieving precise control over film morphology and properties.

3.1.2 High Vacuum Electrospray Deposition of Conjugated Polymers

The process of *high vacuum* (HV) *electrospray deposition* (ESD) caters to deposit films in ultra clean environment from gas phase molecular ions which can provide the possibility of essentially solvent free deposition. At the heart of ESD is a process called *electrospray ionization* that has been long used as an ion source for mass spectrometers. There are three main stages in ESD for the generation of molecular gas phase ions by ESD: (i) the formation of Taylor’s cone, (ii) jet formation, and (iii) the generation of gas phase ions.

The schematic of HV-ESD process is shown in figure 3.2.

3.1.2.1 Taylor's cone formation.

Due to a high positive voltage (between 1–5 kV) applied to the emitter, an *electric field* (E) comes into play. The magnitude of this 'E' is maximum near the sharp emitter tip which results in polarization of solvent molecules near the tip. In the solution, the solute separates into positive and negative ions, assuming the solute is ionic in nature. These positive ions will move under the influence of applied positive biasing, towards the surface of the liquid i.e. towards emitter tip and the negative ions will move in the opposite direction. This process continues until there is a charge redistribution such that ions are free of any influence of E . As a consequence of accumulation of excess positive charges at the emitter tip, the liquid meniscus gets unstable and takes the form of a cone [164, 165]. This cone is termed *Taylor's cone* named after the British physicist and mathematician [166]. At this point there are two competing forces acting on the conical liquid meniscus— surface tension and electrostatic forces. Surface tension acts to pull the liquid back into the emitter as it tries to resist the increase in surface area of the liquid meniscus due to the formation of Taylor's cone. While electrostatic force acts to pull the charged liquid at the meniscus towards the counter electrode (inlet capillary).

3.1.2.2 Jet formation.

At a certain critical voltage called *Rayleigh's limit*, the electrostatic forces overcome surface tension and a fine charged jet is expelled from the emitter. This jet further breaks down into charged droplets as a result to electrostatic repulsions between the jet.

3.1.2.3 Formation of gas phase ions.

The expelled charged droplets can be considered as the cluster of polarized solvent and solute ions. These droplets further shrink in size as the neutral solvent evaporates. At a certain radius, decreasing droplet size (due to solvent evaporation) will bring about sufficiently high charge density to render the droplet unstable. Hence the droplet will break further into smaller droplets. This Coulombic fission of droplets into even smaller ones will continue until gas phase molecular ions are generated [165]

In HV-ESD, these gas phase molecular ions then enter the UHV chamber through the inlet capillary (see figure 3.2). The ESD unit attached to high vacuum chamber is differentially pumped so as to bridge the pressure from ambient conditions to high vacuum. The two roughing pumps at stage I and II generate vacuum of up to the order of 10^1 mbar and 10^{-2} mbar. While the turbo pump at stage III creates vacuum of the order of 10^{-5} mbar. These three stages of vacuum makes it feasible to get rid of all the neutral solvent molecules, if any, that enter the vacuum chamber. Finally, gas phase molecular ions arrives at the (conducting) substrate placed in HV chamber. These gas phase ions are neutralized as soon as they arrive at the substrate and the ion current is sensed by our in-house custom built current sensor.

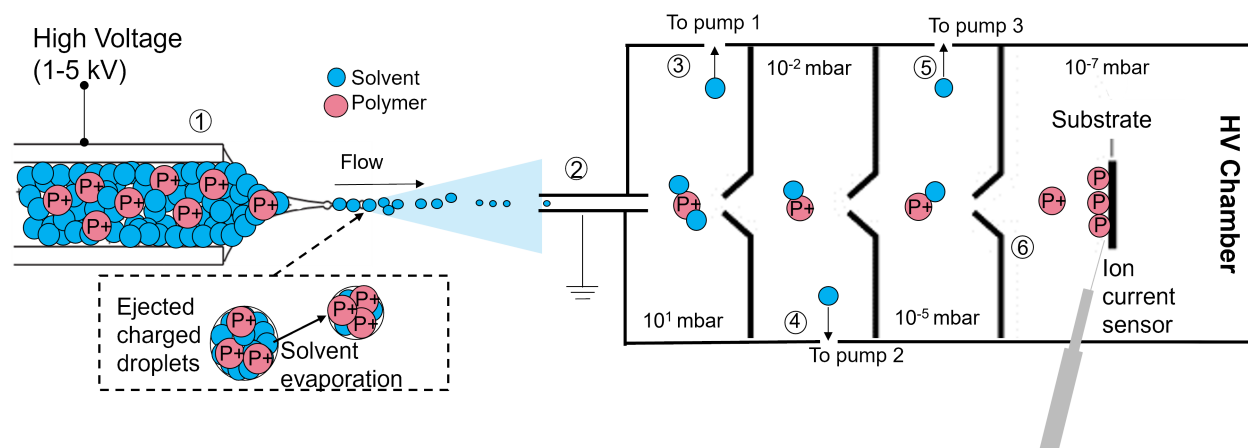


Figure 3.2: Illustration of high vacuum electro spray deposition technique. The parts are labeled by numbers and are named as- (1) metallic emitter capillary, (2) inlet or entrance capillary, (3) roughing pump at stage I, (4) roughing pump at stage II, (5) turbo pump at stage III, (6) high vacuum (HV) chamber.

3.2 Experimental Methods

This section explains the fundamental physics and the working principle of the characterization techniques used in this thesis. In this section, the basic experimental setup and the data analysis method is also introduced. The details about specific instrument parameters that are not general to the experimental methods itself can be found in the respective studies presented in this thesis.

First and foremost, X-ray diffraction (XRD; section 3.2.1) technique is introduced, that has been used as a vital structural characterization tool in my research work. Then, spectroscopic methods used in this thesis, such as, optical absorption spectroscopy (UV-vis/NIR; section 3.2.2), Fourier transform infrared spectroscopy (FTIR; section 3.2.4) and photoluminescence spectroscopy (PL; section 3.2.3) are presented, respectively. In the end, atomic force microscopy (AFM; section 3.2.5) is explained.

3.2.1 X-Ray Diffraction (XRD)

XRD is employed in this thesis for investigating the structural properties of crystalline blends of organic molecules in chapter 5 and amorphous thin films of polymer in chapter 4. This section on XRD is based on the references [167–170].

3.2.1.1 Basic theory

The interaction of X-rays with a material, in the absence of photoionization, i.e., the liberation of electrons from material, can be described by *inelastic* (Compton) scattering or *elastic* (Thompson) scattering. For structural investigation, the most commonly used formalism to describe XRD (referred to as kinematic theory disregarding absorption and multiple scattering) takes advantage of Thompson scattering where the energy of incom-

ing rays is conserved. In the following, only this very formalism is described and exclusively employed in the thesis.

When a beam of X-rays, described by a plane wave, $E_0 \exp(-iK_0.R_0)$, interacts with the crystal lattice, the electron density distribution of the atoms oscillates under the effect of electric field vector E_0 , leading to spherical waves emitted from all the atoms in all directions. Since this interaction between the crystal lattice and X-rays is *elastic* in nature, therefore the emitted waves will have the same wavelength, λ as the incoming X-rays. Now, these scattered waves can interfere constructively or destructively. But only when a *constructive* interference happens, they produce a diffraction pattern that contains information about the arrangement of atoms within the material.

The interaction of an incident X-ray beam with a crystal lattice can also be described using wavevectors, as shown in figure 3.3. The incoming and outgoing wavevectors of the incident X-ray, \vec{k}_i and \vec{k}_f , respectively, both with magnitude $2\pi/\lambda$, define the scattering plane and the scattering angle 2θ . The scattering vector, \vec{q} , is defined as the difference between the scattered and incident wavevectors:

$$\vec{q} = \vec{k}_f - \vec{k}_i \quad (3.1)$$

The magnitude of the scattering vector \vec{q} is related to the scattering angle (2θ) and the X-ray wavelength (λ) as:

$$|\vec{q}| = \frac{4\pi}{\lambda} \sin \theta \quad (3.2)$$

Considering equations 3.1 and 3.2 along with the geometrical consideration that $\sin \theta = m \frac{|\vec{q}|/2}{|k_i|}$, where m is an integer, we get the mathematical form of **Bragg's Law**.

$$n\lambda = 2d \sin \theta \quad (3.3)$$

where d is spacing between the lattice planes and n being an integer. This equation 3.3 highlights that constructive interference, and hence a diffraction peak observed in an XRD experiment, occurs only at specific angles where the path difference between waves scattered from adjacent planes is an integer multiple of the wavelength. The position of these peaks is determined by the spacing (d) between the atomic planes, as described by the equation 3.3.

The arrangements of atoms and the periodicity of the lattice can be best expressed by using the concept of reciprocal lattice which is a mathematical construct related to the real-space crystal lattice. Each point in the reciprocal lattice corresponds to a set of planes in the real-space lattice. The condition for diffraction or *Bragg's law* can then be expressed as simply as:

$$\vec{q} = \vec{G} \quad (3.4)$$

This formulation (equation 3.4), is known as the *Laue condition* and highlights that constructive interference occurs when the scattering vector \vec{q} coincides with a reciprocal lattice point \vec{G} .

Now if we consider a lattice with a unit cell defined by vectors $\vec{a}_1, \vec{a}_2, \vec{a}_3$, then the position of a lattice plane ' (hkl) ' can be described by the Miller indices h, k, l as- $\vec{a}_1/h, \vec{a}_2/k, \vec{a}_3/l$

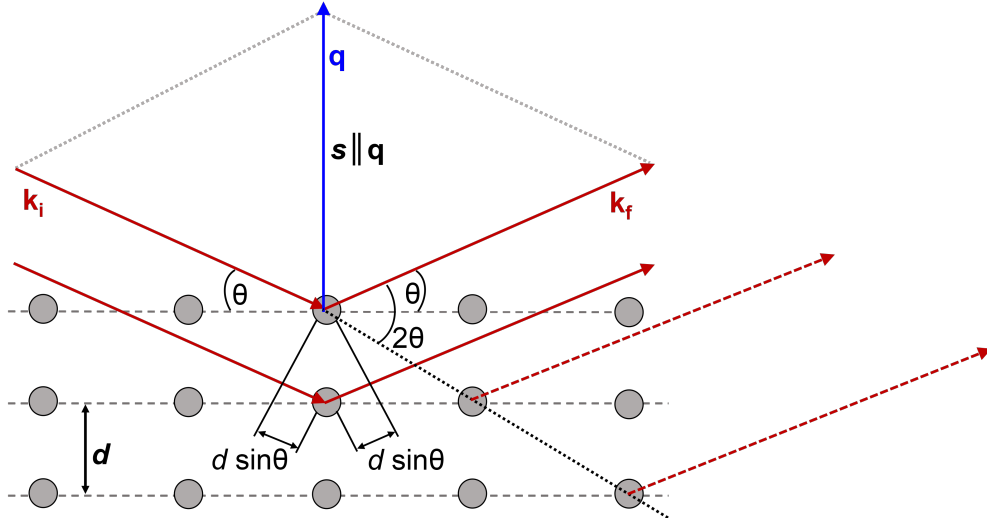


Figure 3.3: Representation of X-ray diffraction from crystalline lattice planes, showing the incoming (\vec{k}_i) and outgoing (\vec{k}_f) wavevectors, the Bragg angle (θ), the lattice-plane spacing (d), and the scattering vector (\vec{q}).

In crystallographic terms, in the real-space, a set of parallel lattice planes ‘ (hkl) ’ can be uniquely defined by their orientation and their periodicity where the orientation of the lattice planes is given by the normal to the planes and their periodicity is represented by the spacing ‘ d_{hkl} ’ between the planes. However, in reciprocal space, these planes are described by a single point. This point, denoted by the reciprocal lattice vector \vec{G}_{hkl} , carries all the essential information about the planes: their orientation, captured by the vector’s direction, and their periodicity, reflected in the vector’s magnitude.

Specular X-ray diffraction (θ - 2θ scan)

In a typical specular XRD or so-called θ - 2θ setup, a monochromatic X-ray beam is directed onto the sample at a varying angle θ and an X-ray detector is moved at the same angle (in a circle) to record the scattered X-rays [see 3.3]. Practically, using a source fixed in space, by rotating the sample at *half* the angular speed of the detector, a coupled configuration is maintained, ensuring that the incoming \vec{k}_i and the outgoing \vec{k}_f wavevectors are always symmetrically positioned with respect to the same set of lattice planes (hkl). Consequently, the scattering vector \vec{q} maintains a constant orientation relative to these lattice planes while its length is varied as a function of θ . The diffraction data in this thesis is presented in two-dimensions by resolving \vec{q} into two orthogonal components, namely, the *out-of-plane* component q_z (parallel to the surface normal \vec{s}) and in-plane component $q_{||}$. They are mathematically related as follow:

$$|\vec{q}| = \sqrt{q_{||}^2 + q_z^2}$$

In specular geometry q_z is constrained to be parallel to \vec{s} , meaning $q_{\parallel} = 0$. As a result, diffraction peak is observed *only* when q_z coincides with a reciprocal lattice vector \vec{G} , as dictated by equation 3.2. This implies that specular XRD selectively probes only those lattice planes that are oriented parallel to the sample surface, providing information about the *out-of-plane* periodicity. In this thesis, as detailed in chapter 5, specular XRD was employed to deduce the information on lattice plane spacing (d) and the out-of-plane periodicity in mixed polycrystalline film of α -sexithiophene and para-sexiphenyl.

Conventionally, diffraction data from θ - 2θ is plotted as intensity against 2θ angle (total scattering angle). However, representing the data in terms of q_z , using equation 3.2 facilitates to make the data independent of the X-ray wavelength thus allowing for direct comparison of diffraction data obtained with different X-ray wavelengths.

Grazing incidence X-ray diffraction (GIXRD)

In GIXRD, the primary beam interacts with a typically (ultra-)thin films (thicknesses ~ 1 – 100 nm) at a very small incidence angle (α_i). The angle α_i is chosen to be around or below the *critical angle* of the substrate. This is done to significantly reduce, the otherwise, inherently large X-ray penetration depth (l) of ~ 10 – 100 μm , as dictated by the relationship:

$$l = \frac{t}{\sin \alpha}$$

where t is the film thickness. GIXRD is, therefore, a highly surface sensitive experimental technique that minimized scattering from the underlying substrate that may otherwise mask the weak scattering intensity from a (ultra-)thin substrate. It allows recording high-quality data down to monolayer thin films [171]. Due to the small incidence angle (α_i) used in GIXRD experiments, the X-ray beam spreads over a larger sample area which effectively reduces the X-ray flux received per sample area. This is particularly important for beam-sensitive materials, like polymers, where prolonged exposure to X-rays can cause structural degradation. Figure 3.4 illustrates the grazing incidence geometry relative to the sample plane.

Unlike specular XRD, where the length of \vec{q} is varied perpendicular to the surface, GIXRD allows to alter the direction of \vec{q} in-plane. Thus GIXRD is a powerful technique for investigating the in-plane structural details (at $q_{xy} \neq 0$)* of thin films. GIXRD is used as a technique complementary to specular XRD, to gain insights into the overall structure of, for example, a thin film. This has been exemplified in chapter 5 where GIXRD data revealed vertical elongated rods in q_{xy} direction, with no peaks in the out-of-plane (q_z) direction. Such rods are indicative of the characteristic herringbone arrangement of organic molecules and are observed in films of *monolayer* thickness. However, the specular XRD data showed sharp well-defined peaks in the out-of-plane direction, thus allowing to deduce the out-of-plane coherence length, which was ~ 158 Å along q_z . Hence, together from GIXRD and specular XRD data, it was concluded that the investigated film has a layered structure with *in-plane* crystalline order but lacks *out-of-plane* periodicity, implying the random stacking of the layers.

*In GIXRD terminology, q_{\parallel} component of the scattering vector is usually referred to as q_{xy}

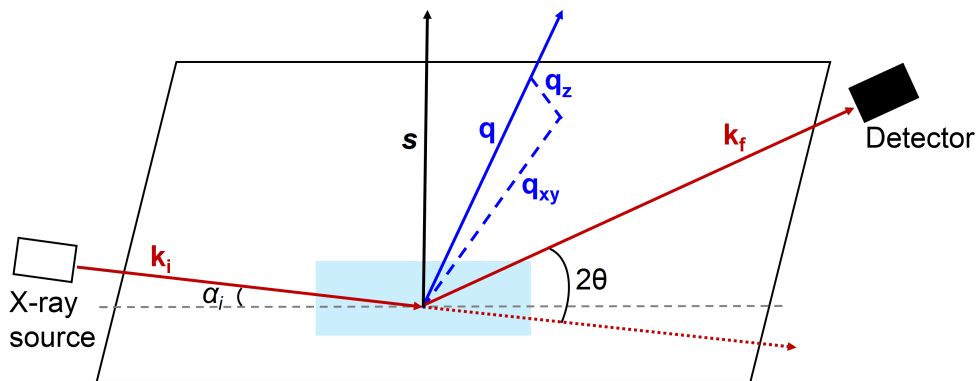


Figure 3.4: Illustration of grazing-incidence X-ray diffraction (GIXRD) geometry, showing the incoming (\vec{k}_i) and outgoing (\vec{k}_f) wavevectors beams, Bragg angle (θ), grazing incidence angle α_i and components of scattering vector (\vec{q}), parallel (q_z) and perpendicular q_{xy} to film surface.

3.2.1.2 Experimental setup

The XRD data presented in chapter 5 was recorded by Dr. Roland Resel (*Graz University, Austria*) and Dr. Ingo Salzmann (then Humboldt University Berlin, Germany) on the W1 beamline at the synchrotron radiation facility DORIS (HASYLAB, Hamburg). Preliminary GIXRD data was collected there with a primary beam of energy of 10.5 keV at an incidence angle of 0.15° angle, using a goniometer (by Risø) in pseudo 2 + 2 geometry and a one-dimensional detector (MYTHEN, Dectris). A 2 + 2 geometry refers to the configuration of the diffractometer that provides four degrees of freedom for controlling the sample and detector positions. GIXRD dataset was recorded immediately after specular XRD and without altering the sample alignment. The use of a primary and secondary slit system (evacuated flight tube with entrance and exit slits behind the sample) allowed for recording high resolution data required for the precise determination of peak positions. The GIXRD dataset presented in chapter 5 was collected by myself at the Canadian Light Source (CLS), Saskatoon, SK, Canada, at the Brockhouse Low Energy Wiggler beamline, with a primary beam of wavelength 0.82 \AA (15 keV) at incidence angles between 0° and 0.12° , using Rayonix MX300 detector.

3.2.1.3 Data acquisition and treatment

The experimental diffraction data, presented in chapter 5, was transformed to reciprocal space using the custom-made software PyGID [172]. The peaks in specular XRD data, reported in chapter 5, were fitted using Voigt functions. An open source software GIDVis [173], GPL v3.0, was used for transforming the raw GIXRD data, reported in chapter 4, into 2D reciprocal space maps. To reduce signals from air scattering and to protect samples from beam damage, GIXRD data was recorded under inert He environment.

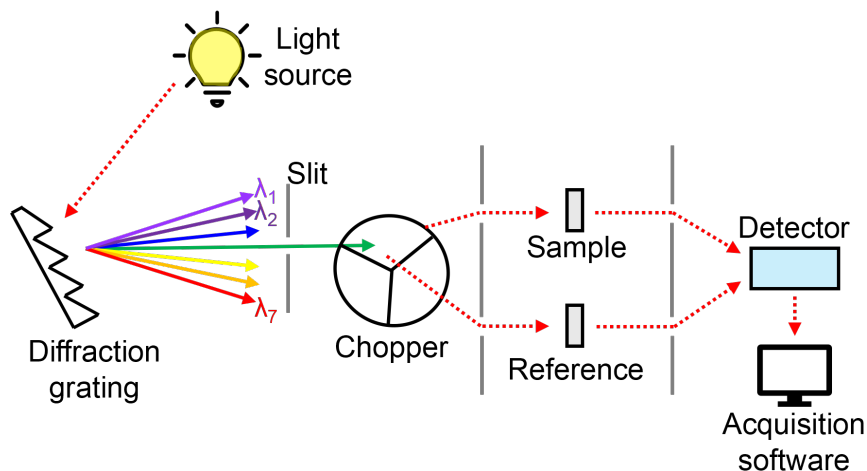


Figure 3.5: A simplified illustration showcasing the key components of a dual-beam UV-vis/NIR spectrometer, comprising a *light source*, a *diffraction grating* to split the light from the lamp into its constituent wavelengths, *slit* for controlling the wavelength resolution, a *chopper mirror* that alternatively directs the incident wavelength towards the sample and reference beam path, a *detector* for recording the light intensity that passes through *reference* and *sample* and a computer with *acquisition software* to generate corresponding absorption spectrum.

3.2.2 Optical Absorption Spectroscopy (UV-vis/NIR)

Optical absorption spectroscopy is a versatile analytical technique that leverages the unique electronic transitions inherent to molecular structures to provide insights into a sample's composition. By analyzing the distinct wavelength absorbed by or transmitted by a sample, we can identify the constituent molecules. Absorption spectroscopy uses wavelengths in the ultraviolet (*UV*)- visible (*vis*)/ near-infrared (*NIR*) region of the electromagnetic spectrum, where the *UV* region extends from $\sim 200\text{--}400\text{ nm}$, the *vis* region from $400\text{--}700\text{ nm}$, and the *NIR* region from $700\text{--}2500\text{ nm}$ [124, 174].

3.2.2.1 Basic theory

When electromagnetic radiation from UV-vis/NIR region is incident upon a sample, certain energies are absorbed by the constituent molecules, causing an attenuation of incident light intensity. This attenuation is governed by *Beer-Lambert law*:

$$A = \log_{10}\left(\frac{I_0}{I}\right) = -\log_{10}(T) \quad (3.5)$$

where A is the *absorbance* which is given by negative logarithm of transmittance T . i.e. the ratio of I_0 is the intensity of the incident beam while I is the transmitted intensity, I_0 is the intensity of the incident beam while I is the transmitted intensity. [124, 174]

The absorbed energies excites electrons from the HOMO to the LUMO. Given that energy is quantized ($E = nh\nu$), the energies absorbed by the sample, correspond to the

energy difference between its HOMO and LUMO levels. This HOMO to LUMO transition represents the *optical band gap* of the material and is experimentally determined by the onset of absorption edge of the optical absorption spectra [1]. Theoretically the electronic transitions would appear as sharp line; however, in practice, they often appear as broad absorption bands due to spectral broadening. This broadening arises from the coupling of vibrational transitions to each electronic state, resulting in multiple spectral features [124, 174]. However, *selection rules*, governed by the symmetry relationship between the involved orbitals, dictate which transitions are allowed. For instance, an electronic transition would be *forbidden* if the spin quantum number of an electron, undergoing the transition, would change [1]. Nevertheless, in experiments, the forbidden transition can result in weak absorption bands. One such case is presented in the figure 5.4 of chapter 5 where the absorption spectra of *in-vacuo* deposited α -sexithiophene films exhibit absorption bands arising from transitions that, while initially *forbidden*, become *partially* allowed due to symmetry breaking. This symmetry breaking is attributed to increased structural disorder which in turn is known to be dependent on film thickness [175].

3.2.2.2 Experimental setup

Absorption data presented in this thesis was acquired using a Varian Cary 5000 spectrometer with an average time of 0.033 s and 1 nm data interval. Generally, a UV-vis/NIR spectrometer has a deuterium lamp to generate wavelength in the UV region and a tungsten-halogen lamp for the vis & NIR regions, a monochromator (i.e. a diffraction grating), a sample compartment and detector. To cover the broad spectral range, Cary 5000 spectrophotometer utilizes two diffraction gratings and two detectors: a photomultiplier tube for the UV-vis region and a *lead sulfide* photocell detector for the NIR region. This dual-detector and dual-grating configuration enables simultaneous measurement of both UV-vis and NIR spectra. All absorption spectra were obtained by using the spectrometer in double-beam setup. In such a setup, as illustrated in figure 3.5, the incident light is split into two beams, directing one beam through the sample and the other through a reference. This allows simultaneous measurement and correction for artifacts arising from fluctuations in source lamp brightness, detector noise or other environmental factors such as stray light and contributions from substrate and sample holder (for thin films), solvent and cuvettes (for solutions).

3.2.2.3 Data acquisition and treatment

Solution absorption measurements were conducted by first recording a baseline spectrum using a quartz cuvette of 0.2 mm effective path length, containing the 'pure solvent' and measuring it as a sample, against a *blank* cuvette placed in the path of reference beam (see figure 3.5). Later, the cuvette with pure solvent was replaced by, for instance, with poly(3-hexylthiophene-2,5-diyl) solution to obtain 'sample spectrum' (measured against blank cuvette in the reference beam path). The *sample spectrum* is automatically corrected for baseline absorbance during acquisition by the software, using a previously recorded baseline spectrum. However, the procedure to obtain absorption spectra of solid-state samples i.e., thin films deposited on quartz substrates, was a bit different. The thin film

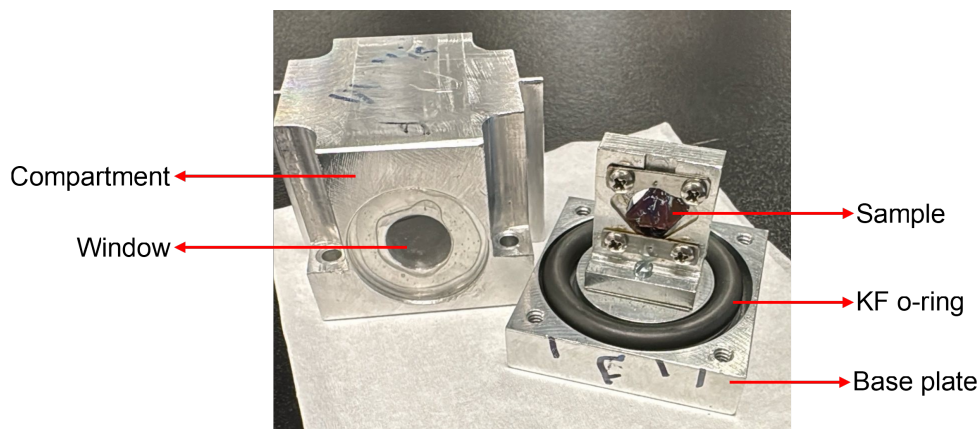


Figure 3.6: Inert atmosphere sample holder used for measuring optical absorption spectroscopy spectrum of thin film samples. The compartment is sealed onto the base plate using the KF o-ring. For UV-vis/NIR spectroscopy measurements, an inert sample holder with quartz windows is used.

samples were analyzed using an inert-atmosphere sample holder, like the one shown in figure 3.6. The holder was designed by another Ph.D. student in our lab, further details of the design could be found in ref. [13]. Due to the availability of only one sample holder, the reference beam path was left empty while measuring the ‘baseline’ and ‘sample’ spectrum. Control experiments, in which a clean quartz substrate was measured as a sample, after baseline correction, confirmed that this single-sample holder approach did not introduce any significant artifacts in the ‘sample spectrum’.

3.2.3 Photoluminescence Spectroscopy (PL)

PL spectroscopy uses the phenomenon of *spontaneous emission*, to probe the electronic structure and excited-state dynamics of a material. Analysis of PL spectra aids identifying the presence of defect states within the band gap of a material (which often appears as lower-energy emissions), and understanding energy transfer mechanisms between varying constituting materials. This section is based on references [125, 127, 176].

3.2.3.1 Basic theory

When a material is exposed to an electromagnetic radiation source, it undergoes *photoexcitation* i.e., photons are absorbed, if the energy E_a of the photons ($E_a = h\nu$, where h is Planck’s constant and ν is the photon frequency) match the electronic band gap of the material. The absorption process excites an electrons from *ground state* (S_0) to *higher energy levels* (S_n). The excited electron is often in a higher vibrational level (ν_n) of S_n electronic state and quickly loses this excess vibrational energy through *non-radiative* processes such as collision or vibrational interactions (*phonons*) within the material lattice before relaxing to the lowest vibrational level (ν_0) of S_n . Further, the excited electron transition back to S_0 , from S_n , through a *radiative* process that involves emitting a photon. The above mentioned processes are illustrated in figure 3.7.

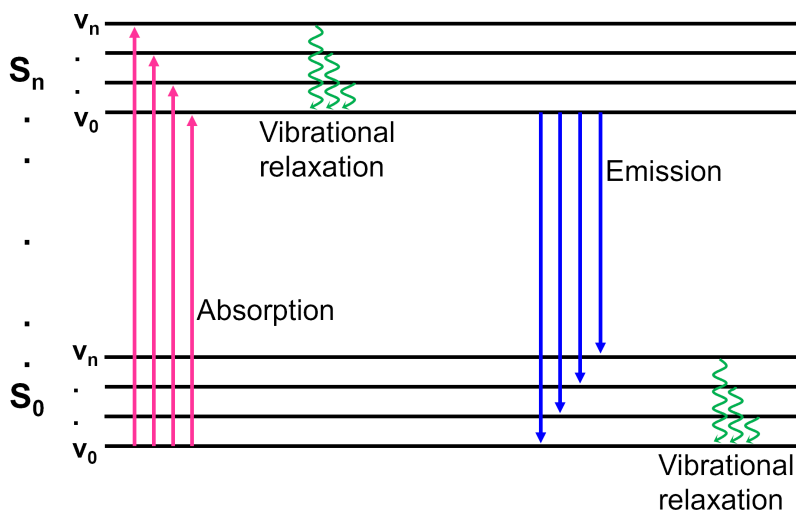


Figure 3.7: Jablonski diagram for photoluminescence, highlighting the pathways of absorption, vibrational relaxation, and fluorescence emission. Diagram shows ground state (S_0) and n^{th} excited state (S_n) energy levels of a molecule along with their vibrational levels from ν_0 to ν_n .

The emitted photon carries energy that matches the energy difference (ΔE) between S_n and S_0 . Here ΔE is most often *less* than E_a , as an outcome of energy loss during *vibrational relaxation*. If PL spectrum of a material is *red-shifted* relative to its absorption spectrum, the spectral shift is referred to as *Stoke's shift*.[†] It is because of Stoke's shift that it is possible to acquire PL spectrum of a material, by enabling the separation between emitted and excitation energies.

The PL (emission) spectra presented in chapter 5 were obtained with Horiba PTI QuantaMaster 8075 spectrofluorometer. To acquire these solid state emission spectra, a slide holder accessory was used which positions the samples at 120° angle from the incident light. The measurements were done with 1 nm step size, an integration time of 1 s per step, slits (excitation and emission) set to 5 nm and an automatic 5 sec dark background collection.

Horiba QuantaMaster utilizes a 75 W Xenon arc lamp, which serves as a broad excitation source spanning the ultraviolet, visible, and near-infrared spectral regions of the electromagnetic radiation. An excitation monochromator enables the selection of individual excitation wavelengths[‡] (λ_{exc}) to target specific electronic transitions within the sample. Upon excitation, the excited electrons relax to their ground state by emitting light photons with characteristic energies. An emission monochromator, that is positioned orthogonally relative to the excitation path, allows separating the emitted wavelength along with effectively minimizing interference from scattered excitation light.

[†]IUPAC defines it as the energy difference between the 0–0 transitions in absorption (S_0, ν_0 to $S_{n=1}, \nu_0$) and PL ($S_{n=1}, \nu_0$ to S_0, ν_0) spectra. But sometimes in practice, Stoke's shift is taken as the difference between absorption and PL peak maxima.

[‡]While wavelength is conventionally used in PL spectroscopy, energy scales makes more sense when discussing electronic transitions.

Photomultiplier tube detector counts each photon reaching it and convert the photon count to a measurable electrical signal. The signal is subsequently amplified and processed to generate the PL emission spectrum of the sample.

3.2.3.2 Data acquisition and treatment

To avoid interference from second-order diffraction of the excitation wavelength (λ_{exc}), a long-pass filter was incorporated into the excitation beam path. For instance, as shown in figure 5.5, when $\lambda_{exc} = 325\text{ nm}$ is used to record the emission spectrum of mixed '6T+6P' film, there a second-order diffraction of λ_{exc} could lead to a spurious signal at double the λ_{exc} (650 nm) which is also the 'region of interest' in this case. Here, using a long-pass filter with a sharp cut on the wavelengths above 350 nm would reject any undesirable wavelengths from the excitation beam and thus any potential signal at 650 nm (due to second-order diffraction from the detector), ensuring that the resulting emission spectrum originates solely from the material.

The PL emission spectra recorded by Horiba spectrofluorometer were further corrected for any contributions from the substrates or from the instrument optics, monochromator and detector. The acquisition software automatically acquires a 5 sec 'dark' (i.e., without any light source) background on the samples before each measurement. Applying this correction to the raw emission data, either in real-time or during subsequent analysis, yields the 'corrected' emission spectrum. This 'corrected' spectra were used in this thesis.

3.2.4 Fourier-Transform Infrared Spectroscopy (FTIR)

In contrast to UV-vis/NIR absorption spectroscopy, which inspects electronic transitions in molecules, FTIR spectroscopy investigates the vibrational modes of molecules. Specifically, those vibrations that induces change in the molecular dipole moment, known as 'infrared-active' vibrations, are detected by FTIR spectroscopy.

3.2.4.1 Basic theory

In FTIR, the sample is irradiated with all the wavelengths, from an infrared (IR) source at once, in contrast to UV-vis/NIR spectroscopy. The constituent molecules in the sample absorbs photons with energies that matches their vibrational modes, causing transitions between vibrational energy levels. At the core of a FTIR spectrometer lies *Michelson interferometer* (see figure 3.8). The basic optical setup of an interferometer consists of a beamsplitter **B** held at 45° angle w.r.t. the incident IR beam, a fixed mirror **M** and a moving mirror **M'**. The incident IR light beam is split into two beams by **B**, out of which one half of the beam is reflected towards **M** held at while the other half is transmitted towards **M'**. Both **M** and **M'** are at 90° angle to the respective halves of the incident IR beam. The two beams are then reflected from **M** and **M'** and returned to **B** where they reunite to form a single beam. Due to the motion of **M'**, the second half of the beam returning to **B** will now have a different path length than the first half. Therefore, after returning at **B**, the two beams reunite through *constructive* or *destructive* interference depending on

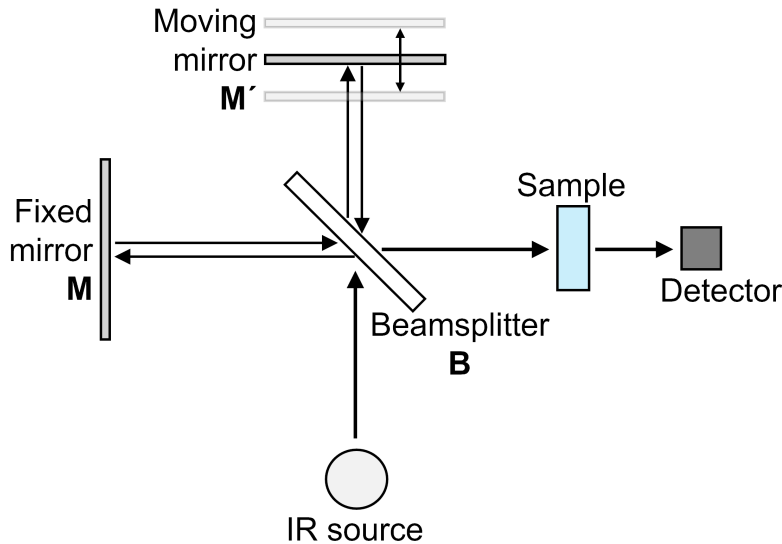


Figure 3.8: Conceptual outline of a transmission-mode FTIR spectrometer employing an IR source, a detector, a sample and a Michelson interferometer. The beamsplitter (B), fixed mirror (M), and moving mirror (M') are the components of a Michelson interferometer.

the position of M' (thus the path difference), split again and then partially reflected and transmitted towards the source and the detector [177].

The distribution of light intensity between these two arms of the interferometer relies on the phase difference resulting from the path difference between the two beams. When the separation between M and B is similar to that between M' and B i.e., if the path difference x between the beams coming from M and M' is *zero* or an *integral* multiple of wavelength λ then a constructively interfered beam is directed from B towards the detector, meaning the maximum beam intensity reaches the detector [177].

However, if M' deviates from the equidistant position such that beams *to* and *from* the B has a path difference $x = \lambda/2$, then the beams will be *out of phase* w.r.t one another at B and will interfere destructively. At this point, zero to minimum beam intensity will reach the detector and the maximum returns to the source [177]. The intensity recorded at the detector as a function of mirror position is called an *interferogram*, which is basically a plot of intensity versus time. An *interferogram* contains information about all the IR wavelengths (or frequencies) emitted by the source. Assuming a monochromatic IR source emitting at frequency ν , the interferogram ($I(x)$) can be described as:

$$I(x) = 2RTI(\nu)(1 + \cos(2\pi\nu x)) \quad (3.6)$$

where R and T are the reflectance and transmittance of the beamsplitter, respectively, x is the path difference and $I(\nu)$ is the intensity of the source beam. The nodes of the \cos function in equation 3.6 acts a ruler that can be used to accurately identify the zero path difference position for an IR source including a range of frequencies [177]. In FTIR spectroscopy, sample is exposed to a range of frequencies using a polychromatic IR source. Therefore the resulting interferogram of a sample, in the *time-domain*, is a complex su-

perposition of all the interference patterns originating from the individual frequencies. To extract the meaningful information about the frequencies absorbed by the sample, the *time-domain* signal is converted into *frequency-domain* by using *Fourier transform* (FT). Now, the interferogram for a polychromatic IR source in the time-domain is described as:

$$I(x) = \int_0^{\infty} A(\nu)(1 + \cos(2\pi\nu x))d\nu \quad (3.7)$$

where $A(\nu)$ is the intensity of the polychromatic IR source, also termed as *spectral distribution* of the polychromatic source [177]. Now, for zero and large path differences, the interferogram $I(x)$ in equation 3.7 approaches a maximum intensity ($I(0) = \int_0^{\infty} A(\nu)d\nu$) and a constant intensity value ($I(\infty) = I(0)/2$) respectively. Thus the interferogram can be written as:

$$F(x) = I(x) - I(\infty) = \int_0^{\infty} A(\nu)\cos(2\pi\nu x)d\nu \quad (3.8)$$

The FT of equation 3.9 returns the spectral distribution of the polychromatic source:

$$A(\nu) = 2 \int_0^{\infty} F(x)\cos(2\pi\nu x)dx \quad (3.9)$$

The final expression i.e., equation 3.8 gives the information about the frequencies absorbed by the sample. To extract the FTIR spectrum of just the sample, a ‘reference’ scan on a blank substrate is performed which is then compared with ‘sample’ scan [177].

When used in transmission mode, like in chapter 5 chapter, where the film samples are placed perpendicular relative to the beam path, FTIR spectroscopy falls short for investigating (ultra-)thin films, monolayers and interfaces on reflective substrates. This is where *Grazing Incidence* (GI) FTIR spectroscopy offers higher sensitivity for aforementioned studies [178]. The grazing incidence angle ($\sim 6.3^\circ$ degrees in chapter 4) in GI-FTIR significantly increases the effective penetration depth of the IR beam through the (ultra-)thin films, resulting in enhanced absorption signals. Since GI reflection FTIR has only been employed in chapter 4 to qualitatively verify the amount of poly(3-hexylthiophene-2,5-diyl) content on SiO_x substrates, therefore this technique is only briefly discussed at this point.

3.2.4.2 Experimental setup

The FTIR data in chapter 5 was collected using Thermo Scientific Nicolet 6700 FTIR spectrometer that uses an EverGlo glowbar IR source, a KBr beam splitter, and a MCT-A liquid nitrogen-cooled HgCdTe detector. FTIR in transmission mode was used to investigate the thin film deposited on SiO_x substrates and the samples were held inside a sample holder that was sealed inside the glovebox. The sample holder used for transmission studies was similar to the one used in section 3.2.2, figure 3.6 except the windows on the holder were made of KBr instead of quartz. Prior to any measurements, the spectrometer was allowed to purge three times using a purge-gas generator. This entire procedure was used to minimize the intensity of CO_2 and H_2O peaks in the spectra and to record any baseline or sample spectrum under inert atmosphere.

FTIR measurements in chapter 4 were performed in grazing incidence reflection geometry (GI-FTIR) using a Bruker Vertex 70v equipped with liquid nitrogen-cooled MCT detector to enable performing FTIR on conductive substrates, as required by ESD. The GI-FTIR spectra was recorded under vacuum $\sim p < 10^{-1}$ mbar. In this setup, the grazing incident angle of the IR beam was fixed to be 6.3° with respect to the sample surface (specular reflection) and care was taken to maintain a consistent beam footprint across all samples.

FTIR dataset in above mentioned chapter were recorded with the resolution of the spectrometer set to 4 cm^{-1} .

3.2.4.3 Data acquisition and treatment

The FTIR spectra presented in figure 5.3 was normalized to the maximum intensity of the peak around $\sim 792\text{ cm}^{-1}$ for the α -sexithiophene (6T) film and $\sim 760\text{ cm}^{-1}$ for both the p -sexiphenyl (6P) and mixed 6T+6P films. No further data processing was done on this spectra. FTIR spectra shown in figure 4.12 is presented without any normalization or data treatment.

3.2.5 Atomic Force Microscopy (AFM)

AFM detects and quantifies the forces between a sharp probe and a sample surface to provide high resolution imaging of surface morphology at nanometer scale. The magnitude and nature of these forces depend critically on the probe-sample distance, nature of sample and the type of probe. AFM not only maps surface topography (for example, through surface roughness analysis) but also provide information about material properties such as conductivity, adhesion, elasticity/stiffness and friction. The following section is based on the references [179–181].

3.2.5.1 Basic theory

AFM operates on the principle of measuring the interaction forces between a sharp probe, mounted on the free end of a flexible cantilever, and a sample. The nanoscale probe is often composed of Si or SiN. As the probe approaches the surface, it experiences a range of forces depending on the respective materials, including *van der Waals forces* and *electrostatic forces*. When the probe-to-surface distance is typically around $\geq 1\text{ nm}$, attractive *van der Waals* interactions, dominate. The attractive forces are a consequence of the temporary fluctuations in electron distribution within atoms of the tip and the sample, resulting in the formation of induced dipoles that attract each other. But when the probe and the sample surface are at sufficiently close distances of $\leq 0.1\text{ nm}$, the interaction enters a regime dominated by repulsive electrostatic forces stemming from overlapping electron clouds between the tip and sample atoms. While the attractive van der Waals forces theoretically exhibit a r^{-6} dependency and the repulsive forces a r^{-12} dependency on the probe-surface distance (r), the geometry of the probe modifies this interaction profile. Approximating the probe as a hemisphere with a radius of 10–50 nm interacting with an infinite sample plane leads to a more gradual decay of the effective van der Waals force,

following a r^{-1} dependency [180, 181]. This slower change makes it possible for AFM to detect the subtle differences in force as the probe scans the surface.

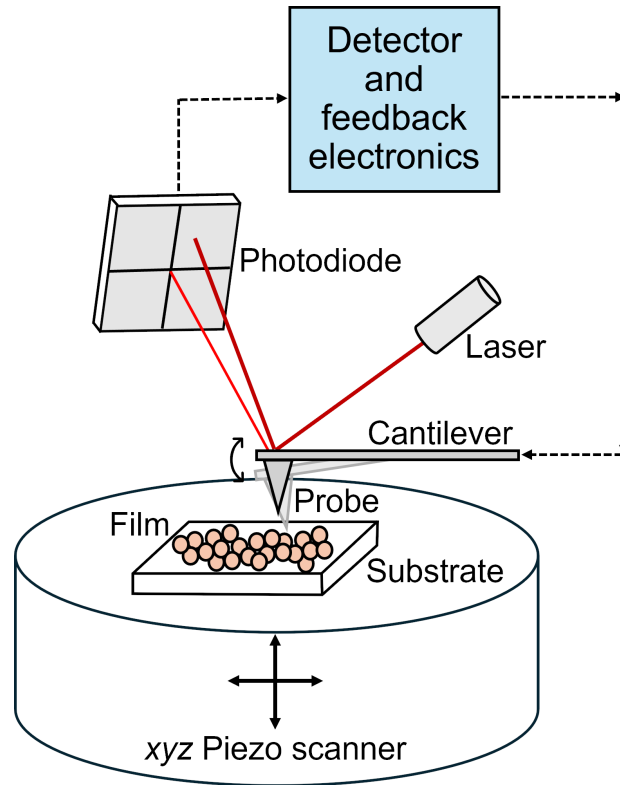


Figure 3.9: Schematic of an AFM; a sharp probe mounted on a cantilever, scans the surface of the thin film deposited on a substrate. A laser and a photodiode records cantilever deflections, resulting from probe–sample atomic interactions. A feedback loop monitors these movements and apply a constant force on the cantilever using piezo elements, to generate an image of sample’s topography.

The deflection or oscillation of the probe in response to probe-surface forces is recorded by using a laser beam focused at the back of the cantilever and reflected on to a position sensitive four-quadrant photodetector (PD). Any subtle changes in the deflection/ oscillation of the cantilever alters the position of the ‘reflected’ laser beam on the PD, which in turn converts these changes into an electrical output. A feedback loop between the PD and the cantilever, forwards this electrical signal to the piezoelectric transducers, which adjust the height of the probe (by moving the probe towards or away from the surface). Therefore this electrical signal is the used by the atomic force microscope to map the topography of a sample.

AFM can be operated in two primary modes, namely- *static mode* and *dynamic mode*. In *static mode*, as commonly know as *contact mode*, the probe is in *continuous* physical contact with the surface while scanning it laterally. The feedback loop adjusts the vertical position of the cantilever to maintain a constant cantilever deflection. This deflection is directly related to probe-surface interaction forces, thus allowing the AFM to map the surface topography. Contact mode can exert significant lateral forces on the sample

therefore it is well suited for imaging rigid samples as it can potentially damage delicate samples such as films of organic polymers and molecules.

Dynamic mode is further categorized into amplitude-modulation (AM) (or tapping) mode and frequency-modulation (FM) (or non-contact) mode.

In *tapping mode*, the cantilever intermittently ‘taps’ the sample surface while oscillating near its resonance frequency. As the probe approaches the surface, the probe-surface interaction forces dampen the oscillation amplitude. Here, the feedback loop maintains a constant oscillation amplitude by adjusting the probe-surface distance, such that the initial amplitude value set by the user is maintained. In *tapping-mode*, the sample surface experiences minimum lateral forces, hence making it ideal for imaging soft or delicate samples.

The *non-contact mode* monitors the shift in the resonant frequency of the cantilever and as opposed to *contact-mode*, this mode operates in the attractive regime of probe-surface interaction forces. When the cantilever, oscillating near its resonant frequency, approaches the surface its resonant frequency shifts as a consequence of (attractive) probe-surface interaction forces. The feedback loop monitors the shift in resonance frequency and in response, adjusts the probe-surface distance to maintain a constant frequency. This mode offers better sensitivity but at the cost of lower resolution, as compared to other two AFM modes. Since there is no direct contact between the probe and the surface in non-contact mode, therefore it is well-suited for imaging extremely delicate samples, as it minimizes the risk of damage.

3.2.5.2 Data acquisition and treatment

To study the morphology of the electrosprayed films in chapter 4, a Bruker MultiMode 8HR AFM in tapping mode was employed. AFM scans were done using ACTA aluminum-coated n-type silicon probes (AppNano) with force constant of 13-77 N. The acquired images were corrected and analyzed using NanoScope 9.7 software.

Chapter 4

Amorphous Poly(3-hexylthiophene) (P3HT) Thin Films by Vacuum Electropray Deposition

The content of this chapter has been published as:

S. Bhagat, M. Berteau-Rainville, S. Beram and I. Salzmann, “Amorphous Poly (3-hexylthiophene) (P3HT) Thin Films by Vacuum Electropray Deposition,” *Crystal Growth & Design*, vol. 24, Art. no. 15, 2024.

Abstract

Vacuum electropray deposition is a promising technique to deposit solvent-free films of polymers or (macro)molecules that can otherwise only be processed in solution owing to their thermal fragility. However, the different environments of vacuum and solvent during film growth can have severe effects on the resulting thin film morphology and structure. Here, we investigate the thin film growth of the generally semi-crystalline conjugated polymer poly(3-hexylthiophene) (P3HT) by vacuum electropray deposition and juxtapose it with films conventionally grown from solution. We find that, in contrast to the solution-processed films, those from electropray deposition appear to be entirely amorphous, which we deduce from amorphous scattering in synchrotron grazing-incidence X-ray diffraction, where their diffraction signature resembles that of dropcast films *in-situ* heated close to their melting point. While numerous experimental approaches exist to increase structural order in thin films, deliberately establishing amorphous films is a challenge for semi-crystalline materials. Based on our present example of P3HT, vacuum electropray deposition therefore emerges as a thin-film preparation technique that is very well suited to readily suppress crystallization, which can be of high value for disentangling experimental data obtained for semi-crystalline materials.

4.1 Introduction

During the past decades, applications based on conjugated organic molecules and conjugated polymers (CPs) which constitute the material class of *organic semiconductors* have attracted considerable interest as their optoelectronic properties are tunable over a large range by tailoring the chemical structure. [36] In addition to the commercial success of organic semiconductors in organic light-emitting diode (OLED) based display technology, [38–40] they are highly promising for thermoelectric, [182] photovoltaic, [45, 183] biomedical, [32] and transistor applications. [25, 47] To large extent, the profound interest in CPs originates in their potential for large-scale processability into thin films by employing cost-efficient solution-based techniques and the feasibility of using highly flexible substrates. [25, 26, 184]

The most commonly employed solution processing techniques for CPs include inkjet printing, [185] roll-to-roll printing, [186] dip-, [187] and spin-coating. [188] For all, the proper choice of solvent [65] together with numerous experimental parameters [61–64] such as the solvent evaporation rate, [69] the solubility of a given CP [66] or that of CP blends therein (e.g., for bulk heterojunction solar cells [67, 68]), as well as substrate properties [70] including temperature [71, 72] govern the achievable film properties. This can easily translate into hard-to-control and ill-defined microstructure and packing for (semi-) crystalline CPs. [73] In contrast, films of conjugated organic small molecules (COMs) often exhibit significantly better-defined structure and can form highly crystalline films, where processing is possible under (high/ultra-high) vacuum conditions via thermal sublimation and deposition on *in-vacuo* cleaned surfaces. There, specific substrate properties including the chemical composition at the substrate interface and its temperature [189, 190] together with stable and precisely adjustable deposition rates [56, 191] are comparably easy to establish and control. For CPs, however, this represents no feasible approach as CPs are thermally fragile due to their high molecular weight. Thermal sublimation induces chemical degradation such as the breaking of backbone bonds or the loss of alkyl-sidechains commonly substituted to the CP backbone to increase solubility. [60] Therefore, CPs are, in general, processed from solution.

To overcome this limitation and reconcile the material class of CPs with vacuum processing, electrospray deposition (ESD) under high vacuum (HV) conditions represents a promising technique that bears the potential of establishing highly defined CP layers largely without the influence of the solvent during thin-film growth. In HV-ESD, the CP films are deposited from the gas phase within a clean and well-controllable environment, essentially independent from contamination of surface and solvent, and onto substrates that can be cleaned *in vacuo*. As a result, HV-ESD represents a viable tool to achieve additional control over the CP microstructure and crystallinity in thin films, otherwise impossible with conventional solution processing techniques. [192, 193] In analogy to vacuum deposited COM films where elevated substrate temperatures can translate into improved order and microstructure, [194] CP films deposited *via* ESD onto substrates held at elevated temperatures (e.g., > 200°C)—intrinsically incompatible with most common solvents in conventional solution processing—can be expected to be beneficial for such films as well. [195, 196] Furthermore, ESD offers the ability to deposit polymers on atomically clean substrates such as metal single crystals and investigate adsorption

geometries using scanning tunneling microscopy with submolecular resolution. [197]

In a practical ESD experiment, high voltage is applied to the polymer solution which is guided through a metallic emitter. At a certain critical voltage (denoted as Rayleigh's limit) the liquid meniscus at the emitter exit aperture takes the form of a cone, typically referred to as *Taylor cone*. [166] Increasing the voltage beyond Rayleigh's limit results in a jet of charged liquid expelling from the emitter due to electrostatic forces taking over the surface tension of the liquid. [198] Coulomb repulsion breaks down the charged liquid jet into charged droplets, which then shrink in size due to solvent evaporation. [166, 198] In a practical setup, this happens during trajectory through a differentially pumped device with the goal to finally produce molecular ions in the gas phase. These charged molecules are then deposited on a substrate located in the HV chamber.

Prototypical CPs such as regioregular poly(3-hexylthiophene) (P3HT) are found to be semi-crystalline if grown from solution with the ratio of crystalline to amorphous film portion (often referred to as the film's "crystallinity") subtly depending on numerous experimental parameters and preparation strategies. [199, 200] In order to *increase* crystallinity, material factors and strategies have been identified and exploited including the CP molecular weight, [104] post-fabrication thermal annealing, [99] solvent-vapor annealing, [100] epitaxial growth on anisotropic substrates, [101] self-seeded growth, [102] or high-temperature rubbing (HTR). [103] The film crystallinity has immense impact on charge transport in pristine CP films [97, 201] and on charge transfer in heterostructures (e.g., as employed in organic photovoltaic devices) [202] as well as in doped CPs, where it has been argued that amorphous and crystalline film portions react differently to dopant exposure. [98] For example, for regioregular poly(3-hexylthiophene) (P3HT) a doubling in crystallinity was reported to be achievable by HTR [103] or by 50% via post-fabrication annealing, respectively. [99] In contrast, deliberately *reducing* crystallinity and achieving *amorphous* films of an intrinsically semi-crystalline CP is challenging upon crystallization from solution on surfaces. Achieving such films can, however, be of high scientific interest to disentangle data experimentally gained on semi-crystalline CPs where processes such as, e.g., charge transfer between the CP and molecular dopants, happen differently for the crystalline and amorphous regions, and experimental information gained from both regimes using non-locally resolved techniques become superimposed. [80, 98] In such situations, preparing *amorphous* CP films represents the most straightforward experimental approach.

Here, we demonstrate that room-temperature HV-ESD of P3HT enables establishing such amorphous films, as we infer from synchrotron grazing-incidence X-ray diffraction (GIXRD). We conclude that due to the absence of a solvent during surface nucleation and crystallization of the CP and its limited diffusion, HV-ESD can represent a generally viable technique to establish amorphous structures for otherwise crystalline systems.

4.2 Experimental Details

4.2.1 Materials

Regio-regular poly(3-hexylthiophene-2,5-diyl) (P3HT) of $M_W > 45$ kDa; 93% regio-regularity) was purchased from Luminescence Technology Inc. (Lumtec). Chloroform, toluene, and methanol purchased from Sigma Aldrich were used as solvents for preparing the HV-ESD solution; all solvents were anhydrous and degassed using argon gas. For the depositions, 1×1 cm² n-type (phosphorus doped) silicon wafers with a native oxide layer (SiO_x), indium tin oxide (ITO) coated glass slides, and quartz were used as substrates.

4.2.2 Sample preparation

We employed an HV-ESD system by MolecularSpray (UHV4iH) which is differentially pumped by three pumps, two roughing pumps and a turbo-molecular pump (as the last stage before the HV chamber) in order to retain HV conditions in the recipient. The polymer solution is injected into a stainless steel emitter (New Objective Taper Tip, internal diameter: 100 μm) with the help of a syringe pump. In this system, P3HT becomes ionized on its trajectory and is deposited from the gas phase on the conducting substrate placed in the HV chamber (base pressure $< 2 \times 10^{-8}$ mbar, pressure during deposition: 1×10^{-6} mbar) after traveling through an inlet/entrance capillary with an internal diameter of 0.25 mm; the emitter capillary is regularly flushed with pure solvent for longer deposition times. The distance between the emitter and inlet capillary was set to be 3 mm for all the depositions. UHV4iH comes with a vacuum-side internally integrated inlet capillary heater to help with the desolvation of any residual solvent that enters the inlet capillary. If used, the heater is factory set to 100°C and auto-regulates its temperature. A high voltage of 2 kV- 5 kV was applied to the emitter to get a stable plume. Polymer concentrations in solution of 0.1 mg/mL and 1 mg/mL were used for chloroform and toluene. The solution of P3HT in toluene was further diluted by adding methanol in a 6:1 ratio and then filtered using a 45 μm particle size nylon syringe filter before HV-ESD. In contrast to vacuum deposition of COMs *via* thermal sublimation, we note that a quartz crystal microbalance for monitoring the deposition rate could not be satisfactorily used in our setup, likely due to the often discontinuous nature of the film deposition process. Instead, we directly used the ion current at the sample position as an indicator for the arrival of ions and, thus, thin film deposition. To this end, the sample was contacted *in vacuo* (exclusively using shielded connections on a UHV manipulator by CreaTec Fischer & Co. GmbH, Germany) and the ion current was recorded using a Keithley 6485 picoammeter providing a readout of current versus time data using a custom program established in LabView.

4.2.3 Sample nomenclature

HV-ESD samples deposited from toluene:methanol solvent mixture and chloroform were categorized into two series referred to as series TM and CF. The films in these series were

further sub-categorized according to whether they were deposited *without* or *with* an inlet capillary heater. From series TM and CF, the films that were deposited *without* using an inlet heater are referred to as series TM-a, and CF-a, respectively, those deposited *with* an inlet capillary heater as series TM-b, and CF-b.

4.2.4 Grazing incidence X-ray diffraction

Grazing-incidence X-ray diffraction (GIXRD) data was collected at Canadian Light Source (CLS) Saskatoon, SK, Canada, at the Brockhouse Low Energy Wiggler Beamline using a Rayonix MX300 detector. The primary beam wavelength was 0.82 Å and incidence angles between 0° and 0.12° were used for GIXRD diffraction experiments in order to change the surface sensitivity of the experiment. The open-source software GIDVis (<https://www.if.tugraz.at/amd/GIDVis/>), GPL v3.0, was used for the transformation of raw GIXRD data into 2D reciprocal space maps; [173] the 2D reciprocal space maps are shown in the section 4.5.

4.2.5 Absorption spectroscopy

The ultraviolet/optical/near-infrared absorption spectra (UV-vis/NIR) of the ESD solutions were obtained using Varian Cary 5000 UV-vis/NIR spectrophotometer with an average time of 0.033 sec per 1 nm data interval using quartz cuvettes of 0.2 mm effective path length. The aggregation behaviour of P3HT in toluene:methanol was studied using a P3HT-toluene solution of 0.5 mg/mL initial concentration. This solution was left for 30 min to let P3HT fully dissolve in toluene and then the solution was filtered using a nylon syringe filter (particle size ~45 µm) before recording the absorption spectra. Thereafter, the same solution was diluted with methanol in a 6:1 (toluene:methanol) ratio and filtered before recording the absorption spectra, without any time delay. This solution was then left for 1 hour, filtered, and again characterized with optical absorption spectroscopy. The absorption spectra of unfiltered P3HT in chloroform was recorded using 0.1 mg/mL concentration and the UV-vis/NIR spectra were recorded within 10 min of preparing the solution. For comparison with P3HT in chloroform, a P3HT-toluene solution of similar concentration was prepared, left for 30 mins, and then used without filtering to record the UV-vis/NIR spectra.

Fourier-transform infrared spectroscopy (FTIR) was performed in grazing-incidence reflection geometry (GI-FTIR) using a Bruker Vertex 70v under vacuum conditions ($p < 10^{-1}$ mbar, LN-cooled MCT detector) to enable performing FTIR on conductive substrates, as required by ESD. In this setup, the grazing incident angle of the infrared beam is 6.3° with respect to the sample surface (specular reflection). In order to ensure comparability of the recorded peak intensities of all samples, great care has been taken to keep the beam footprint on the samples nominally identical by using identical sample sizes and positions (spread in size \pm 10%); the GI-FTIR data for all samples are depicted in figure 4.12 in the section 4.5. The data have been recorded under nominally identical experimental conditions and are depicted as raw data without normalization. Reference FTIR data for transmission geometry was recorded using a Thermo Scientific Nicolet 6700 with the sample under dry N₂ atmosphere in sealed, custom made boxes with KBr

windows (LN-cooled MCT detector); the intensities of this reference scan are therefore not comparable.

4.2.6 Atomic force microscopy

The morphology of the electrosprayed films was analyzed using a Bruker MultiMode 8HR atomic force microscope (AFM) in tapping mode. The AFM scans were performed using ACTA aluminium coated n-type silicon probes (AppNano) of 13-77 N/m force constant; software Nanoscope 9.7 was used for AFM data acquisition, analysis, and representation.

4.3 Results and Discussion

P3HT can rightly be regarded as the “work-horse” in research focused at opto-electronic devices based on conjugated polymers, [47, 203–206] especially for organic solar cells. [202, 207, 208] P3HT is a semi-crystalline polymer with a microstructure sensitive to the specific solution-processing technique employed and preparation parameters used. Thus, we attempt here to establish P3HT films grown under *minimal solvent influence* by HV-ESD and assume that the absence of the solvent during nucleation and crystallization will heavily impact the resulting film. To this end, desired conditions for that experiment would imply using a solvent, that is (i) fully compatible with the electrospray process, (ii) readily evaporates and is pumped off before reaching the substrate, and (iii) completely dissolves P3HT. For HV-ESD it is generally known that, apart from polymer type [209] and its solubility in a given solvent, [210] the solvent properties including surface tension [164], vapor pressure [211] and polarity, [212] can heavily impact the experiment. In addition, the deposition rate of the polymer ions—governed by the injection rate of the polymer solution (i.e., the speed at which the polymer solution is pumped into emitter capillary of ESD unit)—heavily affects the resulting film morphology and structure [213]. Therefore, we focus in this study on the interrelation between solvent properties and injection rate on the film growth. We chose two common solvents for our study: chloroform as low boiling point (BP) solvent (BP: 61°C [214]) and a binary solvent mixture of toluene (high BP: 111°C [214]) and methanol (low BP: 64.6°C [215]) in 6:1 ratio with their deposition parameters carefully optimized for the pure solvents. P3HT films were then deposited via HV-ESD from these solvents at varying injection rates and analyzed for their structural properties using GIXRD. This analysis reveals that we can establish amorphous P3HT films via HV-ESD.

4.3.1 Optimizing deposition parameters

First, we tested HV-ESD of pure solvents and of a binary solvent mixture (all without polymer admixture) to assess if the solvent itself generates ion current on the substrate. This would indicate that solvent molecules are being ionized and do, indeed, reach the substrate instead of readily evaporating on their trajectory. To this end, we tested combinations of toluene (as higher boiling point solvent) and chloroform (as lower boiling point solvent) with methanol at various injection rates and applied voltages. The ratio

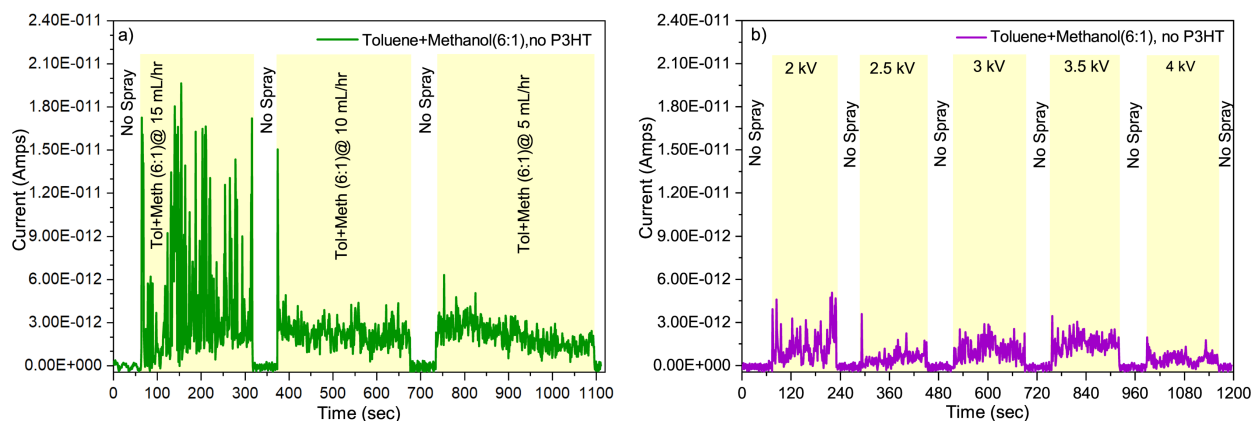


Figure 4.1: (a) Ion current versus time for the mixed-solvent system of toluene: methanol in 6:1 ratio (no P3HT added), with varying nominal injection rates of 15 mL/hr, 10 mL/hr and 5 mL/hr. (b) Same but with variable high voltage applied to the emitter (10 mL/hr nominal injection rate). The ion current values are recorded against a metal sample holder and the current corresponding to solvent spray are highlighted in yellow.

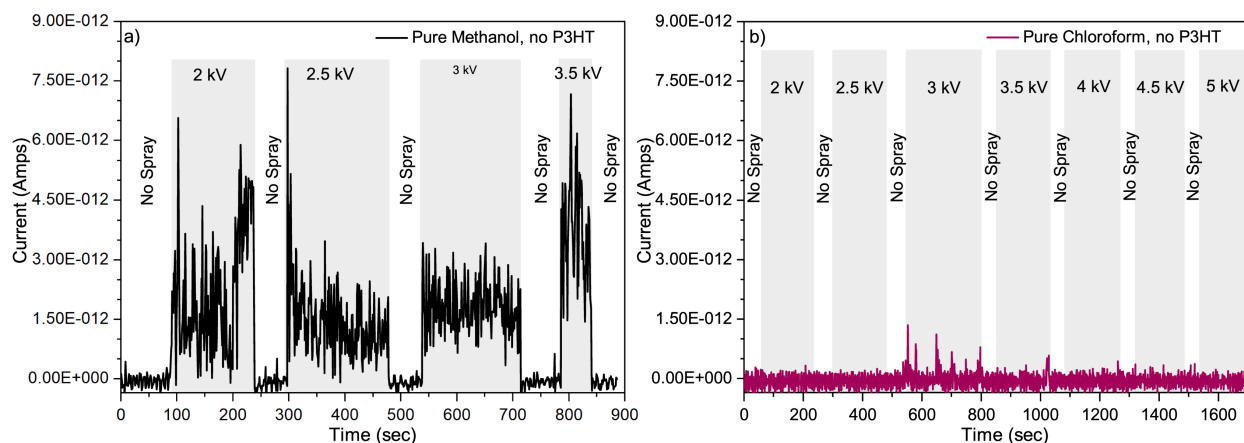


Figure 4.2: (a) Ion current versus time for pure methanol (no P3HT added) and (b) pure chloroform using 10 mL/hr nominal injection rate; the high voltage applied to emitter is given in the figure, data recorded against a metal sample holder.

of methanol used throughout this work in toluene: methanol solution was chosen empirically such that the maximum voltage needed for jet formation in HV-ESD is lower than 3 kV. This is further inspired by a literature report where the authors noticed that the P3HT films appeared dark carbonized when the films were deposited from chloroform using voltages above 3 kV in HV-ESD. [213] Furthermore, toluene and chloroform were chosen because they represent extremes regarding solubility of P3HT, that is, a marginal and good solvent, respectively. Figure 4.1(a, b) show the ion current versus time plots recorded for a metal sample holder placed at the sample position (determined by a laser) for toluene: methanol pure solvent mixtures (without P3HT) at varying injection rate, and applied voltage.

It is known for ESD that different injection rates can impact the size, structure, and

morphology of electrosprayed films. [211, 213, 216] To test the effect of injection rate in our experiment, we chose three different rates (figure 4.1(a)): 15 mL/hr, 10 mL/hr, and 5 mL/hr; voltage was kept constant at 2 kV which was identified as the minimum voltage at which a stable single cone jet could be obtained (see below). While the ion current for 5 mL/hr and 10 mL/hr appears similar (between 2 and 4 pA), the sample current is over-proportionally increased to up to 17 pA for the highest nominal injection rate (15 mL/hr). This indicates that toluene is able to largely evaporate before reaching the substrate for injection rates below 10 mL/hr only. The 10 mL/hr injection rate was therefore chosen to assess the impact of different high voltage values ranging from of 2 kV to 5 kV (figure 4.1(b)). While the sample current does not vary significantly upon changing the high voltage, the geometry of the charged jet does: a single cone was observed for 2 kV, it fluctuated between single and multi-jet for 2.5 kV, and became clearly multi-jet for 3 kV and beyond. The jet became unstable at 3.5 kV and, therefore, no higher voltages were tested for toluene:methanol. Thus, 2 kV voltage was identified as reasonable value for stable single jet mode in HV-ESD. We note that carefully assessing these experimental parameters in HV-ESD is particularly important for P3HT, because the voltage required to maintain a stable single cone jet was found to vary depending on the surface tension and conductivity of the polymer/solvent-mixture solution. [216]

To keep identical parameters throughout our study, we equally used 10 mL/hr of nominal injection rate for pure methanol, toluene, and chloroform (with varying voltages) to assess their impact on the sample current. Note that different voltage values are required owing to the different polarity of the solvents. Notably, we observed that pure toluene could *not* be reasonably electrosprayed using voltages up to 5 kV (which is the upper limit of our experimental setup). For pure methanol and voltage values between 2 kV and 3.5 kV (figure 4.2(a)) we find comparable (and substantial) sample current; the spray geometry was only stable at 2 kV while for 2.5 kV and beyond it clearly changed to multi-jet. Importantly, however, as shown in figure 4.2(b), *no* ion current was recorded when pure chloroform was electrosprayed for the whole range of applied voltages between 2 kV and 5 kV (again for 10 mL/hr). For chloroform, the Taylor-cone geometry was mainly droplets for 2 and 2.5 kV. At 3 kV a stable jet was observed which changed into multi-jet for voltages above 3.5 kV.

We thus conclude that pure chloroform can be an excellent solvent for HV-ESD of P3HT, because (i) it represents a (comparably) *good* solvent for P3HT, [214], (ii) no ion current is observed which implies that chloroform readily evaporates before reaching the substrate. Alternatively, one could speculate that chloroform instead remains neutral in ESD, which is, however, in clear contrast to other solvents such as methanol where ionization in the presence of a strong electric field is well established in literature on electrospray ionization [217, 218]

4.3.2 Assessing pre-aggregation in solution

Based on the Hansen solubility parameters of chloroform [214] it can be expected that P3HT is *well dissolved* in chloroform due to the stronger polymer-solvent interactions as compared to polymer-polymer interactions [219]. In contrast, P3HT has the known tendency to form aggregates in moderate solvents such as p-xylene, toluene, or upon

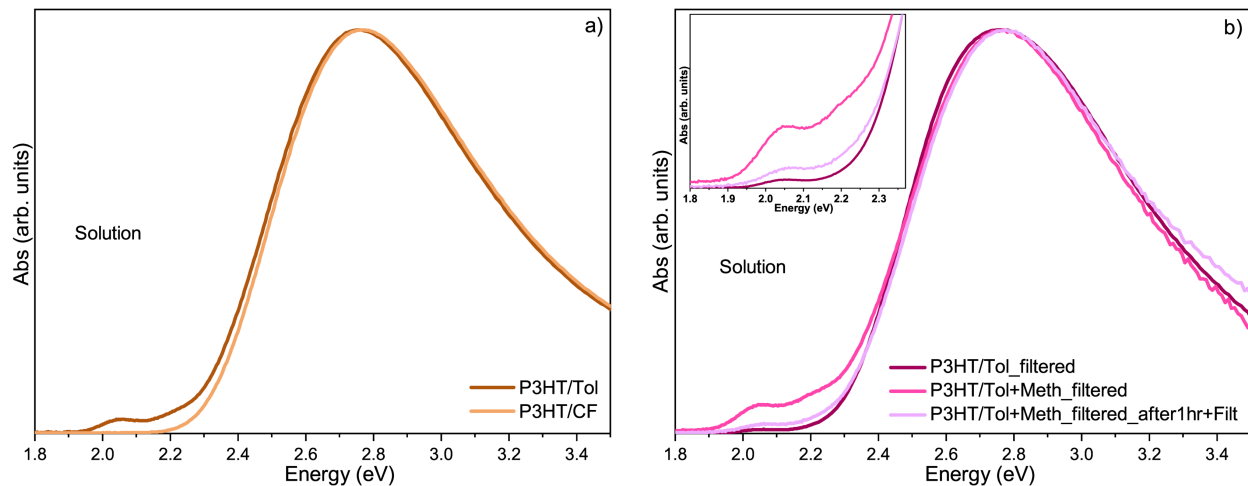


Figure 4.3: Comparison of absorption spectra from solution of P3HT in (a) toluene:methanol (6:1) and chloroform. (b) toluene and toluene:methanol (6:1)

addition of poor solvents like methanol, acetonitrile, or acetone to good solvents, as discussed in detail by Roesing et al. who studied the solubility characteristics of poly(3-hexylthiophene) for essentially all relevant solvents. [220] Thus, when using a solvent mixture for HV-ESD of P3HT we must speculate that crystalline pre-aggregates of P3HT could, in fact, occur and aggregates be electro sprayed, which could then be misinterpreted as surface crystallization. Therefore, before using the P3HT solutions in chloroform and toluene:methanol for HV-ESD, we performed UV-vis/NIR spectroscopy on the solutions in order to test for the spectroscopic fingerprint of aggregated P3HT.

We first performed UV-vis/NIR spectroscopy on filtered P3HT solution in pure toluene and toluene:methanol. A subsequently filtered P3HT solution was then electro sprayed on SiO_x (immediately after filtration). For comparison, we also performed absorption spectroscopy on P3HT dissolved in chloroform and used the same solution for HV-ESD of P3HT. Figure 4.3(a) shows a comparison of the solution absorption spectra of P3HT in toluene and chloroform. The absorption spectrum for 0.1 mg/mL P3HT dissolved in chloroform shows a maximum at ~ 2.77 eV which is due to fully dissolved, coil-like P3HT chains. [221] The same concentration of P3HT in toluene shows the same maximum, however, along with another vibronic absorption feature at 2.06 eV. This lower energy feature is indicative of π -stacked crystalline aggregates due to planarized P3HT chains [222]. Figure 4.3(b) shows a comparison between the absorption spectra of filtered P3HT solution in toluene (magenta curve), and in toluene:methanol (pink curve in figure 4.3) done on 0.5 mg/mL concentration P3HT solution. The fundamental absorption of P3HT around 2.76 eV does not shift when methanol is added to the P3HT/toluene solution. But the additional absorption feature at 2.06 eV now increases significantly as compared to P3HT dissolved in pure toluene (inset of figure 4.3(b)). This is expected because P3HT has poor solubility in methanol and the extent of aggregation increases upon addition of a poor solvent. When this filtered solution was left to rest for an hour, which represents the reasonable timescale of a typical HV-ESD experiment, the aggregation-related feature at 2.06 eV decreased after filtering again. This confirms

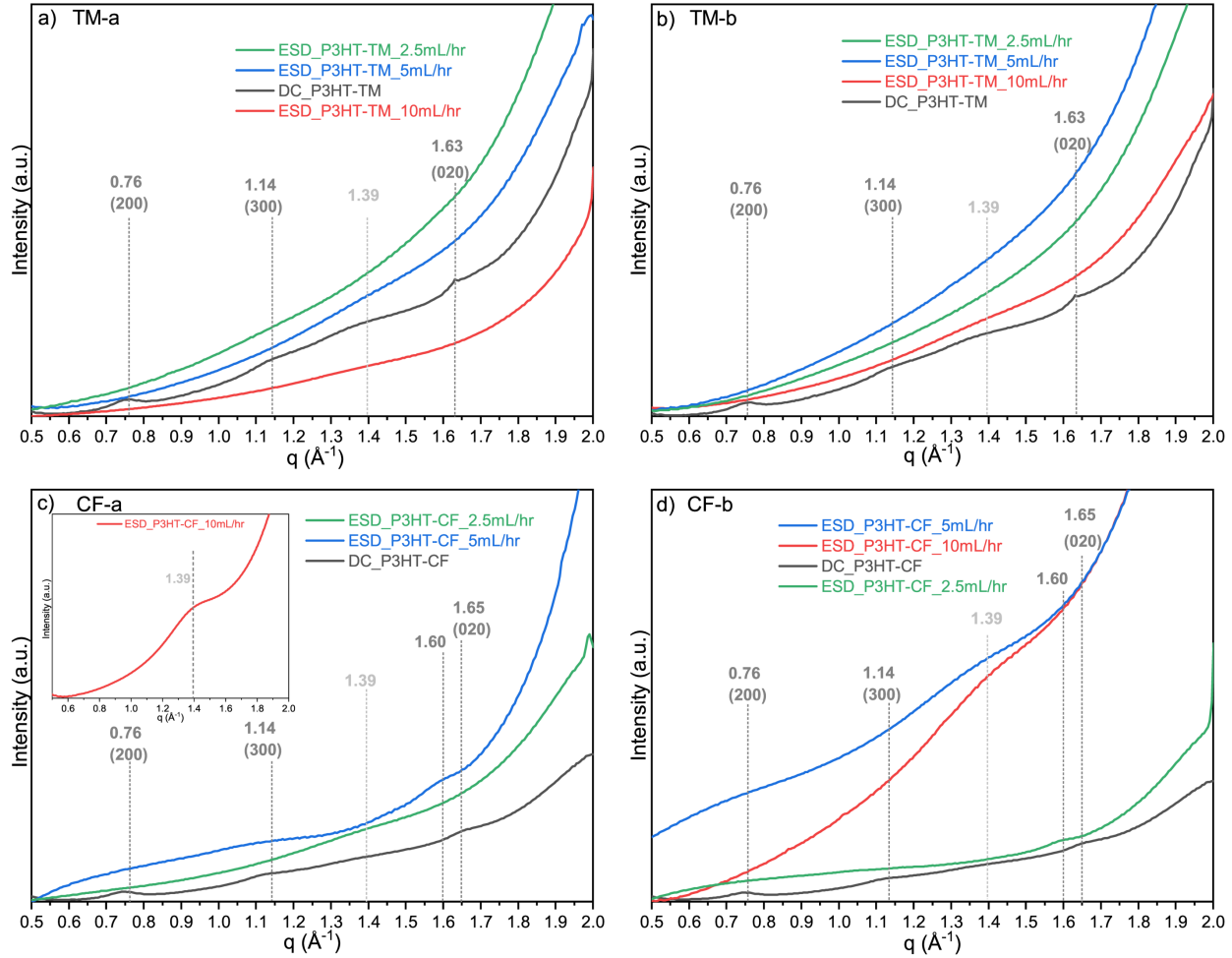


Figure 4.4: Grazing incidence X-Ray diffraction results from P3HT films deposited *via* HV-ESD on SiO_x substrates from (a), series TM-a using toluene: methanol as solvent without inlet heater (b), series TM-b with toluene: methanol applying the inlet heater, (c) series CF-a using chloroform without inlet heater, and (d) series CF-b using chloroform applying the inlet heater; the peak corresponding to the (100) lattice planes has been omitted here for better visualization of peaks showing weaker intensity.

that P3HT does form crystalline aggregates repeatedly in the toluene: methanol solution which must therefore be considered in HV-ESD experiments.

4.3.3 Structure by grazing incidence X-ray diffraction

The structure of P3HT films established by HV-ESD on SiO_x from toluene: methanol (series TM-a, TM-b) and chloroform (series CF-a, CF-b) was then characterized using synchrotron GIXRD. The GIXRD results from series TM-a, TM-b, CF-a, CF-b, along with dropcast films from both solvent types as a reference are shown in figure 4.4, the corresponding 2D reciprocal space maps are shown in the section 4.5. The dropcast P3HT reference film from toluene: methanol (black curve in figure 4.4(a, b)) exhibits the expected

structure and texture reported in literature before. [203] It shows diffraction peaks stemming from the ($h00$) and (020) lattice planes. Diffraction intensity from the ($h00$) planes appear in GIXRD close to the out-of-plane direction of scattering vector q (i.e., close to q_z at $q_{xy} = 0$) which indicates preferential stacking along hexyl side chains of P3HT (commonly referred to as “edge-on”); these planes exhibit a lattice spacing of $d_{100} = 16.5 \text{ \AA}$ (via $d_{hkl} = 2\pi/q$). The additionally observed diffraction from the (020) planes correspond to a spacing of $d_{020} = 3.85 \text{ \AA}$ which is the π - π stacking distance of P3HT lamellas (seen preferentially in q_{xy} at low q_z , that is, along the in-plane component of q). The d_{100} and d_{020} lattice spacings suggest that a P3HT polymorph commonly referred to as Form-I (which shows no side-chain intercalation) [223] is obtained by dropcasting P3HT in toluene:methanol solution. This is the form most commonly found in thin films. [102]

Now switching to P3HT films obtained *via* HV-ESD from toluene:methanol (referred to as series TM-a, TM-b), in marked contrast to the dropcast films, GIXRD did not reveal sharp peaks originating from crystalline P3HT, as seen in figure 4.4(a, b). Rather, a broad peak centered around a q value of 1.39 \AA^{-1} (lattice spacing 4.52 \AA) was observed for films deposited using 10 mL/hr and 5 mL/hr as nominal injection rates; note that it is not observed for the 2.5 mL/hr film possibly due to a lower film thickness in that case. We interpret this broad peak, which is equally present in the dropcast film (and, notably, absent for any bare substrate reference), as *amorphous scattering feature*, [224] which has been reported before using Laue X-ray diffraction on P3HT at the same position [225, 226] (together with the aforementioned peaks from the crystalline portion). We stress that the diffraction intensity of an amorphous halo—due to only some local order—is expected to be significantly lower than that of crystalline portions. Therefore, observing the amorphous halo without any indication of the diffraction peaks related to crystalline P3HT indicates that the film is, indeed, highly amorphous. The GIXRD results of the films in series TM-a and TM-b do not considerably change upon varying the injection rate or using the inlet heater (figure 4.4(a, b)).

For preparation from chloroform (figure 4.4(c, d)), the dropcast P3HT film reference (black curve) shows, again, the features assigned to the Form-I polymorph, now with less amorphous scattering. The HV-ESD films from chloroform, referred to as series CF-a (without inlet heater) and series CF-b (with heater), mostly show the same trend as series TM-a, TM-b from toluene:methanol as discussed above. Again, a broad peak around $q = 1.39 \text{ \AA}^{-1}$ is found for the fastest nominal injection rate of 10 mL/hr (both without and with an inlet heater) and for the slowest rate of 2.5 mL/hr (without heater). While still the diffraction peaks found for the dropcast (crystalline) film are absent, the film established at intermediate rate without heater (5 mL/hr, blue curve in figure 4.4(c)) and that from lowest rate with heater (2.5 mL/hr, green curve in figure 4.4(d)) show a single, weak peak around $q = 1.60 \text{ \AA}^{-1}$ (lattice spacing 3.93 \AA). This position is notably close to, but still well-separated from the (020) peak position found for the crystalline film established *via* dropcasting, which there corresponds to the P3HT π -stacking in Form-I of P3HT. The similarity in lattice spacing to the Form-I d_{020} (3.81 \AA) can be interpreted as some π -stacking to occur here as well. Given that for the integrated reciprocal space maps the ratio of the intensities related to the (100) and (020) lattice planes is ca. 10:1 (in the film dropcast from chloroform), the absence of the ($h00$) series in this case would

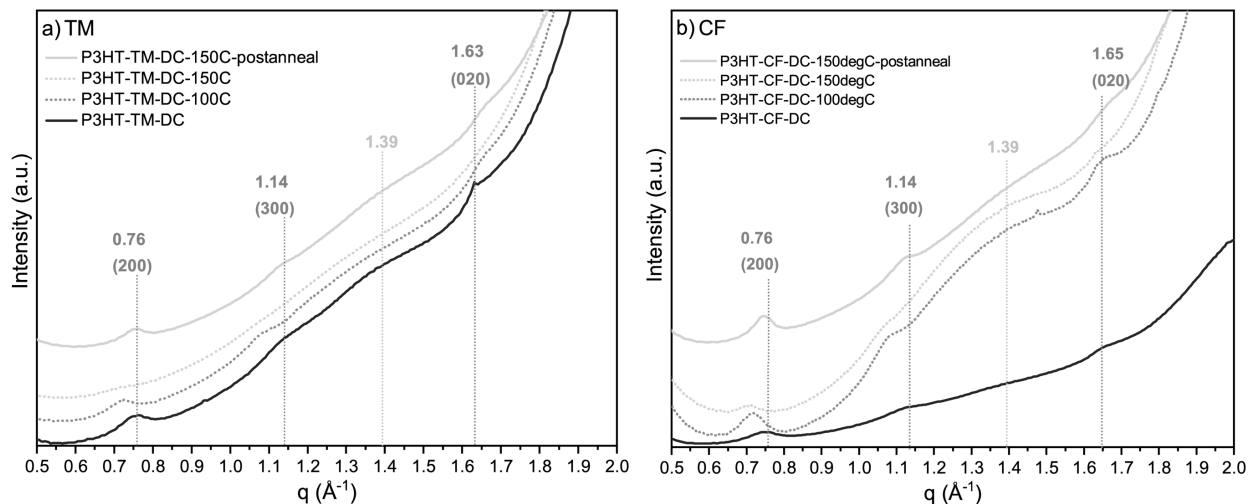


Figure 4.5: Grazing incidence X-Ray diffraction results from dropcast P3HT films deposited on SiO_x wafers from (a) series TM using toluene:methanol as the solvent, (b) series CF using chloroform. The solid black curve represents the reference data at room temperature, dark and light grey dashed curve indicate data recorded on films heated *in-situ* under helium atmosphere to 100°C and 150°C, respectively; the solid grey curve corresponds to post-annealed films allowed to cool down from 150°C to room temperature.

then mean that these structures lack periodicity in the direction of the P3HT alkyl chains which might be due to the highly different growth scenario in HV-ESD.

The morphology of above films is further examined using AFM, the corresponding micrographs are provided in the section 4.5 (figures 4.7 and 4.8). All ESD samples show morphologies characterized by typical features of tens of nanometers in height and of lateral extensions in the 1000 - 2000 nm range. Taking into account the spatial dimensions of P3HT aggregation, e.g., as deduced from the single crystal structure reported by Rahimi et al. [102] showing polymer backbone packing distances of 0.43 nm (π -stacking direction) and of 1.31 nm (along the intercalated alkyl chains), the morphology features in AFM must correspond to an enormous number of polymers agglomerated on the surface. Notably, due to strong π - π interactions, conjugated polymers tend to exhibit a high nucleation probability if grown from solution with a critical nucleus size reported in the single-digit or low double-digit range for P3HT [227]. This indicates that the solvent-free growth on the surface enabled by ESD hampers polymer crystallization.

To independently confirm the interpretation of the peak around 1.39 Å as being due to amorphous scattering, the dropcast P3HT films from series TM and CF (found to grow in P3HT Form I) were *in-situ* annealed at 100°C and 150°C, the corresponding GIXRD data recorded at elevated temperatures and post annealing (at room temperature) are shown in figure 4.5(a, b). At 100°C, as can be expected, an increase in lattice spacing is seen for the ($h00$) planes for both series TM and CF. [228] At the same time, an increase in intensity of the peak around 1.39 Å (in series CF), and a decrease in intensity of the (020) feature representing the crystalline character of films is observed. This increase in

lattice spacing along the hexyl side-chain direction followed by loss of crystallinity has been explained before as a result of reordering of the main chain together with a conformation change of hexyl side-chains [229]. On increasing the annealing temperature to 150°C, the intensity of (*h*00) and (020) lattice planes nearly vanish and the intensity of the peak around 1.39 Å increases further. The loss of the peaks related to the crystalline lattice suggests melting of the P3HT films, while the fact that the broad feature prevails strongly supports its interpretation as amorphous halo. This is further confirmed by the data recorded for the film post annealing, where both films recover their (*h*00) diffraction features at the same lattice spacing which indicates re-crystallization into the commonly observed P3HT crystalline Form I. In particular for series CF (figure 4.5(b)), this is accompanied by a reduction of the amorphous halo in line with what one would expect for re-crystallization.

4.4 Summary

In summary, we have studied the growth of thin films formed by the conjugated polymer P3HT as established by *in-vacuo* electro spray deposition and juxtaposed the resulting structures with those established by conventional dropcasting from solution. To this end, we have iterated towards experimental parameters that allow for stable HV-ESD from common solvents. From the sample current recorded for the pure solvents during the HV-ESD experiment we found that chloroform does not yield current, which indicates it largely evaporates on its trajectory towards the substrate under vacuum. HV-ESD results in the growth of entirely amorphous P3HT films of this otherwise semi-crystalline conjugated polymer, as we show by grazing-incidence X-ray diffraction. HV-ESD as a preparation technique for amorphous films in general can thus be of great value for fundamental studies on semi-crystalline substances, where it is difficult to separate the information on structure-property relationships for crystalline and amorphous film portions. We are currently working on exploiting HV-ESD of P3HT to better understand the molecular electrical doping of this compound for the field of organic electronics, where it has been found that amorphous and crystalline film portions react highly differently to dopant exposure. As it is virtually impossible to inhibit the occurrence of weakly ordered/amorphous film portions, in turn, inhibiting crystallization and deliberately working with amorphous films will help isolating the spectral signatures of, e.g., charge transfer in disordered P3HT to better understand this semi-crystalline system.

4.5 Supplementary Data

The following data has been published as supporting information for the manuscript [20] that this chapter is based on.

4.5.1 Optimization of HV-ESD parameters

In order to deposit solvent-free P3HT films by HV-ESD, it is of utmost importance to identify the deposition parameters (injection rate, applied voltage, solution concentra-

tion) for which no solvent reaches the substrate in the high vacuum chamber.

4.5.1.1 Substrate requirement

The substrate requirements for HV-ESD is tested by electrospraying 1 mg/mL P3HT solution in toluene:methanol (6:1) on ITO (conducting) and quartz (insulator) substrates using voltages between 2.5 kV- 3 kV and injection rate of 5 mL/hr.

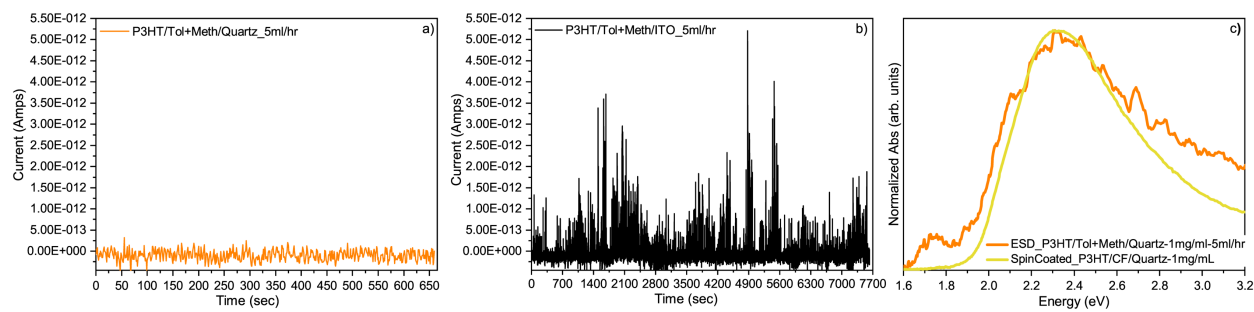


Figure 4.6: Ion current versus time plot for HV-ESD P3HT dissolved in toluene:methanol (6:1) using a nominal injection rate of 5 mL/hr and a voltage between 2.5 kV and 3 kV on (a) quartz and (b) ITO substrates. (c) Comparison of the absorption spectra a HV-ESD film of P3HT from in toluene:methanol (6:1) and of a spin-coat film of P3HT (from chloroform) as reference, both on quartz substrates.

Figure 4.6a,b shows the sample current (in amperes) versus time (in seconds) plot recorded for depositions on quartz and ITO, respectively. As expected, HV-ESD of P3HT on the insulating quartz substrate (Figure 4.6a) showed no ion current, while current in the picoampere range was recorded for deposition on ITO, as shown in Figure 4.6b. To assess whether P3HT was still deposited on the insulating substrate the optical to ultraviolet absorption spectroscopy (UV-vis) was performed on the quartz sample, the corresponding absorption spectra are shown in Figure 4.6c (orange curve). While significantly more noisy than the reference established by spin-coating—likely due to a significantly lower film thickness—the spectrum of the HV-ESD deposited film on quartz (orange curve in figure 4.6(c) is comparable to that of the reference (yellow curve), both showing fundamental absorption of P3HT. Therefore, although an insulating substrate was used for HV-ESD P3HT could indeed be successfully deposited. However, without access to sample current as a parameter to probe the deposition process, HV-ESD is difficult to control and can only be evaluated *ex-situ*, which largely limits its value. In addition, charged polymer ions arriving on the insulating substrate cannot be expected to become neutralized on the timescale of the deposition process due to a lack of connection to ground, which can lead to sample charging uncontrollably affecting the film growth and resulting morphology.

4.5.1.2 Solution Concentration

As the initial trial, we begun with HV-ESD of 1 mg/mL P3HT solution in chloroform and toluene:methanol solvents at 5 mL/hr injection rate and we were successfully able

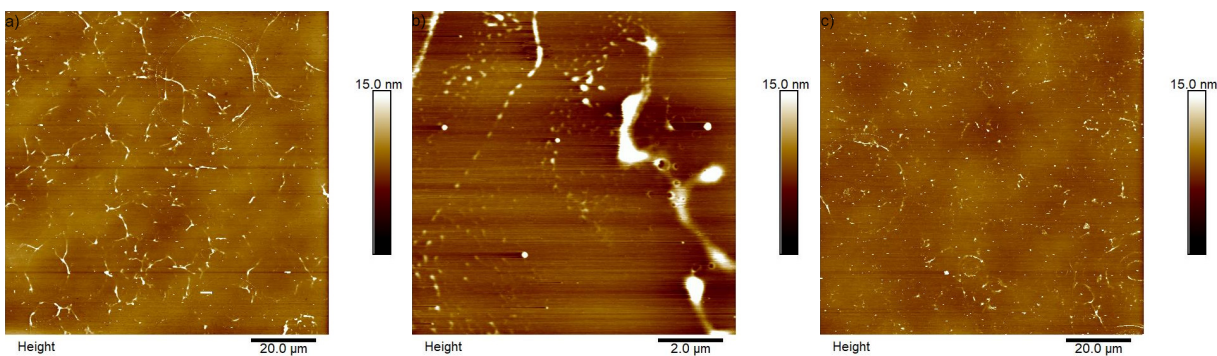


Figure 4.7: AFM images of HV-ESD P3HT films from series TM deposited on SiO_x using a nominal injection rate of 10 mL/hr without inlet heater in (a, b), and of 5 mL/hr without inlet heater in (c).

to deposit P3HT film from toluene:methanol solvent however no film could be deposited from this concentration of P3HT solution in chloroform. This concentration and injection rate led to the blocking of the inlet capillary which was judged by a reduction in pressure of the vacuum chamber and no ion current due to the absence of P3HT ions reaching the substrate. We then tried HV-ESD of P3HT at the same concentration but by increasing the nominal injection rate to 10 mL/hr. Although we did manage to deposit a film from this injection rate and concentration yet the deposition time was very tedious and time-consuming as the inlet capillary needed to be flushed after every few minutes. Therefore, for the next trials we started from a diluted concentration of 0.1 mg/mL P3HT in toluene:methanol and chloroform. The films from these trials are named as series TM and CF in the main text. The morphology of these films was investigated using AFM and their microstructure was probed using GIXRD (refer to section 4.3.3).

The HV-ESD films deposited from toluene:methanol without using inlet heater (i.e., series TM-a) are shown in Figure 4.7. As depicted in Fig 4.7(a) the film deposited at 10 mL/hr in series TM-a (without inlet heater) displays a combination of ring-like “coffee-stain” and dumbbell-shaped morphology. The “coffee-stain” morphology was first explained by Deegan et al. to be a result of rapid evaporation of solvent from pinned contact line of the drying droplet on the substrate surface. Due to capillary flow, the solvent lost from the edge of the droplet must be compensated by the solvent drawn from the center and is accompanied with the movement of solute from the center of the droplet towards the edges where the solute finally dries forming a rim of “coffee-stain” shape [230, 231]. While the dumbbell-shaped morphologies are formed when the charged particle of high molecular weight polymers undergoing Coulomb fission event(s) freezes during or after the fission [232]. During the Coulomb fission events, the larger or ‘parent’ charged particles break down into smaller particles or progeny particles. The presence of pores on the seemingly smooth P3HT particles (refer to figure 4.7(b)) is due to the faster evaporation of lower boiling solvent i.e., methanol thus leaving charged droplets/particles enriched in toluene that has a higher boiling [233]. Similar coffee-stain and dumbbell-shaped morphologies were observed for film using 5 mL/hr nominal injection rate (and without inlet heater) as shown in figure 4.7(c).

The morphologies of films from series CF-a, CF-b are of special interest given the

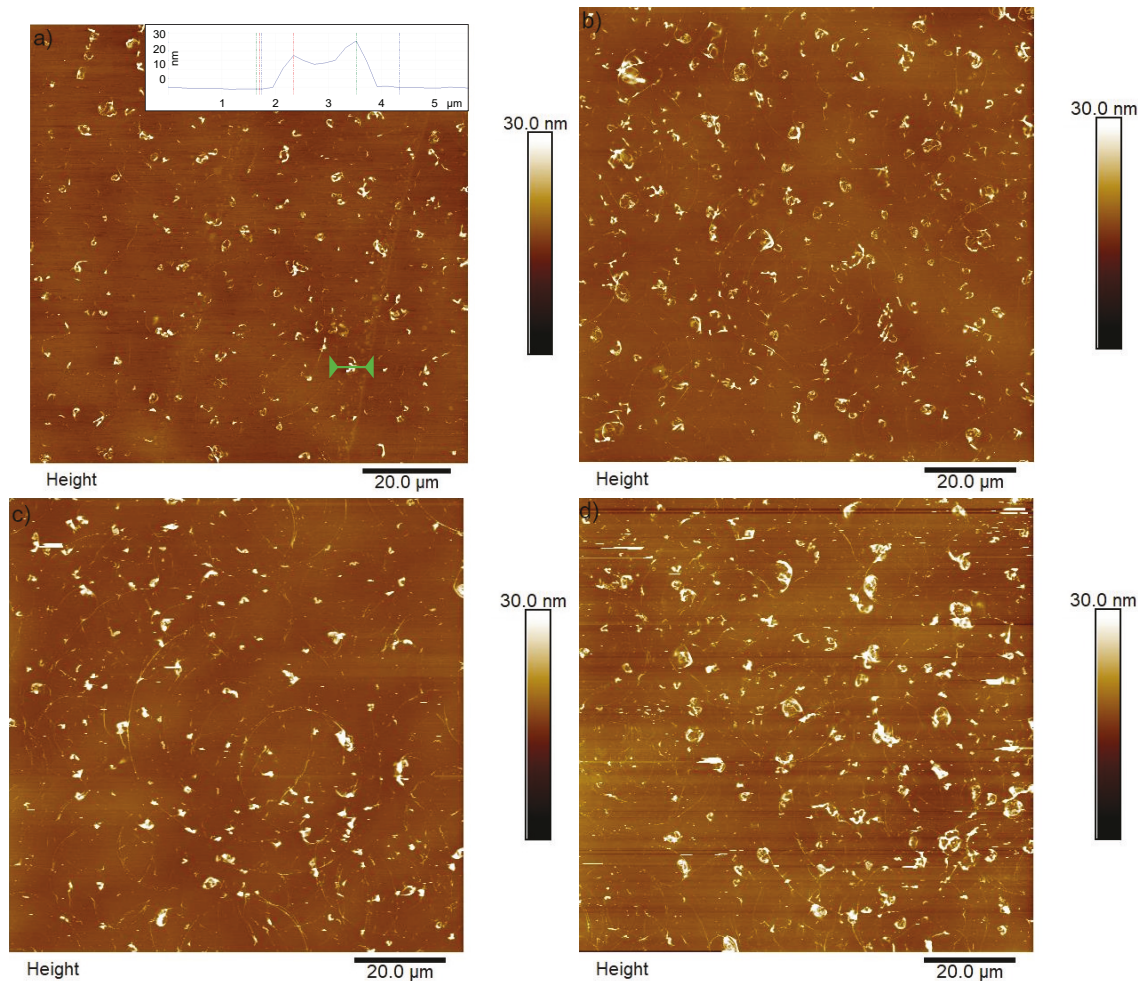


Figure 4.8: AFM images of HV-ESD P3HT films from series CF deposited on SiO_x using an injection rate of (a) 10 mL/hr without inlet heater, (b) 10 mL/hr with inlet heater, (c) 5 mL/hr without inlet heater, (d) 5 mL/hr with inlet heater. The inset in (a) shows a cross section of a characteristic morphology feature of the adsorbate, where vertical dimensions in the 10-30 nm, and lateral dimensions in the 1-2 μm regions are found.

dissimilarity in the structural arrangement as suggested by GIXRD results in the main text. Figures 4.8(a) and 4.8(b) demonstrates AFM images of films deposited at 10 mL/hr nominal injection rates without and with using an inlet heater, respectively. These films indicated cup-like, deflated spheres and porous, broken shell-like morphologies [234] and no distinction in morphologies (and structure from GIXRD) were observed for films deposited at 10 mL/hr from series CF-a, CF-b. However, films deposited using 5 mL/hr injection rate from series CF-a, CF-b (refer to figures 4.8(c) and 4.8(d)) depicted distinguishable particle shapes. Qualitatively, the film deposited without an inlet heater (belonging to series CF-b) displays particles with a more rigid and seemingly smoother surface unlike film deposited with an inlet heater which shows porous, deflated broken shell-like particles. The coffee-stain morphology was commonly observed among the

films shown in figure 4.8.

4.5.2 GIXRD reciprocal space maps

The GIXRD line scans in the main text have been generated by integration of 2D intensity data $I(q_{xy}, q_z)$ (figures 4.9 and 4.10, shown in the next two pages) after transformation into reciprocal space using the software GIDVis. [173]

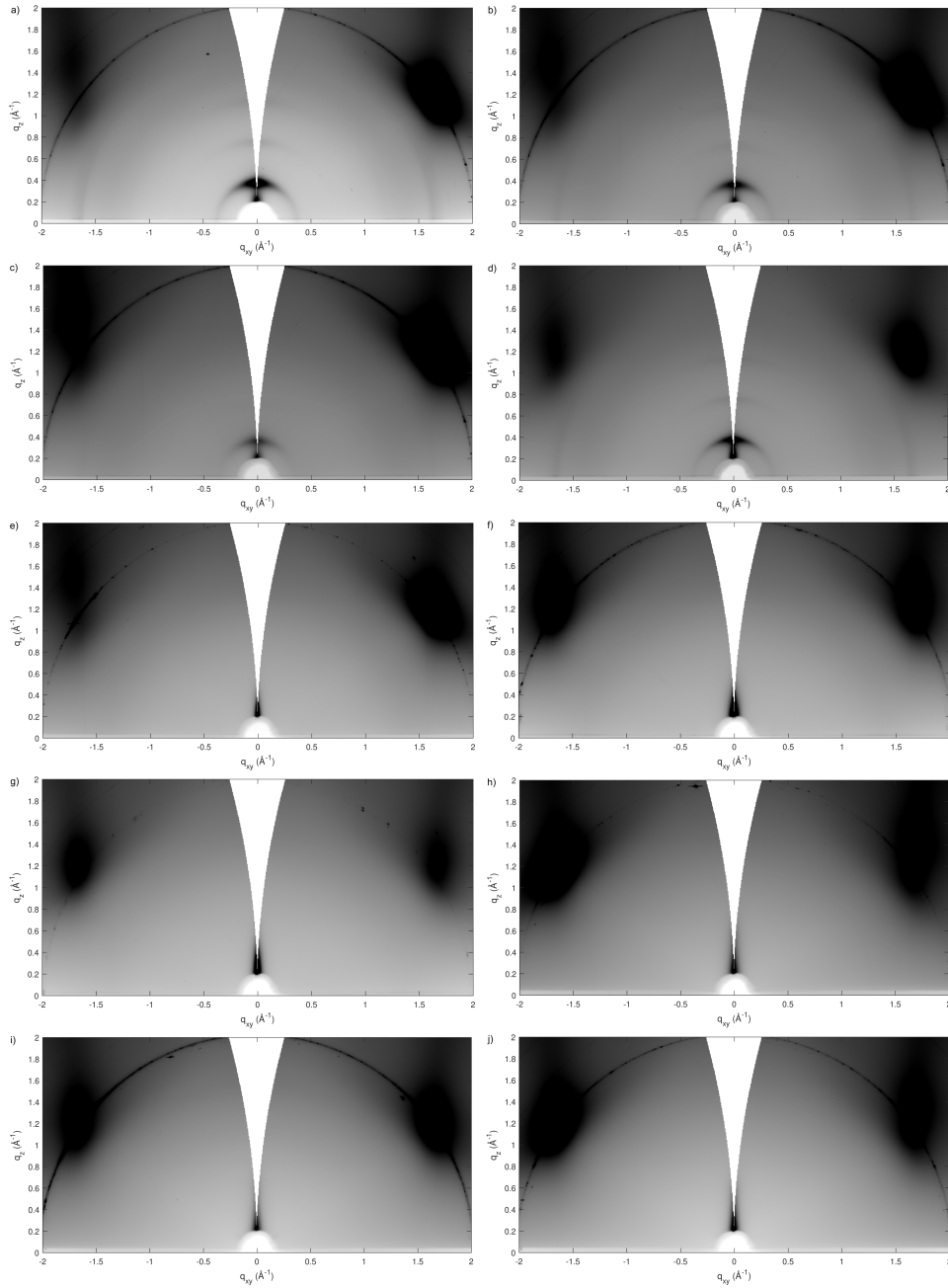


Figure 4.9: GIXRD reciprocal space maps from which the line scans in the main text are generated by intensity integration along $q = (q_{xy}^2 + q_z^2)^{1/2}$: Drop cast P3HT film from toluene: methanol at, (a) room temperature (b) during annealing *in-situ* under helium atmosphere at 100°C, and (c) 150°C, (d) post-annealed drop cast film allowed to cool down from 150°C to room temperature. HV-ESD P3HT films from series TM deposited on SiO_x using a nominal injection rate of, (e) 10 mL/hr without inlet heater, (f) 10 mL/hr with inlet heater, (g) 5 mL/hr without inlet heater, (h) 5 mL/hr with inlet heater, (i) 2.5 mL/hr without inlet heater, (j) 2.5 mL/hr with inlet heater; colors correspond to the square root of the recorded intensity.

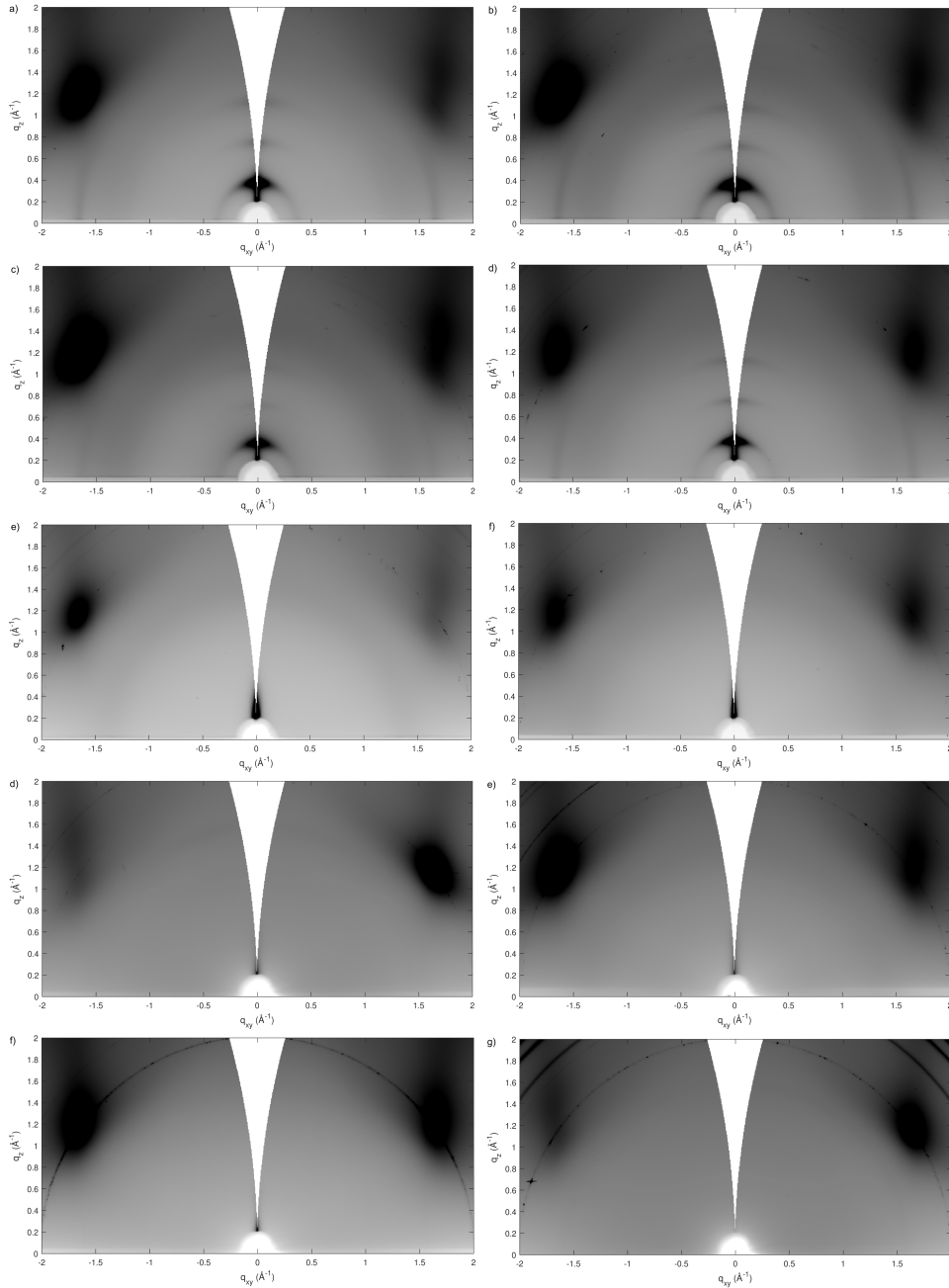


Figure 4.10: GIXRD reciprocal space maps from which the line scans in the main text are generated by intensity integration along $q = (q_{xy}^2 + q_z^2)^{1/2}$: Drop cast P3HT film from chloroform at (a), room temperature, (b), during annealing *in-situ* under He at 100°C, (c) 150°C, and (d) post-annealing allowed to cool down room temperature. HV-ESD P3HT films from series CF on SiO_x using a nominal injection rate of, (e) 10 mL/hr without inlet heater, (f) 10 mL/hr with inlet heater, (g) 5 mL/hr without inlet heater, (h) 5 mL/hr with inlet heater, (i) 2.5 mL/hr without inlet heater, (j) 2.5 mL/hr with inlet heater; black saturation corresponds to the square root of the recorded intensity.

4.5.3 GIXRD linescans with baseline correction

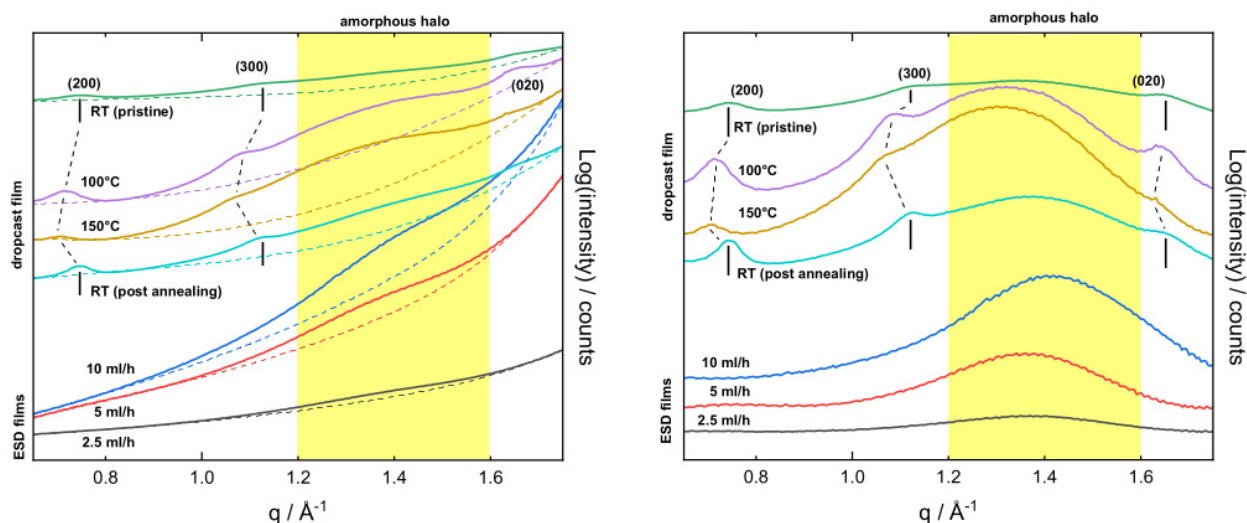


Figure 4.11: Left: Integrated linescan data (solid lines) for the reciprocal space maps shown in figure 4.10 together with baselines (dashed curves). Curves are shown for the samples established using the inlet heater; nomenclature as used throughout the main text. Right: Same curves but baseline corrected; the area of the amorphous halo is highlighted in yellow. All films were measured under He atmosphere, the dropcast film was heated *in-situ* to 100°C and 150°C and then let cool down again to room temperature (RT). This cooling cycle shows the expected shift of the Bragg peaks to higher values of q due to thermal expansion together with an increase in diffraction intensity of the amorphous halo at elevated temperature; post annealing, the Bragg peaks are again observed at their initial position. Notably, the ESD films also show the amorphous halo but no indication of Bragg peaks which evidences no detectable crystalline order; no change was observed upon annealing the ESD films (not shown). Importantly, the diffraction intensities shown in the figure are raw data, all curves have been recorded using identical experimental parameters (primary-beam footprint, integration time, synchrotron ring current due to top-up mode at the Canadian Light Source), therefore, the scattering intensities of the amorphous halos are indicative of the relative amount of amorphous P3HT present in the samples.

4.5.4 GI-FTIR spectroscopy

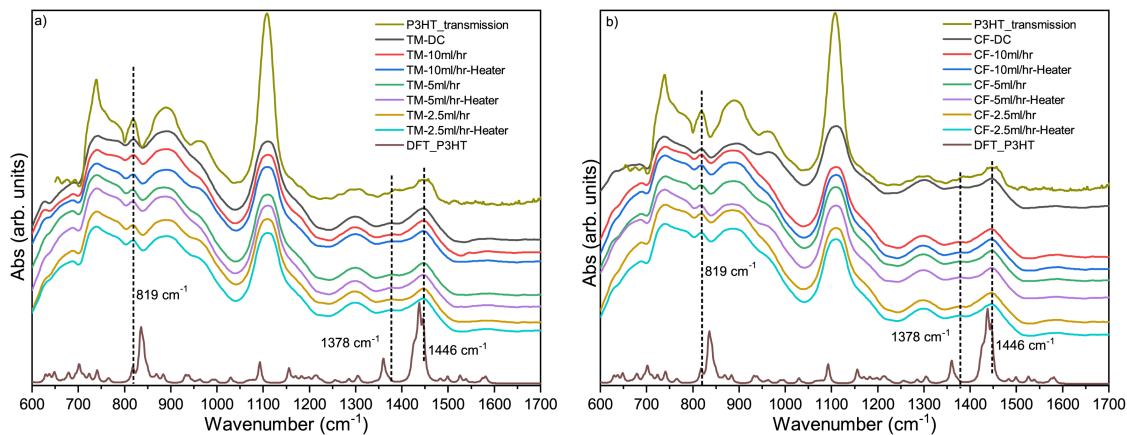


Figure 4.12: (a) GI-FTIR data recorded for the samples established by HV-ESD from toluene:methanol (series TM-a, TM-b) and (b) from chloroform (series CF-a, CF-b), together with data of the drop-cast reference. To interpret the data, a DFT-calculated vibrational spectrum (for a geometry-optimized 3-hexylthiophene heptamer calculated at the ω B97X-D[2]/6-31+g(d,p) level of theory in Gaussian 09 rev. E.01[3]) and an IR spectrum collected in transmission mode (for a dropcast sample on undoped silicon) are additionally shown. These reference data demonstrate the correspondence between the GI-FTIR data recorded on the HV-ESD films and the expected vibrations of P3HT. The vibrations in $1700\text{-}800\text{ cm}^{-1}$ region are the most characteristic for P3HT[4]: According to literature reports and in line with our DFT modeling, the peak at $\sim 820\text{ cm}^{-1}$ represents the out-of-plane C–H vibration of the thiophene ring,[5] that at $\sim 1377\text{ cm}^{-1}$ is assigned to methyl deformation,[4] while the vibrations around $1520\text{-}1440\text{ cm}^{-1}$ are due to symmetric and anti-symmetric vibrations of C=C in thiophene.[4, 5] The peak positions recorded in GI-FTIR data are 819 cm^{-1} , 1377 cm^{-1} and 1446 cm^{-1} , respectively, and thus agree well with the literature values, the peak positions obtained for FTIR in transmission, as well as the results of the DFT calculations. In analogy to the GIXRD data shown in figure 4.11, all GI-FTIR data are recorded under identical experimental conditions (grazing angle of the IR beam: 6.3°) and are not normalized, therefore, the relative intensities qualitatively allow assessing the relative P3HT content of the films, which turns out to be highly similar in all investigated samples.

Chapter 5

Aggregate Formation in Crystalline Blends of α -Sexithiophene and Para-Sexiphenyl

The content of this chapter has been published as:

S. Bhagat, W. Leal, M. Majewski, J. Simbrunner, S. Hofer, R. Resel, and I. Salzmann, "Aggregate Formation in Crystalline Blends of α -Sexithiophene and Para-Sexiphenyl" *Electronic Structure*, vol. 3, p. 34004, 2021.

Abstract

Earlier reports on rod-like conjugated molecules of similar shape and size such as α -sexithiophene (6T) and para-sexiphenyl (6P) indicated mixed crystal growth in equimolar blends. The spectral overlap between the 6P fluorescence and 6T absorption might there give rise to resonant energy transfer between the two species. In marked contrast to H-type aggregation found for 6T bulk crystals, isolated monolayers of 6T as well as 6T monolayers sandwiched between 6P multilayers have been reported to show pronounced green (instead of red) fluorescence, which has been attributed to J-type aggregation. Here, we investigate whether these altered optical properties of 6T translate from the monolayer to a bulk equimolar blend with 6P. Insight into the mixed crystal structure for vacuum films of 6T+6P is provided by using synchrotron grazing-incidence X-ray diffraction on different substrates. By correlating the optical properties of the pure and the mixed systems using absorption and photoluminescence spectroscopy we identify the green emission known from 6T monolayers to prevail in the blend. Our analysis indicates the formation of aggregates which are promoted by the molecular arrangement in the mixed crystal structure highlighting that the remarkable optical properties of 6T/6P heterostacks translate into mixed crystalline films. This study underlines that tuning the opto-electronic properties of organic semiconductors by blending species of similar shape but distinct opto-electronic properties is a promising pathway to achieve altered material properties.

5.1 Introduction

para-sexiphenyl (6P) has been intensively investigated due to its blue luminescence, thermal stability, and high quantum yield in the solid state and has been regarded as promising material in the research targeting organic light emitting diodes [235–237]. Equally, α -sexithiophene (6T) has been widely used in organic solar cells [238–240] and together with its alkylated derivatives in organic field effect transistors owing to a high field-effect mobility [241–243]. Apart from their individual properties, combinations of these rod-like molecules as layered systems have attracted much interest in the past. It has been reported that the emission from 6P/6T heterostacks can be tuned from yellow, red via white to blue by varying the stacking distance [8, 105–108], and that in epitaxially aligned nanofibers grown by the periodic deposition of 6T and 6P the lasing properties of the nanofibers could be tuned from deep blue to the red-orange [110]. In principle, the significant overlap between the spectral range of 6P emission and 6T absorption makes it possible to have efficient resonance energy transfer (RET) between these materials [111], and for the layered 6P/6T system it was observed that the optical properties of these heterostructures differ considerably from those of the pure materials [8, 105–111]. A characteristic green emission has been observed in the layered system, which adds to the blue and red emission from pristine 6P and 6T, respectively. In a study to investigate the green emission from that system, Schwabegger et al. [109] performed photoelectron spectroscopy and found a sharp interface between the 6T as deposited on 6P and no evidence for electronic coupling between the individual 6T and 6P molecules. Therefore, the origin of the green emission has been explained by the contribution from interfacial, isolated 6T which adds to the emission from the pure materials in their bulk crystal structures. Notably, studies by Vogel et al. suggested the possibility of mixed crystal structure formation by vacuum codeposition of 6T and 6P molecules, as deduced from specular X-ray diffraction (XRD) and Fourier-transform infrared spectroscopy (FTIR) [112, 244]. In the present study, we investigate whether mixed crystal growth indeed occurs in thin films of equimolar blends of 6T and 6P and whether the green emission observed for layered systems translates into such blends. By combining specular and grazing-incidence X-ray diffraction (GIXRD) we observe growth of a mixed crystalline structure similar to that of pristine 6P, which prevails both in lying and standing orientation. Via optical absorption and fluorescence spectroscopy we find that the green emission behaviour known from layered systems prevails in the codeposited films, which we explain by the underlying molecular arrangement.

5.2 Methods

Thin films were deposited by physical vapour deposition under high vacuum conditions (base pressure: 2×10^{-8} mbar) using 6P and 6T from TCI chemicals. 6P was used as received while 6T was purified by thermal sublimation before use (see schematics of the setup in the figure 5.8). The codeposited film of 6T and 6P was grown using a 1:1

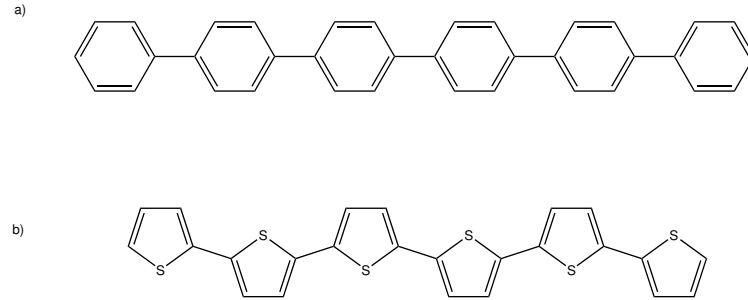


Figure 5.1: Chemical structure of (a) para-sexiphenyl (6P) and (b) α -sexithiophene (6T)

molar ratio of the materials. For the depositions, $1 \times 1 \text{ cm}^2$ quartz slides, silicon wafers (prime grade) with a native oxide layer (referred to as SiO_x in the following), and freshly cleaved highly oriented pyrolytic graphite (HOPG, ZYA quality) were used as substrates. The rate of deposition for all the films was set to $2 \text{ \AA}/\text{min}$ (rate of the individual materials and total rate) and was measured using a quartz crystal microbalance. To monitor the deposition rate during codeposition, first, we set the rate of the individual materials using a shutter; once the desired rate was set to be stable for both the sources, the substrates were exposed to the stream of vapours from the pure materials (see figure 5.8). The nominal film thicknesses of the codeposited films, as measured by the microbalance (using the average mass density of the pristine materials) was 30 nm for spectroscopy measurements and 20 nm for structural investigations.

The optical properties of the thermally deposited films were investigated using UV-vis/NIR spectroscopy (UV-vis/NIR), photoluminescence (PL) spectroscopy and infrared absorption spectroscopy (FTIR). The optical spectra were recorded on thin films deposited on quartz substrates. Optical absorption spectra of the samples were obtained by using Varian Cary 5000 UV-vis/NIR spectrophotometer with an average time of 0.033 sec and 1 nm data interval. The emission spectra were recorded using Horiba PTI Quanta Master 8075 spectrofluorometer (1 nm steps with 1 sec per step integration time). Infrared absorption spectra were recorded using Thermo Nicolet 6700 spectrometer. For infrared absorption spectroscopy, thin films on SiO_x substrates were used and the resolution of the infrared spectrometer was set to 4 cm^{-1} .

For structural analysis, pure and mixed films of 6P and 6T were grown on freshly cleaved HOPG and SiO_x by physical vapour (co-)deposition in the high vacuum. The films were characterized at beamline W1 at the synchrotron radiation facility DORIS (HASYLAB, Hamburg). GIXRD experiments were performed immediately after specular X-ray diffraction (without altering the sample alignment) using a goniometer (by Risø) in pseudo $2 + 2$ geometry and a one-dimensional detector (MYTHEN, Dectris); the use of a primary and secondary slit system (evacuated flight tube with entrance and exit slits behind the sample) allowed for recording high resolution data required for the precise determination of peak positions; the primary beam energy was 10.5 keV, peaks were fitted using Voigt functions. GIXRD experiments were performed using an incident angle of the primary beam relative to the substrates of 0.15° , alignment was done via surface reflection (SiO_x) and the HOPG (002) peak, respectively. Reciprocal space maps were

recorded by keeping the sample fixed and performing a series of detector scans along the in-plane scattering angle at differently fixed out-of-plane scattering angle, thus relying on the fiber textured growth of the adsorbate (on SiO_x) and the fiber texture of the HOPG substrate, respectively. The vertical mounting of the detector allowed the simultaneous measurement of ca. 3.5° in out-of-plane direction. The experimental diffraction pattern was transformed to reciprocal space using the custom-made software PyGID [172].

To determine the packing motif in the unit cell a combined experimental/computational approach was used, where to get the unit cell dimensions (table 5.1) a recently developed indexing routine [9] was employed. This crystallographic unit cell coming from experiment was then used as input for Molecular Dynamics simulations, which were carried out utilizing the LAMMPS software package [245] with the CHARMM general force field version 3.0.1 [246]. Several thousand trial structures are generated by placing one 6P and one 6T molecule with a random orientation in an expanded (140%) unit cell with periodic boundaries. No fixes are applied, and the molecules can freely move in this cell. During the simulation run, the unit cell was then continuously reduced in size to the experimentally determined value, while the molecules could find a relaxed conformation. Resulting candidate structures are clustered, based on their packing motif and high-energy solutions are discarded to make a final comparison of the calculated structure factors with the measured peak intensities from the GIXRD experiment (for our best solution see figure 5.12).

5.3 Results

5.3.1 Structural properties by X-ray diffraction

To investigate the growth of equimolar 6T+6P blends we performed XRD and GIXRD on films grown on SiO_x and HOPG, respectively, the results are shown in figure 5.2. The XRD results for the film on HOPG (top curve in figure 5.2a) shows, apart from the dominant HOPG (002) reflection, only one peak that we ascribe to the adsorbate. Its position at 1.406 \AA^{-1} corresponds to a lattice spacing of 4.47 \AA which is close to the strongest reflection of pure 6P, as calculated to 4.57 \AA for the 6P single-crystal structure reported by Baker et. al. [6] [position indicated by a vertical dotted line in figure 5.2(a)]; no indications of 6T related reflections are observed. We note that the deviation from the calculated 6P structure we observe for this peak is way beyond the error margin of our experiment for the following reasons: the HOPG (002) peak in figure 5.2a lies close to the reflection which we observe for the 6T+6P film, therefore, the error margin due to sample misalignment and wavelength determination is expected to be similar for both reflections. As the measured HOPG (002) peak position agrees with the calculated value within $7 \times 10^{-4} \text{ \AA}$ we expect the error margin of the adsorbate related reflection to be in the same range. Thus, the peak we observe in XRD on HOPG cannot be explained by pure 6P. In the XRD data of a nominally identical film on SiO_x [bottom curve in figure 5.2(a)] we find a series of equally spaced peaks starting at 0.2361 \AA^{-1} (position deduced from a fit of the third re-

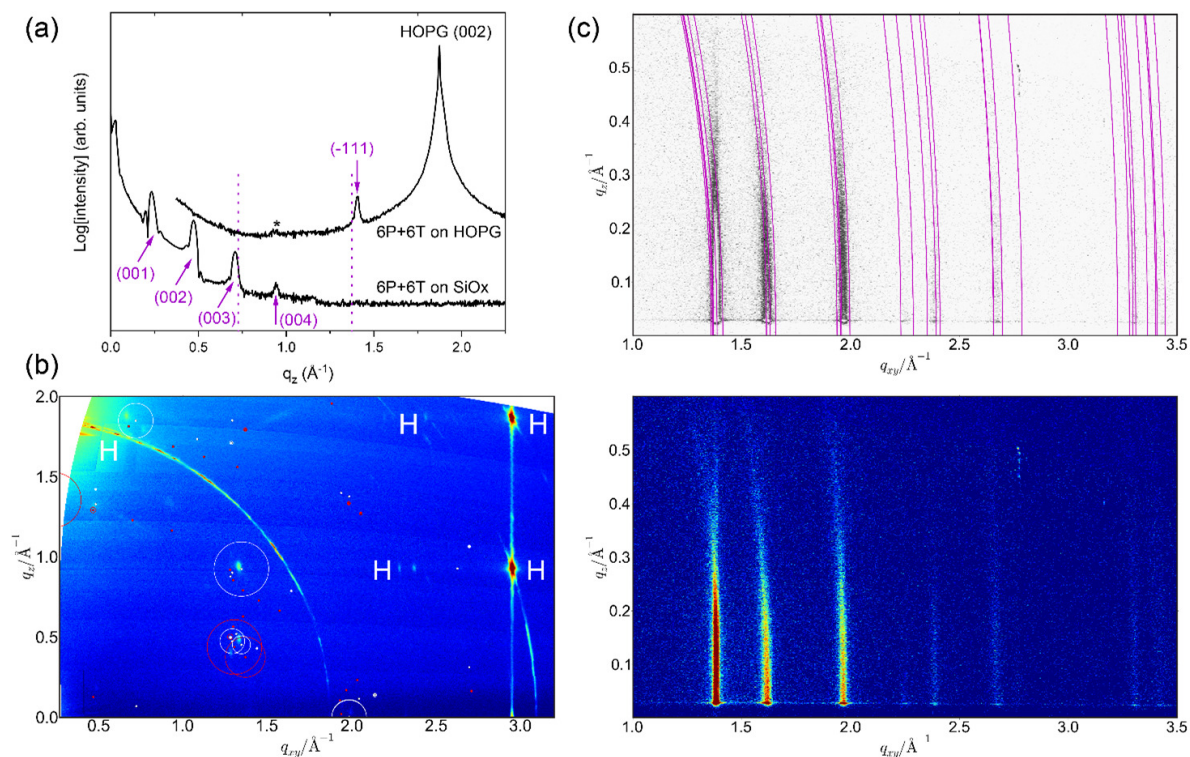


Figure 5.2: Structural analysis of 6T+6P films. (a) XRD on SiO_x and HOPG substrates, calculated peak positions for pure 6P (cell choice II) [6, 7] are indicated by vertical dotted lines for the (-111) reflection on HOPG and the (003) peak on SiO_x ; the asterisk marks a second order contribution by the substrate. (b) Reciprocal space map obtained by GIXRD on the film grown on HOPG showing the experimental data together with calculated reflections of pure 6P for (-111) orientation (white) and (-112) texture (magenta); diffraction intensity due to the HOPG substrate is labelled by 'H'. (c) GIXRD data for the film on SiO_x (bottom) and plotted together with Debye–Scherrer rings calculated for the strongest reflections based on our structure solution (top), which highlights the occurrence of vertical Bragg rods and the similarity of the mixed crystal structure on both substrates.

Parameters	6P+6T mixed film	Pristine 6P [6, 7]
a	5.696 Å	8.091 Å
b	7.836 Å	5.568 Å
c	26.888 Å	26.241 Å
α	83.62°	90°
β	86.42°	98.17°
γ	89.44°	90°
volume	1190.27 Å ³	1170.18 Å ³

Table 5.1: Comparison of the unit cell parameters refined for the equimolar mixed film and pristine 6P

flection) which corresponds to a lattice spacing of 26.61 Å and reminds of the (00*l*) series observed for pure 6P deposited on isotropic substrates [163]; as on the HOPG substrate, we find no indication of 6T related XRD features. The lattice spacing we observe here is, again, significantly different to the calculated values for the (001) reflection of the two 6P polymorphs known to grow on isotropic substrates (β -phase: 25.97 Å [6, 163], γ -phase: 27.24 Å [247]). From the well-defined side-oscillations of the first two peaks (Laue oscillations) we can estimate the out-of-plane coherence length of the film to be 158 Å (± 15), which is close to the nominal film thickness of 200 Å. The similarity to the 6P single-crystal structure [6] is also evident from our GIXRD data for 6T+6P on HOPG, which is shown in form of a reciprocal space map in figure 5.2(b). The peak positions calculated for pure 6P [6] are plotted in white for (−111)-texture (circle diameters correspond to calculated intensities). They lie close to, but deviate significantly from the experimental reflections; again, the strong reflections from the HOPG substrate [labelled by ‘H’ in figure 5.2(b)] can serve here as an internal reference for sample alignment. In the reciprocal space map, we also plot the calculated reflections for pure 6P in (−112)-texture, as this texture plane has a lattice spacing of 4.43 Å and is thus even closer to the XRD peak we observe figure 5.2(a); the calculated intensities (circles plotted in magenta) however are a much worse match for the experimental values. Overall, from these results we conclude that on both substrates 6T+6P forms a mixed crystalline film. While similar to the that of single-crystalline 6P [6, 236], its structure is significantly altered due to the presence of 6T. We attempted to refine the unit cell parameters of 6P to match the GIXRD data of the mixed film on HOPG following an indexation method developed recently [9–11]. This yielded a triclinic 6T+6P unit cell with the parameters given in table 5.1 juxtaposed with those of pristine 6P (in cell choice II) [6, 7]; see section 5.5 figure 5.12 for the reciprocal space map with the calculated reflections based on our refined 6T+6P unit cell. Most notably, the lattice spacings of the (00*l*) series calculated for the 6T+6P unit cell match very well the XRD data for the mixed film on SiO_x (e.g., the calculated (001) lattice spacing is 26.67 Å, the experimental value is 26.61 Å). This indicates the same mixed crystal structure to also grow on SiO_x despite the different texture plane [(001) on SiO_x, (−111) on HOPG].

The GIXRD data recorded for the film on SiO_x [figure 5.2(c)] does neither show well-defined Bragg peaks as it would be expected for a crystalline, fiber-textured film (2D

powder), nor Debye–Scherrer rings reminiscent of a crystalline non-textured adsorbate (3D powder). Instead, we observe elongated vertical diffraction features at q_{xy} positions which are indicative of the molecular herringbone arrangement of 6P (the most prominent being the $-11l$, $-20l$, $-21l$ series) [9], but no peaks in the out-of-plane direction. Such uncommon features are referred to as Bragg rods and are found in textured, crystalline monolayers due to the lack of out-of-plane periodicity [168, 171]. However, from our XRD data, owing to its strong and sharp diffraction features and pronounced Laue oscillations which allowed deducing the out-of-plane crystalline coherence length, we know that the film is certainly far thicker than a monolayer. Therefore, the occurrence of Bragg rods is indicative of a layered structure, where the individual layers show crystalline order only within the planes while the lateral position of the layers with respect to each other is arbitrary. Note that we have recently reported a similar growth mode for asymmetrically substituted 6P films on SiO_x with two fluorine substitutions at the meta position of the terminal ring [14]. Still, however, our 6T+6P unit cell refined for the film on HOPG matches well the experimental positions for the film on SiO_x , as illustrated in figure 5.2(c), which strongly supports that the same mixed structure grows on both substrates (with different texture planes). Overall, our structural analysis strongly suggests mixed crystal growth to occur for equimolar 6T+6P films in a crystal structure similar to that of pure 6P.

5.3.2 Fourier transform infrared spectroscopy (FTIR)

To spectroscopically investigate the mixed films and to gain information on the composition complementary to our diffraction data, we performed FTIR on the blend and correlated these data to that of the pure systems. Figure 5.3 shows FTIR spectra recorded on pure 6P, 6T and 6T+6P films as codeposited on SiO_x , the vibrational modes are labelled in accordance with previous studies [248–250]. The modes related to the out-of-plane $\gamma(\text{C}_\alpha\text{-H})$ end-ring vibration and $\gamma(\text{C}_p\text{-H})$ para-substituted ring vibration of 6P show a blue shift of 1.7 cm^{-1} and 1.0 cm^{-1} respectively, upon codeposition with 6T. Similarly, the $\gamma(\text{C}_\beta\text{-H})$ vibration of 6T shows a blue shift of 2.5 cm^{-1} in the codeposited 6P environment. The feature in the FTIR data of the codeposited film which is most relevant to our study is the vanishing of the Davydov split peaks, which are originally at 687.7 cm^{-1} and 701.2 cm^{-1} for pure 6T. Instead, a peak at 687.7 cm^{-1} appears in the codeposited film. As its width is significantly broader than the pure modes we interpret it as a superposition of two neighboring modes, the ring deformation $\delta(\text{C}_\alpha\text{-H})$ vibration of 6P (688.3 cm^{-1}) and the out-of-plane end-ring bending $\gamma(\text{C}_\alpha\text{-H})$ of 6T [244]. Importantly, the vanishing of Davydov split 6T peaks in the codeposited film is an indication of a change in the local environment of the 6T molecules due to the presence of 6P. Therefore, these data strongly support the notion of mixing on the molecular scale, and that no pure 6T phase precipitates in the mixed film. These results are in agreement with previous findings by Vogel et al. [112].

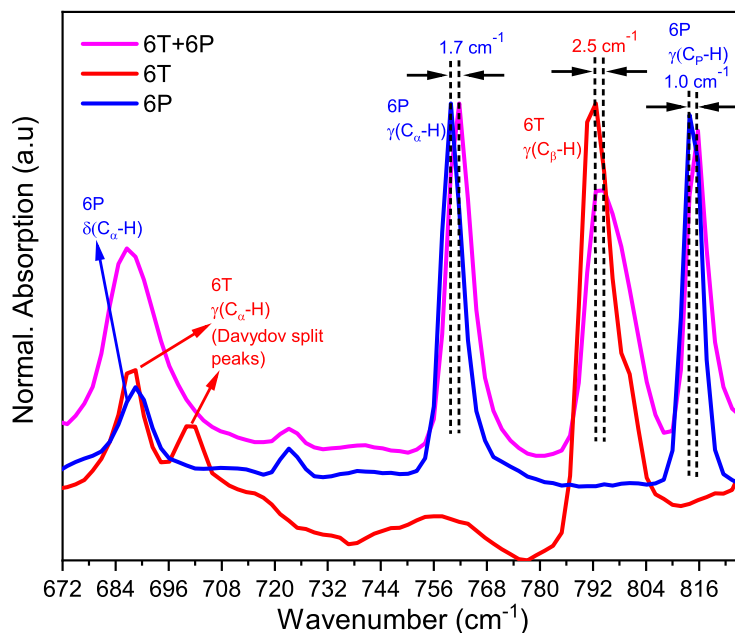


Figure 5.3: FTIR spectra of pure 6T (red curve), 6P (blue) and codeposited 6T+6P (magenta) films grown on SiO_x .

5.3.3 UV-vis/NIR spectroscopy

It is well established that blending organic semiconductors on the molecular scale can lead to gradual changes in the optical and electronic structure of the blend. Tuning the ionization energy of the mixed system is possible by changing the mixing ratio [251], which can be exploited to tune the open circuit voltage of organic solar cells [252]. Also, for rod-like organic semiconductors such as pentacene (PEN) and perfluoropentacene (PFP) it has been found that mixed crystal formation can translate into significantly altered optical properties of the blend. There, the emergence of a charge transfer absorption has been reported in blends of PEN and PFP [253, 254] which was promoted by a cofacial arrangement of the molecules in their crystalline structure [255–257] and led to effects like singlet exciton fission [258]. To investigate the optical properties of the 6T+6P blend we performed UV-vis/NIR spectroscopy on the mixed films and the pure films as reference, the results are shown in figure 5.4. Consistent with previous studies [259–261] pure 6P displays strong absorption in the range between 3–4 eV, with an absorption onset at 3.1 eV (blue curve in figure 5.4). The absorption in this region has been assigned to fundamental $\pi \rightarrow \pi^*$ transitions of 6P molecules with their long molecular axis oriented almost perpendicular to the substrate (referred to as ‘standing’ in the following). Likewise, the absorption spectrum of pure 6T (red curve in figure 5.4) shows the

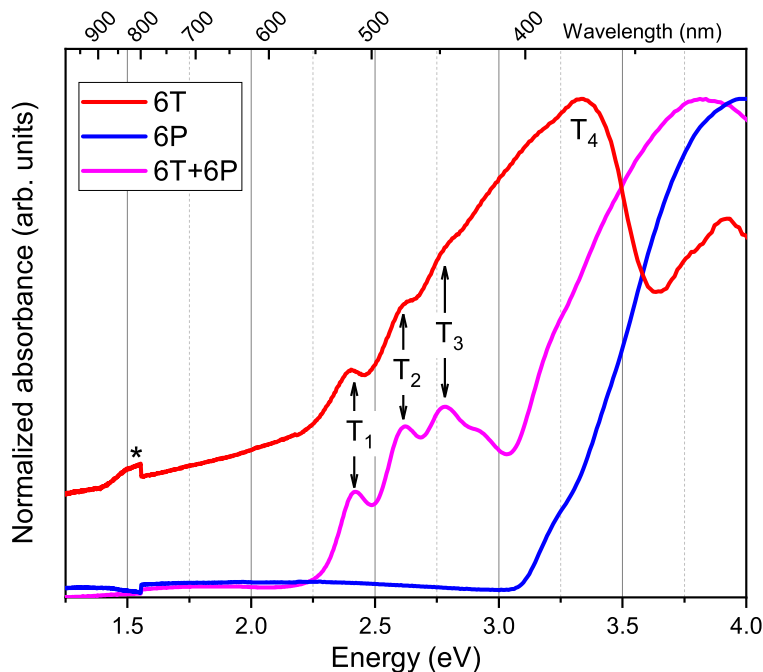


Figure 5.4: UV-vis/NIR spectra of pure 6T (red curve), pure 6P (blue), and codeposited 6T+6P (magenta) films on quartz; features discussed in the text are labelled.

known characteristics of 6T films with an absorption maximum around 3.4 eV (labelled as T_4) and weaker features around 2.4 eV, 2.6 eV and 2.8 eV (peaks labelled as $T_1 \dots T_3$) [262, 263]. The origin of these absorption features has been under debate in earlier papers on the opto-electronic properties of 6T [263–268]. It has been concluded that the fundamental $\pi \rightarrow \pi^*$ transition of 6T occurs from the symmetric 1^1A_g ground state to the asymmetric 1^1B_u excited state [269]. For 6T in solution [263] and if isolated in a polymer matrix [262] this transition (peak) is found around 2.8 eV and 2.4 eV, respectively, while in the condensed phase it is heavily *hypsochromically* shifted to 3.4 eV. This has been explained for 6T crystals by *Davydov splitting* of the 1^1B_u excited state with all oscillator strength on the higher energy level [262, 269] and a remarkable degree of Davydov splitting of ca. 1 eV [262, 270]. Note that like 6P, [6] 6T also grows in a herringbone crystal structure. It exhibits four molecules per unit cell, parallel long molecular axes, a planar all-trans configuration, and molecular planes between nearest neighbours inclined by 60° which can promote such a splitting [271]. Also, absorption of 6T is largely influenced by the order of the molecules in the film. In films of multilayer thickness (in the following referred to as ‘bulk’) on dielectric substrates the long molecular axis of 6T tends to grow standing on the substrate surface, however, with some film portion also adopting an orientation parallel to the surface (‘lying’) [272]. Notably, the growth on dielectric substrates such as SiO_x is increasingly complex as it depends strongly on preparation conditions whether polymorphism in thin films with the occurrence of a standing disordered phase together with crystalline 6T is found [265, 273, 274]. The absorption spectra

for 6T films have been found to depend on the film thickness where intensity in the low energy transitions has been ascribed to increasing disorder in the films, which breaks the selection rule and makes forbidden transitions partially allowed [175]. Thus, although the transition to the lower Davydov band is expected to carry no oscillator strength, such an absorption around 2.4 eV (labelled T_1 in our data in figure 5.4) has been observed in thin films correlating with our observations [262]. The energy separation of ca. 0.2 eV between the peaks T_1 , T_2 and T_3 is close to the energy of the C=C stretching mode (0.18 eV) [266, 275–277] suggesting that T_2 and T_3 are then vibronic progressions of T_1 [265, 278]. The pronounced absorption background in the spectrum of 6T below the fundamental transition can be explained by *Mie scattering* which comes into play when the crystallite size in a polycrystalline structure is in the range of the incident wavelength. Note that the marked dominance of T_4 has also been discussed as H-aggregation in condensed 6T, that is, exciton coupling between molecules having parallel transition dipoles [175, 263, 265, 276].

We now turn our attention to the absorption of the equimolarly mixed 6T+6P film (magenta curve in figure 5.4). Here, we observe a marked difference to the spectra of the pure films: features T_1 , T_2 and T_3 now become dominant in the spectrum, while the formally strongest 6T transition T_4 is no longer detected. As we know from our FTIR data, Davydov splitting of 6T does not prevail in the 1:1 blend indicating the formation of a mixed crystal structure (*vide supra*), which is also strongly suggested by our structural analysis, absorption peaks $T_1 \dots T_3$ cannot stem from transitions into the lower Davydov band. As they occur at the same energies as in the pure film, we rather ascribe these peaks to transitions of the isolated molecules, possibly with some extent of J-aggregation in the blend (see also our PL data below), as T_1 is found redshifted as compared to 6T in a PET matrix [262].

5.3.4 Photoluminescence spectroscopy (PL)

To finally explore whether green emission reported for monolayers of 6T prevails in the mixed crystal structure, we performed photoluminescence spectroscopy on pure 6P, bulk 6T and the 1:1 codeposited 6T+6P film on the various substrates. Figure 5.5 shows PL spectra of the films on SiO_x using an excitation wavelength of 315 nm (3.95 eV) and 373 nm (3.33 eV) for pure 6P and 6T, respectively, and of 325 nm (3.82 eV) for the 6T+6P film, which is, thus, well above the 6T absorption region. Note that due to the substantial spectral overlap between 6P emission and 6T absorption and their mixing on the molecular scale emission from the codeposited film is expected to comprise sensitized emission from 6T due to *RET* [8]. This is promoted by the fact that the transition dipole moments of both 6T and 6P are oriented along the molecular long axes [105, 236, 262, 279] and, thus, lie essentially parallel in the 6T+6P blend based on the structure we determined (see table 5.1 and figure 5.7 below).

The emission spectrum of 6T (red curve in figure 5.5) shows poorly resolved peaks which can be deconvoluted into four peaks using the Voigt function (figure 5.9) centered around 2.38 eV, 2.26 eV (0–0), 2.1 eV (0–1) and 1.94 eV (0–2). The energy separation of 0.16 eV between the latter three (in the range of the C=C stretching energy) indicates

that they are the vibronic progressions of the same electronic transition. However, the peak at 2.38 eV does not fit into this series and must be of different origin. Its position is close to the reported value of the fundamental emission peak observed for a flat-lying sub-monolayer of 6T on SiO_x (2.3 eV) [272, 277], where growth of a 6T monolayer between 6T bulk islands may give rise to this emission feature on SiO_x . The fact that this peak is absent on the quartz substrate while the vibronic peaks are still observed (figure 5.9) supports this view, as quartz has a higher surface roughness and is thus expected to induce more three-dimensional growth. Alternatively, as 6T has been found to exhibit polymorphic growth on SiO_x [265, 273, 274] we cannot fully exclude that transition to be the fundamental transition shifted due to the different packing. The other three peaks at lower energy and their intensity distribution are well in line with those found in a 6T single crystal with the dominating 0–1 emission peak indicating H-aggregate formation [272, 277].

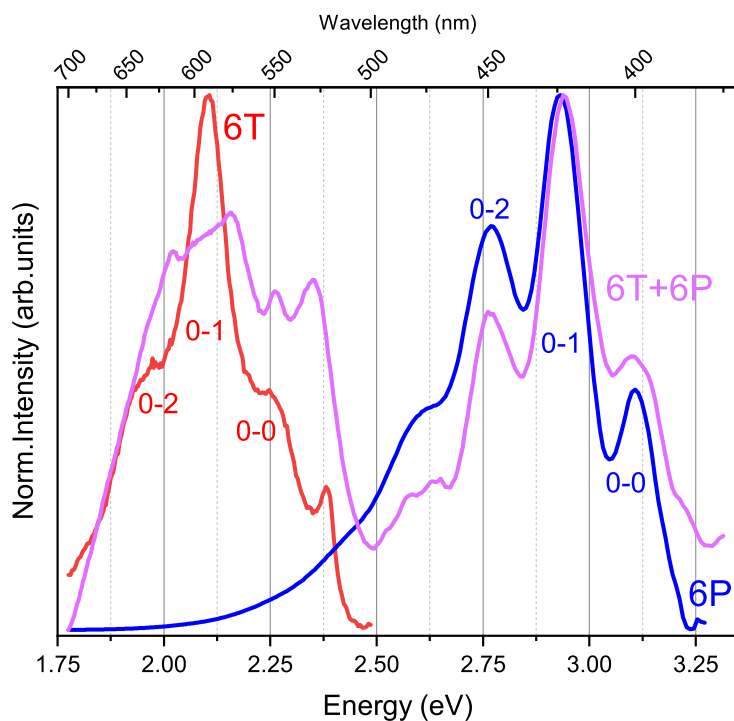


Figure 5.5: Photoluminescence spectra from pure 6T (red curve), 6P (blue) and codeposited 6T+6P (magenta) films on SiO_x . For better comparison, PL emission of pure 6T and the codeposited and 6P film has been normalized to 0-1 emission peak of pure 6P.

The emission spectrum of 6P (blue curve in figure 5.5) shows well resolved peaks around 3.11 eV (0–0), 2.93 eV (0–1) (dominant peak), 2.76 eV (0–2) and another weaker feature around 2.58 eV (0–3). They are separated by 0.18 eV and can be well fitted by Voigt functions (figure 5.10). Note that the emission spectrum of 6P on quartz is very similar but shows no resolved vibronic features, likely due to disorder.

Due to the growth of a mixed crystal structure of 6T+6P the PL spectra of the codeposited films are no simple superposition of the pure film spectra. Rather, several ob-

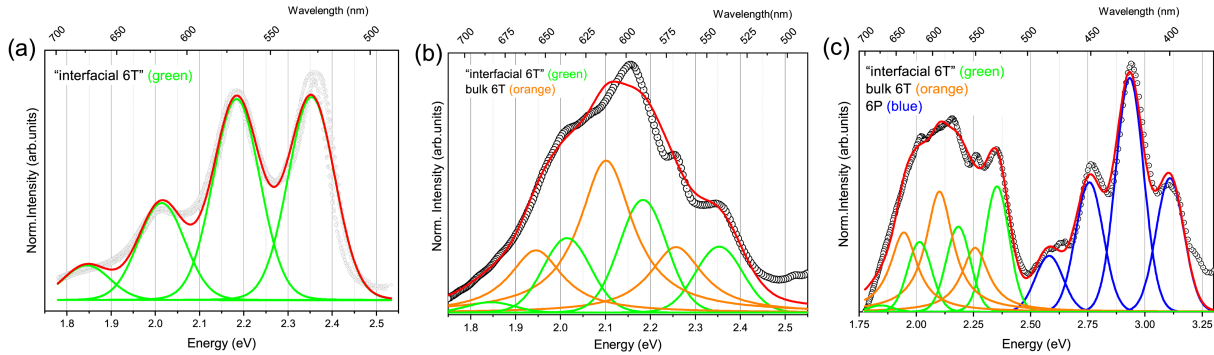


Figure 5.6: (a) PL data for ‘interfacial 6T’ extracted from Ref. [8] and fitted with four Voigt functions (green curves). (b) Corresponding PL data recorded for the 6T+6P film on HOPG; data is fitted with ‘interfacial 6T’ peaks [positions taken from (a)] and bulk 6T peaks (orange curves). (c) PL data recorded for the 6T+6P film on SiO_x again fitted with the peaks from ‘interfacial 6T’, bulk 6T, and with peaks assigned to 6P (blue curves); the fits of the pure spectra (bulk 6T, 6P) are provided as figures 5.9 and 5.10 in the section 5.5; peak positions are provided in tables 5.4 and 5.5.

served peak positions resemble those reported for lying monolayers of 6T sandwiched between 6P layers on muscovite mica and HOPG. There, 6T– in the following referred to as ‘interfacial 6T’ in accordance with literature [8, 107, 108, 280]– showed green instead of the red emission which is characteristic for the 6T bulk crystal structure; literature data taken from ref. [8] is shown and fitted in figure 5.6(a) [8, 107–109]. We note that the time evolution of the green emission from ‘interfacial 6T’ has been investigated in detail in Ref. [8], where the authors deduced non-radiative energy transfer between 6P and 6T. As it is apparent in figure 5.6(b) and 5.6(c) for our codeposited films on HOPG and SiO_x , respectively, the observed peak positions for the 6T related emission features can be well explained by ‘interfacial 6T’ (green curves) together with some contribution from bulk 6T (orange curve). We note that while the 6T related emission peaks on HOPG (i.e., in lying orientation) are perfectly aligned with those on the other two substrates, 6P emission is weaker there and the peaks appear slightly shifted (see figure 5.11 for full spectra). All PL spectra of the codeposited films have been fitted using the same peak parameters (number, position, and width) as determined for the pure films, the data for ‘interfacial 6T’ has been taken from Ref. [8].

It has been suggested by Loi et al. and Da Como et al. for the lying sub-monolayer of 6T on SiO_x that the PL has J-aggregate character [272, 277], which is in agreement with the findings for ‘interfacial 6T’ [107]. Note that charge transfer in the ground state between the species can be excluded on the basis of previous photoemission results [8]. Therefore, we regard our PL data as indication for J-aggregation of 6T in the co-crystalline 6T+6P blend as well, which entails end-to-end alignment of neighbouring 6T molecules in the mixed crystal structure. Our tentative structure solution based on GIXRD revealed a unit cell volume capable of hosting two molecules, the length of the c -axis of 2.89 nm is essentially equal to the *van der Waals* length of 6P. Therefore, it can be expected that the molecules are not (much) inclined with respect to this axis and, thus, a 6T orientation

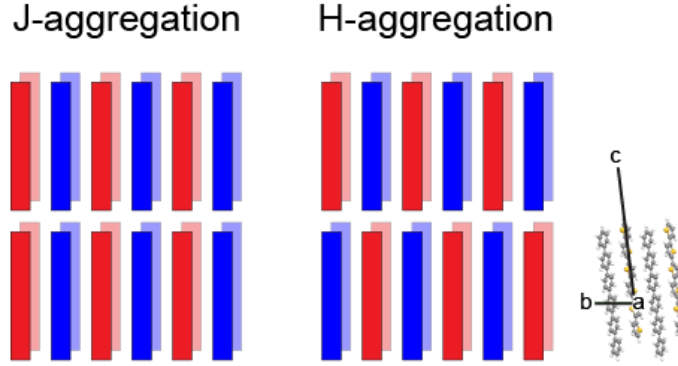


Figure 5.7: Sketch of the two extreme cases of interlayer arrangement that can occur for 6T+6P films on SiO_x together with the crystallographic unit cell suggested for the mixed structure and the proposed orientation of the molecules within the unit cell (the angle between the long molecular axes of 6P and 6T is smaller than 1°); the calculated GIXRD intensities for this tentative structure solution are shown together with the reciprocal space map of 6T+6P on HOPG in the section 5.5 figure 5.12.

suitable for J-aggregation is likely in the mixed crystal structure, which explains the green emission. Our attempts to model the 6T+6P mixed crystal structure yields a structure of herringbone type with essentially parallel molecular long axes, calculated diffraction intensities match well the experimental ones (figure 5.12); this tentative structure solution is depicted in figure 5.7. This allows us to determine the angles between the molecular long axes and the respective texture planes of the films on HOPG and SiO_x [(-111) and (001), respectively], which are $< 1^\circ$ for HOPG ('lying orientation') and 74.7° for SiO_x ('standing orientation'). We now recall the GIXRD data on SiO_x where Bragg rods have been observed despite multilayer film thickness in the fibre-textured film, which indicates a structure which is crystalline within the layers (i.e., the crystallographic ab -plane) but in which the lateral position of the layers is arbitrary. For such a structure, in the statistical average, significant end-to-end alignment of 6T molecules is therefore expected, at least for half of the 6T molecules if the layers were indeed completely uncorrelated with each other. In addition, however, the PL spectra also show a contribution similar to the emission found for the 6T single crystals ('bulk 6T'). There, H-aggregation occurs due to side-by-side stacked molecules in the 6T herringbone structure. On the basis of our GIXRD data on SiO_x we can conclude from the occurrence of the three strong q_z -rods between 1.3 \AA^{-1} and 2.0 \AA^{-1} a structure of herringbone type (as it is found for both pristine materials as well) to prevail also in the mixed system. Therefore, H-aggregation of 6T can, in principle, occur also in the mixed film and dominate for those 6T molecules in the structure that are not suitable for J-aggregation. Note that systems showing both H- and J-aggregation and the prerequisites thereof have been discussed in great detail recently by Kreger et al. [281], Hestand and Spano [134], Yamagata et al. [282], and Eder et al. [283], the latter demonstrating the possibility of reversible switching between H- and J-aggregation. Alternatively, the precipitation of bulk 6T cannot be entirely excluded, if too little to be detected by our X-ray diffraction experiments, and if of too low concentration to be observed in FTIR. We regard this, however, as very unlikely given its expected

significant contribution to the PL. Clearly, fully understanding the photophysics of the present system would require growing a mixed 6T+6P single crystal of sufficient size to perform both PL and single-crystal X-ray diffraction to precisely determine its crystal structure.

5.4 Conclusions

We have detailed the structural and optical properties of equimolar vacuum codeposited films of the organic semiconductors 6T and 6P in order to assess how the optical properties of the individual species translate into a solid-state blend. From the disappearance of the characteristic Davydov splitting found in pristine, crystalline 6T, intimate molecular-level mixing could be concluded. Structural analysis by specular X-ray diffraction and GIXRD corroborated this finding and pointed towards mixed crystal structure formation both in lying (on HOPG) and standing (on SiO_x) molecular orientation. The unit cell parameters deduced from GIXRD yielded a unit cell volume capable of hosting two molecules, which allowed us to conclude on the molecular orientation in the film to be of herringbone type. For the standing film on SiO_x the occurrence of Bragg rods reveals that this crystalline order prevails in the layered mixed film, but that the layers are non-correlated with each other. The photoluminescence of the mixed films showed green emission in addition to the characteristic red and blue emission known for pure 6T and 6P, irrespective of the substrate. These observations can be explained by contributions of J- and H-type aggregation of 6T, which is supported by our absorption spectroscopy results of the mixed films as well as by the structural film properties deduced from X-ray diffraction. Our study thus shows that the remarkable optical properties of 6T/6P heterostacks translate well into the mixed phase of this material pair and, once more, that tuning the opto-electronic properties of organic semiconductors through establishing blends of functional materials is a promising pathway to achieve altered material properties.

5.5 Supplementary Data

The data presented in this section has been published as supporting information for the manuscript [17] on which this chapter is based on.

5.5.1 Additional experimental information

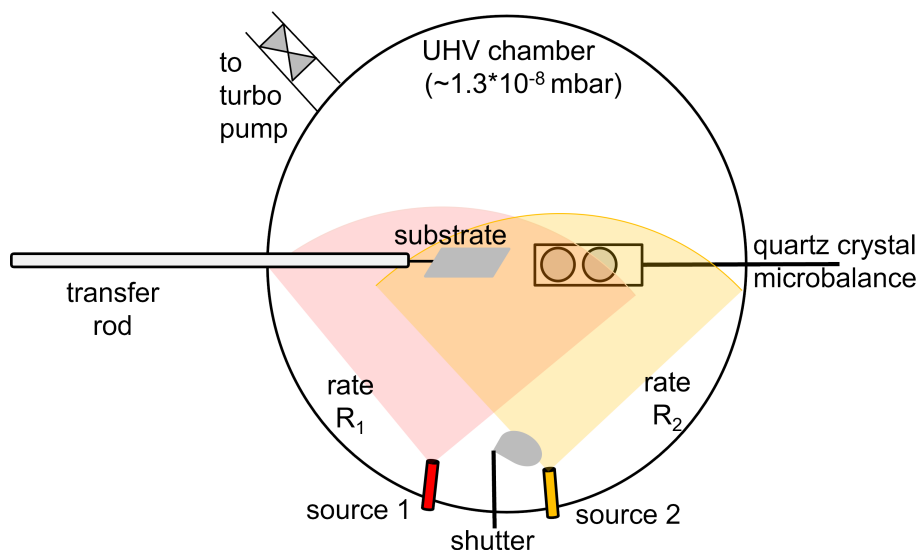


Figure 5.8: Illustration of co-deposition by physical vapour deposition in ultra-high vacuum (UHV) chamber.

5.5.2 Additional experimental data

5.5.2.1 FTIR peak positions

	$\gamma(\text{C}_\alpha - \text{H})_{6\text{T}}$	$\gamma(\text{C}_\beta - \text{H})_{6\text{T}}$	$\delta(\text{C}_\alpha - \text{H})_{6\text{P}}$	$\gamma(\text{C}_\alpha - \text{H})_{6\text{P}}$	$\gamma(\text{C}_\text{P} - \text{H})_{6\text{P}}$
6P	-	-	688.3	760.1	814.6
6T + 6P	687.7	795.5	686.5	761.8	815.6
6T	687.7, 701.2	793.0	-	-	-

Table 5.2: Comparison between fundamental vibration peaks of 6P and 6T (values in cm^{-1}).

5.5.2.2 Additional Photoluminescence Spectroscopy Data

Using the intensity ratios of the vibronic transitions we can calculate Huang-Rhys factor S . For a rigid molecule that does not undergo conformational changes upon excitation, S is around 1 and the emission is dominated by 0-0 vibronic transition. This is also reflected by zero Stokes shift between the absorption and emission maxima. Instead, for a flexible species S is higher than 1 and the emission is dominated by higher vibrational levels instead, as in the present case. As calculated in Table 5.3, value of S for 6P varied from 2.96 (in pure film) to 2.53 (in the codeposited film) and for 6T the value changed from 2.75 (in pure film) to 2.39 (in the codeposited film) indicating not much change in the geometry due to codeposition.

		Pure film	Codeposited film	S_P	S_C
6P	$(0-1)/(0-0)$	2.22	1.93	2.96	2.53
	$(0-2)/(0-1)$	0.74	0.60		
6T	$(0-1)/(0-0)$	2.28	1.69	2.75	2.39
	$(0-2)/(0-1)$	0.47	0.70		

Table 5.3: Summary of intensity ratios of $(0-1)/(0-0)$ and $(0-2)/(0-1)$ peaks in pure 6P, 6T and codeposited films on SiO_x , and the Huang-Rhys factors (S) calculated for the different pure (S_P) and codeposited (S_C) films.

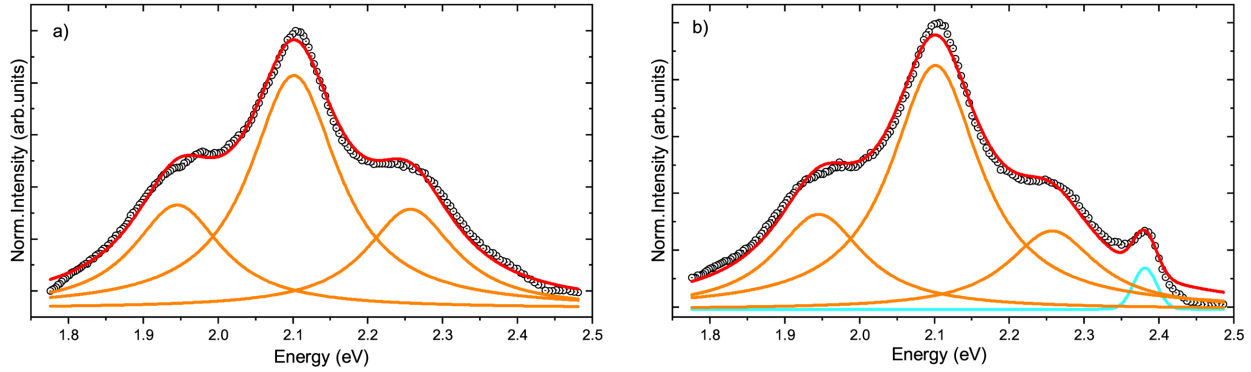


Figure 5.9: Fitted PL spectra of (a) 6T on quartz and (b) on SiO_x ; peaks fitted using Voigt functions.

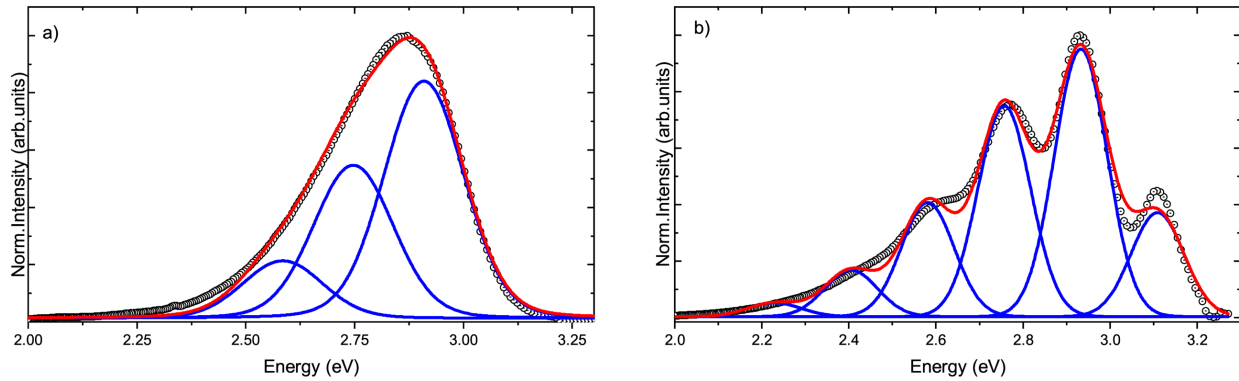


Figure 5.10: Fitted PL spectra of (a) 6P on quartz and (b) on SiO_x ; peaks fitted using Voigt functions.

	Absorption (eV)	Emission (quartz) (eV)	Emission (silicon oxide) (eV)	Emission (HOPG)(eV)
6T + 6P	-	-	2.94	2.16
6P	3.97	2.87	2.93	-
Bulk 6T	3.34	2.11	2.11	-

Table 5.4: Absorption and emission maxima for pure 6P, 6T and codeposited film.

	0-0	0-1	0-2	0-3	0-4	0-5
6P	3.109	2.933	2.757	2.581	2.405	2.229
Interfacial 6T	2.353	2.184	2.014	1.845	-	-
Bulk 6T	2.257	2.101	1.945	-	-	-

Table 5.5: Summary of deconvoluted peak position for 6P and 6T (interfacial and bulk) films deposited on Si substrate (values in eV).

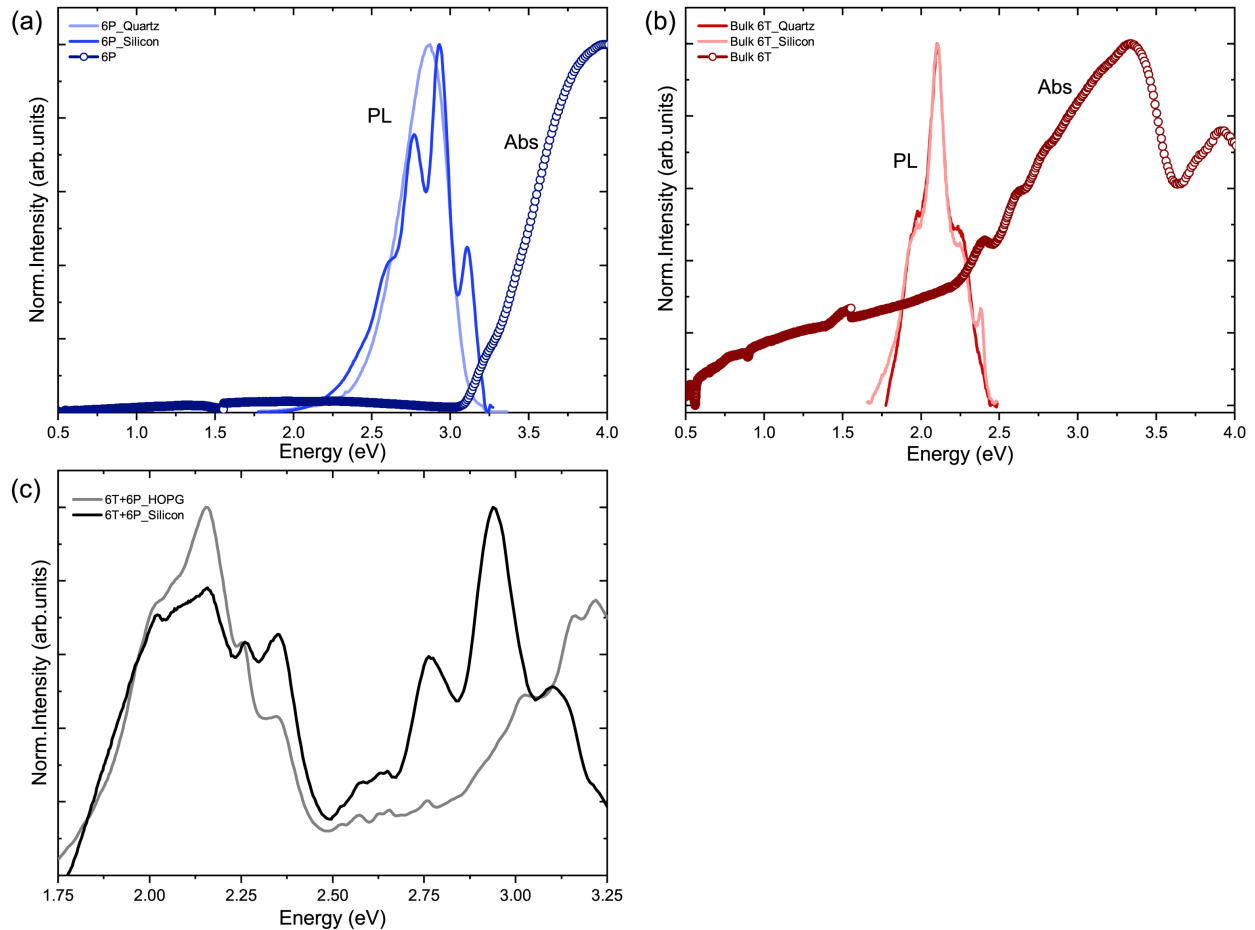


Figure 5.11: Comparison of absorption and emission spectra of (a) pure 6P, (b) pure 6T on quartz and SiO_x substrates, and (c) of the PL data recorded for codeposited 6T+6P films on SiO_x (black curve) and HOPG (grey curve) as substrate; see also figure 5.6 of the main text.

5.5.3 Structure Modelling

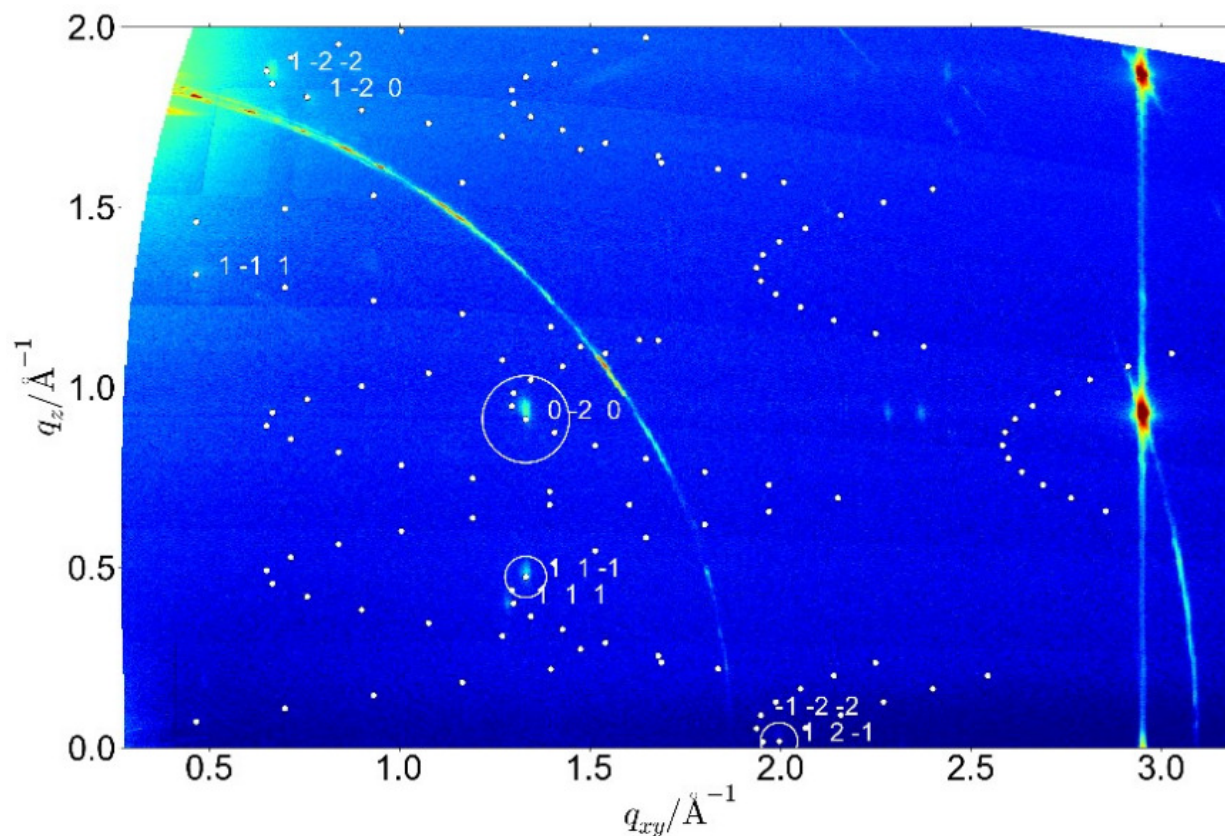


Figure 5.12: Reciprocal space map obtained by GIXRD on the 6T+6P film grown on HOPG showing the experimental data together with calculated reflections [(-111) texture] of the refined unit cell with parameters $a=5.696\text{\AA}$, $b=7.836\text{\AA}$, $c=26.888\text{\AA}$, $\alpha=83.62^\circ$, $\beta=86.42^\circ$, $\gamma=89.44^\circ$ (cf. table 5.1 in the main text). The map shows the indices which have been used for the unit cell determination following an indexation method developed recently [9–11]. Circle diameters correspond to intensities calculated for a tentative model structure comprising one molecule of each species in the unit cell (see illustration of the structure in figure 5.7 of the main text).

Chapter 6

Ongoing and Future Research Directions

The data presented in this chapter extend beyond and complements the primary findings of the thesis by providing insights into related studies on p-doping of OSC with molecular dopants such as FxTCNQs and Lewis acids.

In addition to my research on the tuning of the microstructure of P3HT films to enable exploring the role of microstructure in CTC versus IPA formation upon molecular doping, I have conducted extensive experiments on doping linear hexylated oligothiophenes (HxTs) and other thiophene-based molecules such as a series of benzothieno[3,2-b][1]benzothiophene derivatives (BTBTx) with FxTCNQ as molecular p-dopants. Additionally, I have investigated the doping of the prototypical conjugated polymer P3HT with a range of Lewis acids of different Lewis acids and electron affinities. The skeletal structures of all materials used in this section are shown in Appendix A in figures A.2 and A.3. While these studies are not yet sufficiently comprehensive to be immediately publishable, they allow drawing crucial conclusions and will be subject to upcoming manuscripts which I am planning to compose.

6.1 p-Doping of Oligothiophenes with F4CTNQ

Oligothiophenes with hexylated sidechains can serve as model systems for probing the conjugation length as parameter in the doping mechanisms of P3HT. This is possible because, in contrast to the conjugated polymer, their conjugation lengths are exceedingly well defined. In this study, alkylated rather than non-alkylated oligomers were chosen because, while the latter are capable of forming highly crystalline films when deposited by vacuum sublimation, they are generally insoluble in most organic solvents [271, 284–287].

In a previous study on crystalline films of the OSC α -quaterthiophene (4T) it was shown that blending the OSC with a planar, strong electron acceptor like F4TCNQ promotes CTC formation [90]. Conversely, for P3HT exposed to F4TCNQ, IPA and CTC formation has been found to co-exist depending on the processing conditions [80, 288].

In a recent manuscript from our group published by Liu et al. [12] and the PhD thesis by Hannes Hase [13] it was further demonstrated that on blending HxTs ($x = 4, 6,$

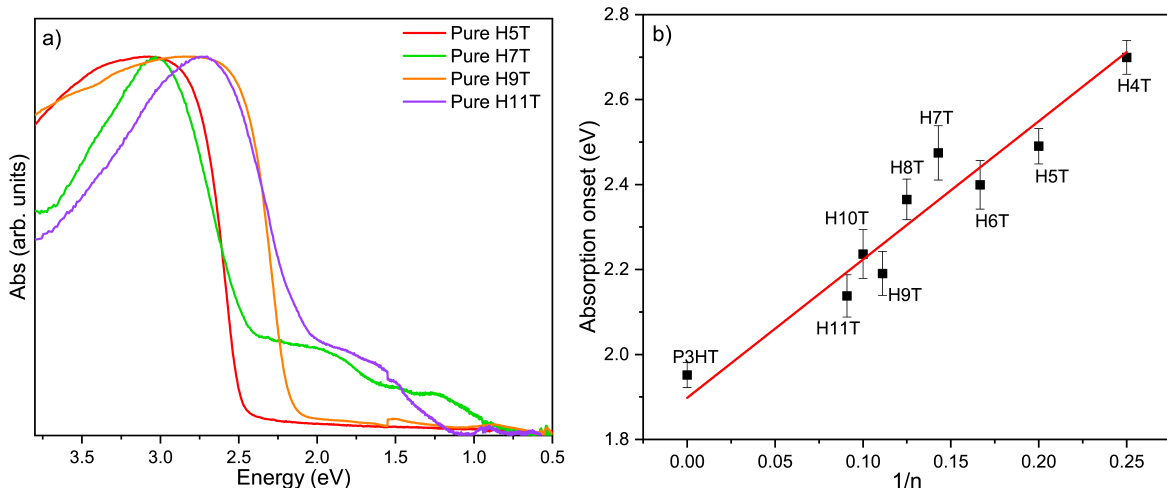


Figure 6.1: (a) UV-vis/NIR spectra of pristine H_xTs ($x= 5, 7, 9, 11$) films, (b) a plot of extrapolated absorption onset versus $1/n$ where n is the number of thiophene repeat units. The absorption onset values of H4T, H6T, H8T and H10T are taken from Ref. [12, 13] for comparison.

8, 10) with F4TCNQ, the shorter H_xTs ($x= 4, 6, 8$) primarily exhibited CTC formation. However, additional IPA formation was observed with H10T–F4TCNQ, thus marking the onset of the transition from CTC into an ICT regime. In comparison to H8T, H10T was found to be more conducive to forming IPA, despite the similar IE values of ~ 5.39 eV for these two oligothiophenes [13]. It was hypothesized that this difference can be attributed to the ability of H10T to form distinct side-chain regions, akin to those observed in P3HT. These regions could effectively accommodate F4TCNQ^{•-}, thereby acting as a spacer towards the thiophene π -electron cloud, hence, providing a more favourable electrostatic environment for IPA formation [13, 93, 289, 290]. However, applying this idea to H10T–F4CTNQ was based on a series of H_xTs with an *even* number of thiophene repeat units, each having *two non-hexylated thiophene units* in the center. In this study, we aim to extend these considerations by investigating H_xTs with *odd*-numbered repeat thiophene units, which feature *a single non-hexylated thiophene unit* in the center (refer to figures A.2 in Appendix A for chemical structure). For IPAs in F4TCNQ doped P3HT, F4TCNQ^{•-} have been reported to be intercalated within the alkyl-sidechains of P3HT [98, 154, 291–293]. Therefore, it is plausible that differences in the number of non-hexylated thiophene units, lead to distinct host–dopant arrangements in doped H_xTs, potentially resulting in different doping behaviors. Also, it was hypothesized by Hase et al., [13] that the density of side chains may influence the doping mechanism in conjugated polymers and oligomers.

The goals of this study are twofold: (1) to elucidate the role of the parameters– hexyl side chain density and conjugation length– in the doping mechanisms of organic semiconductors, and (2) to bridge the gap between existing data on even-numbered H_xTs, as reported in prior work [12, 13], i.e., explore if pure IPA formation occurs beyond the limit of 10 repeat units as observed by Liu et al. [12]. H8T, despite having an IE comparable to H10T, still primarily exhibits CTC formation, while H10T shows IPA and CTC formation. Thus, H9T serves as an important case study, as its IE is expected to lie in the range of

H8T and H10T but it has the same number of hexyl side chains as H10T does. Therefore, comparing the doping phenomenology of H9T with that of H8T and H10T can potentially offer valuable insights into the transition between the two regimes, CTC versus IPA, as a function of conjugation length and side chain density [13]. Preliminary results from this study are discussed below.

Figure 6.1(a) shows the UV-vis/NIR spectra of pristine H5T, H7T, H9T, and H11T films. As expected, the energy of the fundamental HOMO-LUMO transition decreases with increasing oligomer chain length, as indicated by the red-shifted absorption onsets [294–297]. Figure 6.1(b) presents the absorption onset values of H_xTs (x = 4 to 11) as a function of the inverse number of thiophene repeat units (1/n), combining data from the present study with previously published results for H4T, H6T, H8T, and H10T [12, 13]. The observed linear dependence is consistent with previous findings [12, 297] indicating that all H_xTs (x = 4 to 11) are essentially planar in the solid state without an interruption in conjugation (as reported before for 6T by Horowitz et al. [271]). The UV-vis/NIR

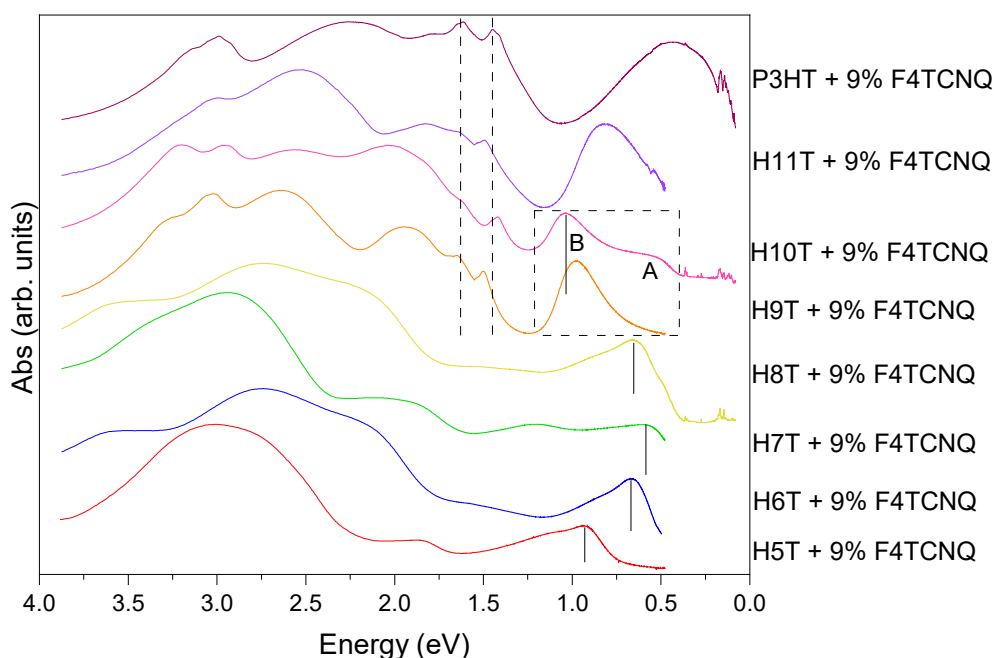


Figure 6.2: UV-vis/NIR spectra of thin-film of H_xTs (x = 5 to 11) and P3HT upon doping with F4TCNQ at a dopant molar ratio of 9% per thiophene-ring; the vertical lines mark the peak positions assigned to the HOMO-LUMO transition of the CTC in doped H_xTs (x= 5 to 8). The dashed lines mark the position of peaks characteristic to F4TCNQ^{•-}. In ref. [12, 13] peaks ‘A’ and ‘B’ are interpreted as indicators of H10T^{•+} (labeled as B) and the CTC related transition in H10T-F4TCNQ (A), respectively.

The optical absorption spectra of doped H6T, H8T, H10T and P3HT were taken from ref. [12, 13] for comparison.

spectra of H_xTs (x = 5 to 11) doped with F4TCNQ are shown in figure 6.2 together with

the P3HT polymer limit. As evident in figure 6.2, upon doping with F4TCNQ, H5T and H7T exhibit sub-gap absorption bands at approximately 0.93 eV and 0.60 eV, respectively. These values align very well with the bathochromic shift observed in CTC transitions for H4T, H6T, and H8T which appear at 0.89 eV, 0.66 eV, and 0.66 eV, respectively [12, 13]. Overall, this bathochromic shift in CTC transitions with increasing conjugation length is in-line with the theoretical predictions [298] and tendencies reported for F4TCNQ-doped *even*-numbered H_xTs (x= 4, 6, 8) [12, 13]. Shifting focus to optical absorption spectra of H9T-F4TCNQ, shown in figure 6.2, it can be seen that upon doping with F4TCNQ, sharp peaks appear around 1.49/1.64 eV, which are characteristic for the F4TCNQ^{•-} [299, 300]. The position of these peaks agrees with those observed in P3HT-F4TCNQ systems (top curve in figure 6.2(b)) [13, 299, 300] where the formation of a dopant radical anion is confirmed. Furthermore, a peak denoted as ‘B’ and marked by a solid line in figure 6.2 appears slightly red-shifted for H9T-F4TCNQ (0.97 eV) as compared to H10T-F4TCNQ (1.03 eV). Previous studies on tridodecyl nonithiophene [296] and H10T [13] have suggested potential assignments for this peak, ranging from H_xT^{•+} absorption to CTC transitions. Additionally, based on the characteristic F4TCNQ^{•-} peaks ~1.49/1.64 eV, in H9T-F4TCNQ, we can deduce that this host-dopant pair does show signs of IPA formation, like the case of H10T in ref. [12], where the process of integer charge transfer between dopant and OSC requires the formation of a radical cation formed in the latter as well. Therefore, in line with the interpretation put forward for ‘B’ in the H10T case [12], this absorption could be assigned to H9T^{•+}. However, for the H10T case, the lower energy transition labeled as ‘A’ was assigned to a CTC transition and such a transition is not observed here for the H9T case, interpreting ‘B’ as CTC transition would, in turn, largely contradict the trend found for the whole series of increasing chain length and would require a significantly larger intermolecular coupling in the CTC. Therefore, based on the present data we cannot yet confirm if CTC formation also occurs as a weak CTC transition may be masked by it. A definitive interpretation of peak ‘B’ therefore will require further investigation, including vibrational spectroscopy (FTIR), to observe a possible low energy polaron transition [301] and molecular vibrations indicative of radical cation formation, and UV-vis/NIR spectroscopy in various solution where CTC formation is less likely. The absorption spectra of H11T-F4TCNQ are shown in figure 6.2, which alike H9T-F4TCNQ also shows the characteristic peaks assigned to F4TCNQ^{•-} at ~1.49/1.64 eV. From the current study on doping *odd*-numbered oligothiophenes with F4TCNQ we can, however, safely infer that the threshold for first observing IPA formation lies already at H9T. Above discussion about the nature of transition ‘B’ benefits from the investigation of the yet longest available oligomer H11T, where, again a equally strong sub-gap absorption is observed at an energy again far off the expected trend fro CTC formation. The fact that CTC formation seems less likely for the even lower IE oligomer and the increase in peak width of peak B from H9T, over H11T to P3HT points towards this transition to correspond to the radical cation (often referred to as polaronic transition P2 in pertinent literature [301]). This suggests that H11T as a longer oligomer analogue closer to P3HT shows a doping phenomenology closer to that of the polymer limit. We expect that the planned FTIR and solution UV-vis/NIR spectroscopy experiments on even longer thiophene oligomers such as H12T and H13T (synthesis attempted in the Forgione research group at Concordia) will serve to finally

resolve this open question. Additionally, the viscous state found for the whole HxT series may serve, in particular, for the case of H11T, as an important reference to understand the doping of (intrinsically semi-crystalline) P3HT, where I demonstrated that in-vacuo electrospray deposition allows preparing amorphous films (see chapter 5). Overall, while the present comprehensive body of data allows already drawing some conclusions on the doping phenomenology of the oligo- to polymer transition, the above mentioned experiments will be required to finally converge towards a publishable manuscript without need of speculation in the data interpretation; the publication of this work is planned for 2025.

6.2 p-Doping of BTBT Derivatives with Molecular Dopants

Donor materials <i>Acronym</i>	Ionisation energy(eV)	Acceptor materials	Electron affinity (eV)
BTBT-(C ₁₀ H ₂₁) ₂ <i>BTBT1</i>	5.65	TCNQ	4.69
BTBT-(C(CH ₃) ₃) ₂ <i>BTBT2</i>	5.67	FTCNQ	4.81
BTBT-(O-Ph) ₂ <i>BTBT3</i>	5.68	F2TCNQ	5.02
BTBT-(O-C ₈ H ₁₇) ₂ <i>BTBT4</i>	5.26	F4TCNQ	5.13
BTBT-(O-CH ₃) ₄ <i>BTBT5</i>	5.26		
BTBT-(CO-C ₇ H ₁₅) <i>BTBT6</i>	6.19		
BTBT-(C ₆ F ₁₃) ₂ <i>BTBT7</i>	6.50		
BTBT-(NH ₂) ₂ <i>BTBT8</i>	4.74		
BTBT-(NO ₂) ₂ <i>BTBT9</i>	6.86		

Table 6.1: DFT calculated values for the ionisation energy of the donor and the electron affinity of the acceptor materials.

While in the previous sub-section decrease in IE was achieved by increasing the length of the conjugated backbone of an oligomeric OSC, the IE of small conjugated molecules can equally be modified by adding electron withdrawing or donating groups to its conjugated core. This has been done on the prototypical OSC benzothieno[3,2-b][1]benzothiophene (BTBT), the chemical structure of the parent species and a library of investigated derivatives is depicted in figure A.2. This work represents a collaboration with the research groups of Dr. Yves Geerts (Universté Libre de Bruxelles, ULB, Belgium) and that of Dr. Norbert Koch, (Humboldt University Berlin, HUB, Germany); I

contributed to the investigations on the most interesting system BTBT-(NH₂)₂ (referred to as BTBT8 in the following) to this work, which is planned to be published with me as the first author in 2025. In this preliminary study, mixed films of BTBT1–5 with TCNQ derivatives have been investigated by UV-vis/NIR and FTIR spectroscopy to assess CTC versus IPA formation, as well as by GIXRD*, in order to find intermixture on the molecular scale (as required for CTC formation) versus phase separation. In UV-vis/NIR spectroscopy, the systems depicted in figure 6.3 a–f show new transitions in the fundamental gap of the pristine materials. In analogy to the discussion in the previous sub-section, the transitions, here labeled as ‘T1’ and ‘T2’ (in accordance to the time-dependent DFT calculations for the complex BTBT1:F4TCNQ as shown before [302]) are assigned to be related to the CTC; note that these transition energies are not dependent on the concentration. The general trend of decreasing transition energy for increasing EA of the dopant (from TCNQ to F4TCNQ) is observed for all of the BTBT derivatives (BTBT1-5). A similar trend is found for decreasing IE of the OSCs (from BTBT1+2+3 to BTBT4+5), find the IE/EA values (as determined by DFT calculations at ULB) and nomenclature for the BTBT derivatives in Table 6.1. The optical absorption of the CTC is clearly modified by the EA of the dopant and by the IE of the semiconductor, where the transitions T1 and T2 are found at lower energies for lower values of IE-EA.

However, for the sole case of BTBT8 with an IE well in the range of the dopant EA series, the phenomenology for blends with F4TCNQ is strikingly distinct to the other cases, both in UV-vis/NIR and FTIR. While the CTC transition energies for the BTBT8 blends follow well the expected trend for the blends with TCNQ, F2TCNQ and F4TCNQ, the structure of absorption spectrum of the BTBT8:F4TCNQ blend film differs significantly (gray curve in figure 6.3(f)). There, four absorptions are now observed which, however, do not correspond to the transition energies of F4TCNQ^{•-} (see figure 6.2), neither in position nor peak shape. If interpreted as CTC related, the transition found at lowest energy does not follow the expected trend of smaller CTC transition energy with higher dopant EA but is found at slightly higher energy than for F2TCNQ. In the same vein, the transition T2 is not clearly visible but would be expected in the range of the three higher energy transitions. Note that the structure of the absorption spectra is also similar for measurements in the temperature range from room temperature down to 77 K (experiments performed at HUB, Germany).

The present data allows the following interpretation, which is informed by the body of knowledge on the charge transfer behavior of BTBT1 in the work by Mendez et al. [302]. If charged molecules were present, their transition energies would be constant, transitions due to the BTBT radical cation alongside those of the F_xTCNQ radical anion would be expected, which is not the case. Therefore, the scenario for BTBT1-5 and BTBT8 with the TCNQ–F₂TCNQ is clearly the formation of CTC, as mentioned above. The tendency of the BTBT backbone to form 1:1 mixed crystals, as found for BTBT1 and the whole dopant series, lends further support for this interpretation, as supporting GIXRD experiments show indications of the formation of a mixed crystal structure for BTBT1-5. For phase separated systems, the lack of spatial overlap between the OSC HOMO and the dopant LUMO inhibits the formation of CTCs.

*GIXRD data on BTBT_x:F_xTCNQ is not shown in this thesis

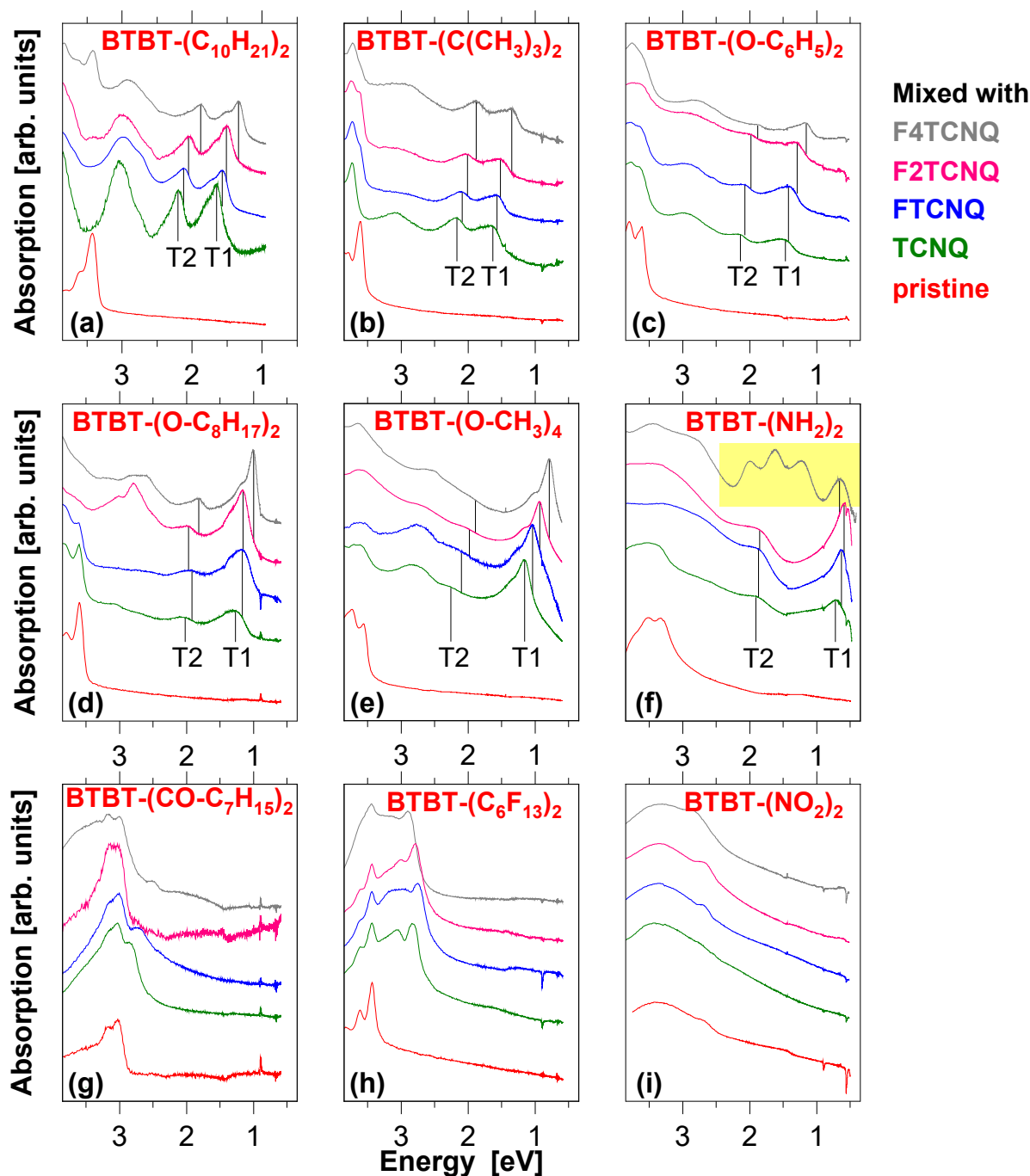


Figure 6.3: UV-vis/NIR absorption spectra of pristine BTBTx-films and mixed films of BTBTx and TCNQ derivatives in a nominal mixing ratio of 1:1, see the IE and EA values for the OSCs and dopants, respectively, in table 6.1 together with the nomenclature of the BTBT derivatives. (a)–(f) Equimolar mixed films showing CTC formation which is marked as peaks T1 and T2, (g)–(i) Systems without CTC formation due to phase separation, as shown by supporting GIXRD measurements (diffraction data not shown in this thesis). The spectrum of BTBT8:F4TCNQ film is highlighted because of the significant difference in the absorption peaks in the low energy region (see detailed discussion in the text).

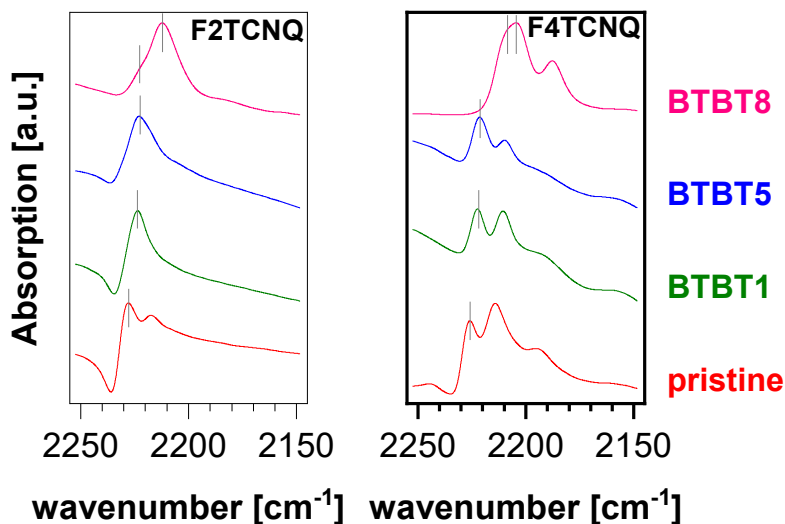


Figure 6.4: FTIR spectra of thin-films of BTBT1, BTBT5 and BTBT7 doped with F2TCNQ and F4TCNQ, in a nominal mixing ratio of 1:1. The IR data from pristine F2TCNQ and F4TCNQ films is shown at as bottom curves, for reference. Note that data in the region of only C≡N-stretching mode is shown. The wavenumber used for analysis is marked by a tick.

FTIR spectroscopy gives (from characteristic shifts in the C≡N stretching mode of F_xTCNQ) indications for the degree of charge transfer as explained in section 2.3.1 of chapter 2; data on BTPT1, BTBT5, and BTBT8 are shown in figure 6.4. The C≡N stretching mode shifts only slightly with decreasing IE of the BTBT derivative (from BTBT1 over BTBT5 to BTBT8), equally for F2TCNQ and F4TCNQ. A much stronger shift is observed for the BTBT8:F4TCNQ case, in line with its unique behavior in UV-vis/NIR as well. Note that the values of the C≡N stretching mode for the neutral acceptors F2TCNQ and F4TCNQ are 2228 cm⁻¹ and 2226 cm⁻¹, respectively, and the shift towards the radical anions is about 30 cm⁻¹ to lower energies [90, 303, 304].

The increased energy of the lowest optical transition for BTBT8:F4TCNQ, at first glance off the trend expected for a CTC related transition (see below), and the generally changed structure of the absorption spectrum (four instead of two peaks) hint to an entirely different scenario. The simplest explanation of these findings would be a transition from CTC to IPA formation. Regarding the CTC transition in a case of $IE - EA < 0$, that is for a very strong p-dopant acting on a given OSC, notably an increase in the transition energy of the CTC would indeed be expected according to equation 2.6. The much higher degree of charge transfer for the BTBT8:F4TCNQ blend as deduced from the shift of the dopant's C≡N vibrations in FTIR (figure 6.4) equally points into that direction. However, the lack of the typical F4TCNQ radical anion transitions in UV-vis/NIR together with the occurrence of three additional peaks at higher energy (instead of one that would correspond to the BTBT8 radical cation formed by integer charge transfer) still leaves some space for interpretation of the doping scenario. Currently, simulations on the DFT level are being performed in our group (contributed by Melissa Berteau-Reinville) to find a

more definitive explanation of these peaks, where possible scenarios range from IPA formation with F4TCNQ^{•-} related peaks being masked by the strong additional transitions (related to BTBT8^{•+}), over the four peaks being the optical signature of an anionic CTC, to a superposition of both situations.

6.3 Doping with Lewis Acids

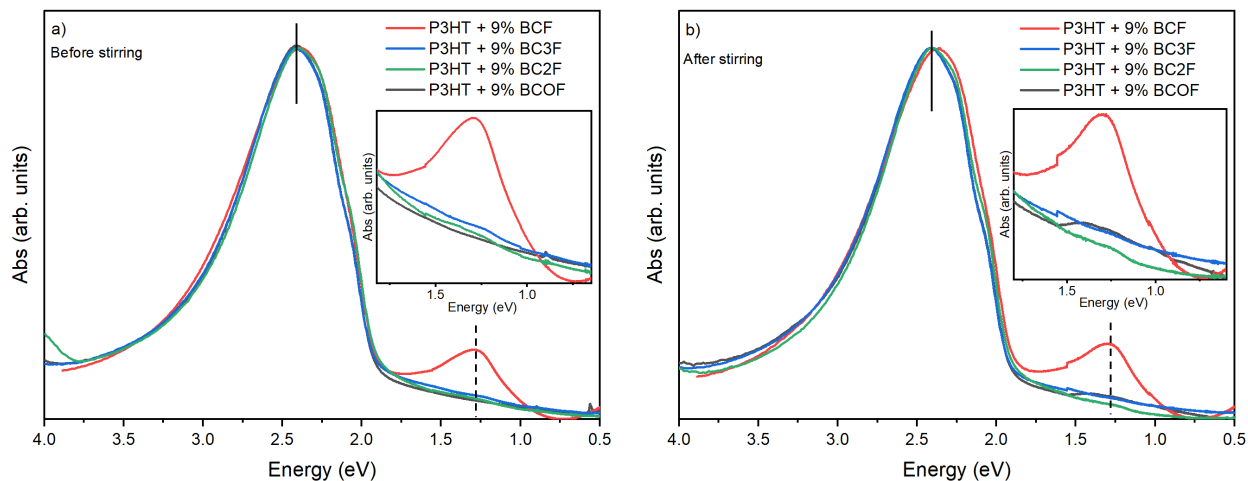


Figure 6.5: UV-vis/NIR spectra of P3HT doped with BCF, BC3F, BC2F and BCOF (a) before stirring, (b) after stirring. The dashed line shows the polaronic feature of P3HT and the solid line shows the fundamental absorption of P3HT. The inset images highlights the P3HT polaronic features.

Although F4TCNQ has a high electron affinity of ~ 5.1 eV (see table 6.1) that can effectively p-dope most relevant OSCs. However, due to its planar structure it is prone to forming CTC with planar OSCs. Further, F4TCNQ is generally susceptible to diffusion through the OSC layers [305], in particular at elevated temperature (e.g., F4TCNQ starts to desorb at 80°C and complete desorption occurs at 120°C upon annealing solid films)[154]. Diffusion of molecular dopants is highly detrimental to device stability in applications of OSCs and, thus, must be avoided. Therefore, as most straightforward approach the molecular weight of a dopant must be increased, which calls for the bulky dopant design to inhibit diffusion while still retaining high electron affinity. One bulky candidate would be Lewis acids (LAs) such as tris(pentafluorophenyl)borane (BCF, see chemical structures of all Lewis acids mentioned in the following in figure A.3 of Appendix A), an approach that gained attention after Welch et al. reported p-doping of oligomers and CPs via LAs of varying EA [306, 307].

In literature, the p-doping with BCF was first explained to occur via Lewis acid-base adduct formation. This is a somewhat obvious thought, as the electrophilic boron has a tendency to covalently bind to sites bearing a lone-pair of electrons (e.g., nitrogen), which are often found in the LA-doped OSC (then acting as a Lewis base). This worked as an inspiration for several research groups to explore the doping properties of LAs. Pingel et

al. reported the p-doping of P3HT (however, as a very weak Lewis base comprising sulfur sites instead of nitrogen) observing a phenomenology reminiscent of IPA formation, as found for P3HT-F4TCNQ [308] and even outperforming its doping efficiency. This is however very surprising because BCF has an EA (~ 3.4 eV) which is significantly lower than the P3HT IE (~ 4.8 eV) and should inhibit integer charge transfer [89, 309], but still P3HT showed indications of successful doping with BCF (both in solution and the solid state). The absorption spectra of P3HT doped with BCF showed P3HT polaronic features below ~ 1.8 eV and electron paramagnetic resonance spectroscopy (EPR) confirmed the presence of P3HT cations and BCF anions [308] despite IPA formation cannot be expected to occur due to the large difference between IE and EA of OSC and LA. Furthermore, the p-doping of CP with BCF resulted in a notable enhancement in conductivity, comparable to the values observed with F4TCNQ in earlier studies, therefore, the formation of mobile holes, as the ultimate goal of p-doping the semiconductor, is clearly evidenced [308, 310].

To remedy this inconsistencies, later Yurash et al. attempted to explain the doping with LA to be a two step process where, in the first step, LA first forms a covalent complex with H_2O which is a strong Brønsted acid. In the second step, this LA- H_2O complex protonates a segment of the CP which is then followed by electron transfer from neutral CP segment to the protonated one [311]. Still, however, this process does not appear to fully capture the processes at work because it entails energy barriers which are unlikely to be overcome [312]. Therefore, investigating this process further to fully understand the parameters governing LA-doping of OSCs remains key to fully exploiting the potential of this approach. The doping of CPs with LAs has been a mystery for quite sometime, given the much lower electron affinity of LAs as compared to ionization energy of CPs [306, 308]. Fully understanding the LA-doping of OSCs is an ongoing research topic in our group. In one approach to better understand the doping mechanism of LAs, we wish to investigate the role of different electron affinities enabled by a series of LAs, in doping of P3HT. I was substantially involved in performing UV-vis/NIR and FTIR[†] experiments on thin-films of P3HT doped with BCF and a series of lesser fluorinated BCF derivatives. Notably, to minimize the influence the impact of water in the process (as suggested by Yurash et al. [311]) working in a high quality glovebox atmosphere (immediately after regeneration and exchange of the molecular sieve to capture H_2O) is mandatory, which has been done in my responsibility for the glovebox in our lab. Figure 6.5 shows the UV-vis/NIR spectra of P3HT thin films doped with LAs: BCF, BC3F, BC2F, and BCOF. Spectra were recorded on films fabricated from solution, both before (figure 6.5(a)) and after (Figure 6.5(b)) subjecting the LA-doped P3HT solutions to 24 hours of stirring. In figure 6.5 it was observed that, in contrast to the instantaneous doping of P3HT by BCF, no doping-related spectroscopic features were observed for BC3F and BC2F. However, BCOF did show indications of being able to weakly dope P3HT only after 24 hour stirring. These experiments were done to compliment the research efforts of Melissa Berteau-Rainville (PhD student co-supervised with Dr. Orgiu at the INRS), who is using a combination of computational and other experimental techniques to resolve this long standing mystery in the field. This work is part of an ongoing collaboration with

[†]Only UV-vis/NIR results are shown in this section, as no conclusions could be drawn from FTIR results, yet.

the groups of Drs. Baumgartner and Caputo (York University), who provided the BCF-derivatives mentioned above. This work is ongoing, publication is planned for 2025.

Chapter 7

Summary, Conclusions, and Outlook

Organic semiconductors have attracted significant interest, particularly after OLEDs were introduced to finally revolutionize organic electronics in 1987 [313], gaining popularity in displays and lighting due to their lightweight and flexible design. A major breakthrough in realizing the potential of organic electronics was the successful electrical doping of organic semiconductors [114], where introducing doped charge-transport layers in standard device architectures enabled OLEDs to achieve the performance necessary for commercial use. A precise control over electrical conductivity and the control over interfacial energetics, both achieved by doping of OSCs, remain essential for application in organic devices. The doping efficiency and the charge transport behavior in CP thin films, is suggested to be influenced by their microstructure where the structural disorder inherent to CP thin films, translates into energetic disorder.

One aim of this thesis is to enable elucidating the role of microstructure in doping of CPs, by exploiting HV-ESD as highly unconventional technique for depositing P3HT with minimum solvent interference. First, we extensively tested the parameters such as—compatibility of substrate, solvents, solution concentration, injection rate and applied voltage—to ensure reliable deposition of P3HT films under minimum solvent influence. During parameter optimization, we observed that chloroform, unlike other solvents, does not produce a measurable current during HV-ESD, suggesting rapid evaporation before reaching the substrate. P3HT films fabricated using the optimized parameters yielded amorphous P3HT films, that was confirmed via GIXRD measurements. Notably, the choice of initial solvent(s)—chloroform or toluene:methano—used to dissolve P3HT did not affect the outcome, as highly amorphous P3HT films were consistently achieved via HV-ESD. This result suggests that the absence of solvent during surface nucleation and crystallization, combined with limited diffusion of P3HT on the substrate, led to the formation of highly amorphous structures in typically semi-crystalline P3HT, although smooth SiO_x wafers, selected as substrates, promote surface diffusion. This contrasts with the results achieved by conventional solution-processing techniques like spin-coating and drop-casting, which typically yield semi-crystalline films with coexisting amorphous and crystalline regions. These regions exhibit distinct ionization energies and different abilities for dopants to penetrate the film, where prior studies indicate that they thus react differently to dopant exposure. By doping these purely amorphous films, it will now be possible to identify specific spectral signatures of charge transfer in disor-

dered P3HT, ultimately advancing the understanding of doping behavior in this complex semi-crystalline system. We are currently working on doping amorphous P3HT films by exposing them to thermally sublimated F4TCNQ vapors to perform sequential doping of the films. The highly amorphous CP films established via HV-ESD can also be used in devices such as polymer based OLEDs, mechanically flexible organic photodetectors or photovoltaics, where employing amorphous films can be advantageous.

In parallel, we also investigated the structural and optical properties of mixed-crystalline films of 6T and 6P in a 1:1 ratio, fabricated via vacuum codeposition. Previous studies on vacuum coevaporation of rod-like conjugated molecules of similar shape, such as pentacene and perfluoropentacene, have shown the formation of mixed crystals with cofacially stacked molecules. Given the similar conjugated core lengths of 6T and 6P and significant spectral overlap between 6P emission and 6T absorption, it was anticipated for 6T and 6P to show efficient resonance energy transfer. Prior reports on layered heterostructures of 6P/6T revealed that their emission could be tuned from yellow and red through white to blue by adjusting their stacking distance. From XRD, it had been suggested before that the vacuum coevaporation of 6T and 6P could result in mixed crystal structure formation. Using FTIR analysis, we confirmed indeed molecular-level mixing through the absence of the characteristic Davydov splitting in 6T, which is indicative of the crystalline 6T structure. Our XRD data indicated a mixed-crystal structure in 1:1 films for films deposited on different substrates. Crystal structure analysis of these films revealed that the mixed films have a unit cell which is capable of accommodating two molecules, suggesting a herringbone molecular arrangement within the film. Bragg rods observed in standing films on silicon dioxide suggested a layered mixed crystal structure with uncorrelated layers. PL studies showed green emission in addition to the characteristic red and blue emissions of pristine 6T and 6P, respectively. Such emission behavior was observed for films deposited on different substrates and supported by absorption spectroscopy and structural analyses, indicating contributions from both J- and H-type aggregation of 6T within the blend. These findings suggest that the unique optical properties observed in 6T/6P heterostructures are retained in the mixed phase, highlighting the potential of functional organic semiconductor blends for tailoring optoelectronic properties and creating materials with enhanced or novel functionalities.

In summary, in this work we successfully established amorphous P3HT films from gas phase ions using HV-ESD. These films now serve as the basis of future work on investigating the role of microstructure in the CTC *versus* IPA formation scenarios upon p-doping of P3HT with molecular dopants. We also demonstrated the ability to tailor the optical properties of in-vacuo codeposited COMs, for their possible application in optoelectronic devices.

Bibliography

- [1] A. Köhler and H. Bässler, *Electronic processes in organic semiconductors: An introduction*. John Wiley & Sons, 2015.
- [2] J.-D. Chai and M. Head-Gordon, “[Long-range corrected hybrid density functionals with damped atom–atom dispersion corrections](#),” *Physical Chemistry Chemical Physics*, vol. 10, no. 44, p. 6615, 2008.
- [3] M. J. Frisch, G. W. Trucks, H. B. Schlegel, G. E. Scuseria, M. A. Robb, J. R. Cheeseman, G. Scalmani, V. Barone, B. Mennucci, G. A. Petersson, H. Nakatsuji, M. Caricato, X. Li, H. P. Hratchian, A. F. Izmaylov, J. Bloino, G. Zheng, J. L. Sonnenberg, M. Hada, M. Ehara, K. Toyota, R. Fukuda, J. Hasegawa, M. Ishida, T. Nakajima, Y. Honda, O. Kitao, H. Nakai, T. Vreven, J. A. Montgomery, Jr., J. E. Peralta, F. Ogliaro, M. Bearpark, J. J. Heyd, E. Brothers, K. N. Kudin, V. N. Staroverov, R. Kobayashi, J. Normand, K. Raghavachari, A. Rendell, J. C. Burant, S. S. Iyengar, J. Tomasi, M. Cossi, N. Rega, J. M. Millam, M. Klene, J. E. Knox, J. B. Cross, V. Bakken, C. Adamo, J. Jaramillo, R. Gomperts, R. E. Stratmann, O. Yazyev, A. J. Austin, R. Cammi, C. Pomelli, J. W. Ochterski, R. L. Martin, K. Morokuma, V. G. Zakrzewski, G. A. Voth, P. Salvador, J. J. Dannenberg, S. Dapprich, A. D. Daniels, Ö. Farkas, J. B. Foresman, J. V. Ortiz, J. Cioslowski, and D. J. Fox, “Gaussian 09 Revision E.01 (Gaussian Inc., Wallingford, CT),” Wallingford, CT, 2009.
- [4] S. Hotta, S. Rughooputh, A. Heeger, and F. Wudl, “Spectroscopic studies of soluble poly (3-alkylthienylenes),” *Macromolecules*, vol. 20, no. 1, pp. 212–215, 1987.
- [5] A. Tamanai, S. Beck, and A. Pucci, “Mid-infrared characterization of thiophene-based thin polymer films,” *Displays*, vol. 34, no. 5, pp. 399–405, 2013.
- [6] K. N. Baker, A. V. Fratini, T. Resch, H. C. Knachel, W. Adams, E. Socci, and B. Farmer, “[Crystal structures, phase transitions and energy calculations of poly\(p-phenylene\) oligomers](#),” *Polymer*, vol. 34, no. 8, pp. 1571–1587, 1993.
- [7] D.-M. Smilgies, “[Phenylene lattices](#),” *Acta Crystallographica Section B*, vol. 61, no. 3, pp. 357–358, 2005.
- [8] C. Simbrunner, G. Hernandez-Sosa, F. Quochi, G. Schwabegger, C. Botta, M. Oehzelt, I. Salzmann, T. Djuric, A. Neuhold, R. Resel, M. Saba, A. Mura, G. Bongiovanni, A. Vollmer, N. Koch, and H. Sitter, “[Color tuning of nanofibers by periodic organic-organic hetero-epitaxy](#),” *ACS Nano*, vol. 6, no. 6, pp. 4629–4638, 2012.

- [9] J. Simbrunner, C. Simbrunner, B. Schrode, C. Rothel, N. Bedoya-Martinez, I. Salzmänn, and R. Resel, “[Indexing of grazing-incidence x-ray diffraction patterns: the case of fibre-textured thin films](#),” *Acta Crystallographica a-Foundation and Advances*, vol. 74, no. 4, pp. 373–387, 2018.
- [10] J. Simbrunner, S. Hofer, B. Schrode, Y. Garmshausen, S. Hecht, R. Resel, and I. Salzmänn, “[Indexing grazing-incidence x-ray diffraction patterns of thin films: lattices of higher symmetry](#),” *Journal of Applied Crystallography*, vol. 52, no. 2, pp. 428–439, 2019.
- [11] J. Simbrunner, B. Schrode, J. Domke, T. Fritz, I. Salzmänn, and R. Resel, “[An efficient method for indexing grazing-incidence x-ray diffraction data of epitaxially grown thin films](#),” *Acta Crystallogr A Found Adv*, vol. 76, no. 3, pp. 345–357, 2020.
- [12] J. T. Liu, H. Hase, S. Taylor, I. Salzmänn, and P. Forgione, “[Approaching the integer-charge transfer regime in molecularly doped oligothiophenes by efficient decarboxylative cross-coupling](#),” *Angewandte Chemie International Edition*, vol. 59, pp. 7146–7153, 2020.
- [13] H. Hase, “Integer and fractional charge transfer in the doping of poly-and oligothiophenes,” Ph.D. dissertation, Concordia University, 2023.
- [14] J. Hu, N. Aghdassi, S. Bhagat, Y. Garmshausen, R. Wang, N. Koch, S. Hecht, S. Duhm, and I. Salzmänn, “Dipolar substitution impacts growth and electronic properties of para-sexiphenyl thin films,” *Advanced Materials Interfaces*, vol. 7, no. 3, p. 1901707, 2020.
- [15] S. Bhagat, H. Hase, and I. Salzmänn, *Chemical doping of organic semiconductors*. Elsevier - Woodhead Publishing, 2021, pp. 107–141.
- [16] H. Hase and I. Salzmänn, “[Doping in organic semiconductors](#),” in *Handbook of Organic Materials for Electronic and Photonic Devices, 2nd Edition*, O. Ostroverkhova, Ed. Woodhead Publishing, 2018, pp. 349–383.
- [17] S. Bhagat, W. D. Leal, M. B. Majewski, J. Simbrunner, S. Hofer, R. Resel, and I. Salzmänn, “[Aggregate formation in crystalline blends of \$\alpha\$ -sexithiophene and para-sexiphenyl](#),” *Electronic Structure*, vol. 3, p. 034004, 2021.
- [18] G. Zhang, T. Patel, P. Nallepalli, S. Bhagat, H. Hase, A. M. Jazani, I. Salzmänn, Z. Ye, and J. K. Oh, “[Macromolecularly engineered thermoreversible heterogeneous self-healable networks encapsulating reactive multidentate block copolymer-stabilized carbon nanotubes](#),” *Macromolecular Rapid Communications*, vol. 42, p. 2000514, 2021.
- [19] S. Charoughchi, J. T. Liu, M. Berteau-Rainville, H. Hase, M. S. Askari, S. Bhagat, P. Forgione, and I. Salzmänn, “Sterically-hindered molecular p-dopants promote integer charge transfer in organic semiconductors,” *Angewandte Chemie*, vol. 135, no. 31, p. e202304964, 2023.

- [20] S. Bhagat, M. Berteau-Rainville, S. Beram, and I. Salzmänn, “[Amorphous poly\(3-hexylthiophene\)\(p3ht\) thin films by vacuum electrospray deposition](#),” *Crystal Growth & Design*, vol. 24, no. 15, pp. 6105–6114, 2024.
- [21] S. Bhagat, M. Berteau-Rainville, A. Opitz, H. Mendez, A. Jung, K. Sauer, B. Wegner, P. Beyer, K. Matte, H. Hase, N. Koch, G. Heimel, I. Salzmänn, and Y. Geerts, “Tuneable low gap mixed-stack charge-transfer crystals,” *To be submitted*.
- [22] M. Berteau-Rainville, T. P. L. Cosby, S. Bhagat, A. E. Laturski, E. Orgiu, T. Baumgartner, C. B. Caputo, and I. Salzmänn, “Degradation-assisted doping of organic semiconductors: a new strategy enabled by lewis acids,” *To be submitted*.
- [23] C. Koutsiaki, T. Kaimakamis, A. Zachariadis, A. Papamichail, C. Kamaraki, S. Fachouri, C. Gravalidis, A. Laskarakis, and S. Logothetidis, “Efficient combination of roll-to-roll compatible techniques towards the large area deposition of a polymer dielectric film and the solution-processing of an organic semiconductor for the field-effect transistors fabrication on plastic substrate,” *Organic Electronics*, vol. 73, pp. 231–239, 2019.
- [24] M. Mas-Torrent and C. Rovira, “Novel small molecules for organic field-effect transistors: towards processability and high performance,” *Chemical Society Reviews*, vol. 37, no. 4, pp. 827–838, 2008.
- [25] K. Liu, B. Ouyang, X. Guo, Y. Guo, and Y. Liu, “[Advances in flexible organic field-effect transistors and their applications for flexible electronics](#),” *npj Flexible Electronics*, vol. 6, no. 1, 2022.
- [26] A. Kleinschmidt and D. J. Lipomi, “[Stretchable conjugated polymers: A case study in topic selection for new research groups](#),” *Accounts of Chemical Research*, vol. 51, no. 12, pp. 3134–3143, 2018.
- [27] J. S. Heo, J. Eom, Y.-H. Kim, and S. K. Park, “Recent progress of textile-based wearable electronics: a comprehensive review of materials, devices, and applications,” *Small*, vol. 14, no. 3, p. 1703034, 2018.
- [28] P. C. Chow and T. Someya, “Organic photodetectors for next-generation wearable electronics,” *Advanced Materials*, vol. 32, no. 15, p. 1902045, 2020.
- [29] E. Iusupovskaia, A. Y. Gerasimenko, S. Selishchev, D. Telyshev, and A. Markov, “Organic semiconductors with p-i-n structure for optoelectronic neurostimulation,” *Biomedical Engineering*, vol. 58, no. 2, pp. 143–146, 2024.
- [30] J. Borges-González, C. J. Kousseff, and C. B. Nielsen, “Organic semiconductors for biological sensing,” *Journal of Materials Chemistry C*, vol. 7, no. 5, pp. 1111–1130, 2019.
- [31] C. Liao, C. Mak, M. Zhang, H. L. Chan, and F. Yan, “Flexible organic electrochemical transistors for highly selective enzyme biosensors and used for saliva testing,” *Adv. Mater.*, vol. 27, no. 4, pp. 676–681, 2015.

- [32] T. Nezakati, A. Seifalian, A. Tan, and A. M. Seifalian, “[Conductive polymers: Opportunities and challenges in biomedical applications](#),” *Chemical Reviews*, vol. 118, no. 14, pp. 6766–6843, 2018.
- [33] D. Zhang, T. Huang, and L. Duan, “Emerging self-emissive technologies for flexible displays,” *Advanced Materials*, vol. 32, no. 15, p. 1902391, 2020.
- [34] M.-C. Choi, Y. Kim, and C.-S. Ha, “Polymers for flexible displays: From material selection to device applications,” *Progress in Polymer Science*, vol. 33, no. 6, pp. 581–630, 2008.
- [35] F. C. Franco Jr and A. A. B. Padama, “Dft and td-dft study on the structural and optoelectronic characteristics of chemically modified donor-acceptor conjugated oligomers for organic polymer solar cells,” *Polymer*, vol. 97, pp. 55–62, 2016.
- [36] H. Bronstein, C. B. Nielsen, B. C. Schroeder, and I. McCulloch, “[The role of chemical design in the performance of organic semiconductors](#),” *Nature Reviews Chemistry*, vol. 4, no. 2, pp. 66–77, 2020.
- [37] F. C. Franco Jr, “Computational study on optoelectronic property tuning of oligothiophenes via chemical modifications for solar cell applications,” *Asian Journal of Chemistry*, vol. 30, no. 2, p. 329, 2018.
- [38] Q. Zhang, B. Li, S. Huang, H. Nomura, H. Tanaka, and C. Adachi, “Efficient blue organic light-emitting diodes employing thermally activated delayed fluorescence,” *Nature Photonics*, vol. 8, no. 4, pp. 326–332, 2014.
- [39] S. Wu, S. Li, Q. Sun, C. Huang, and M.-K. Fung, “Highly efficient white organic light-emitting diodes with ultrathin emissive layers and a spacer-free structure,” *Scientific Reports*, vol. 6, no. 1, p. 25821, 2016.
- [40] J. Lee, H.-F. Chen, T. Batagoda, C. Coburn, P. I. Djurovich, M. E. Thompson, and S. R. Forrest, “Deep blue phosphorescent organic light-emitting diodes with very high brightness and efficiency,” *Nature Materials*, vol. 15, no. 1, pp. 92–98, 2016.
- [41] J. Hynynen, D. Kiefer, and C. Muller, “[Influence of crystallinity on the thermoelectric power factor of p3ht vapour-doped with f4tcnq](#),” *RSC Advances*, vol. 8, pp. 1593–1599, 2018.
- [42] G. Zuo, O. Andersson, H. Abdalla, and M. Kemerink, “High thermoelectric power factor from multilayer solution-processed organic films,” *Applied Physics Letters*, vol. 112, no. 8, 2018.
- [43] J. Cha, H. Jin, M. K. Kim, J. H. Park, and M. Kim, “Evaporation-controlled spray deposition process achieving ultrasooth photoactive layer for efficient organic solar cells,” *Surfaces and Interfaces*, vol. 28, p. 101669, 2022.

- [44] C. Zisis, E. Pechlivani, S. Tsimikli, E. Mekeridis, A. Laskarakis, and S. Logothetidis, "Organic photovoltaics on greenhouse rooftops: effects on plant growth," *Materials Today: Proceedings*, vol. 19, pp. 65–72, 2019.
- [45] T. Fukuda, K. Takagi, T. Asano, Z. Honda, N. Kamata, K. Ueno, H. Shirai, J. Ju, Y. Yamagata, and Y. Tajima, "Bulk heterojunction organic photovoltaic cell fabricated by the electrospray deposition method using mixed organic solvent," *Physica Status Solidi-Rapid Research Letters*, vol. 5, pp. 229–231, 2011.
- [46] A. Camus, M. Reali, and C. Santato, "Advances in high-resolution printed transistors: The case of bio-sourced organic materials," *Current Opinion in Green and Sustainable Chemistry*, vol. 34, p. 100594, 2022.
- [47] H. Sirringhaus, "Device physics of solution-processed organic field-effect transistors," *Advanced Materials*, vol. 17, no. 20, pp. 2411–2425, 2005.
- [48] A. D. Scaccabarozzi, A. Basu, F. Aniés, J. Liu, O. Zapata-Arteaga, R. Warren, Y. Firdaus, M. I. Nugraha, Y. Lin, M. Campoy-Quiles *et al.*, "Doping approaches for organic semiconductors," *Chemical Reviews*, vol. 122, no. 4, pp. 4420–4492, 2021.
- [49] S. Sze and K. Ng, "Physics of semiconductor devices. hoboken, nj, usa: John 23 wiley & sons," 2006.
- [50] B. Lüssem, M. Riede, and K. Leo, "Doping of organic semiconductors," *physica status solidi (a)*, vol. 210, pp. 9–43, 2013.
- [51] M. Schwoerer and H. C. Wolf, *Organic molecular solids*. John Wiley & Sons, 2007.
- [52] J. H. Schön, C. Kloc, and B. Batlogg, "Universal crossover from band to hopping conduction in molecular organic semiconductors," *Physical Review Letters*, vol. 86, no. 17, p. 3843, 2001.
- [53] I. Salzmann, G. Heimel, M. Oehzelt, S. Winkler, and N. Koch, "Molecular Electrical Doping of Organic Semiconductors: Fundamental Mechanisms and Emerging Dopant Design Rules," *Accounts of Chemical Research*, vol. 49, pp. 370–378, 2016.
- [54] R. Resel, N. Koch, F. Meghdadi, G. Leising, W. Unzog, and K. Reichmann, "Growth and preferred crystallographic orientation of hexaphenyl thin films," *Thin Solid Films*, vol. 305, no. 1-2, pp. 232–242, 1997.
- [55] P. Frank, G. Hlawacek, O. Lengyel, A. Satka, C. Teichert, R. Resel, and A. Winkler, "Influence of surface temperature and surface modifications on the initial layer growth of para-hexaphenyl on mica (0 0 1)," *Surface science*, vol. 601, no. 10, pp. 2152–2160, 2007.
- [56] S. Pratontep, M. Brinkmann, F. Nüesch, and L. Zuppiroli, "Nucleation and growth of ultrathin pentacene films on silicon dioxide: effect of deposition rate and substrate temperature," *Synthetic Metals*, vol. 146, no. 3, pp. 387–391, 2004.

- [57] M. Kratzer, S. Klima, C. Teichert, B. Vasić, A. Matković, U. Ralević, and R. Gajić, “Temperature dependent growth morphologies of parahexaphenyl on sio2 supported exfoliated graphene,” *Journal of Vacuum Science & Technology B*, vol. 31, no. 4, 2013.
- [58] L. Athouel, G. Froyer, M. Riou, and M. Schott, “Structural studies of parasexiphenyl thin films: importance of the deposition parameters,” *Thin Solid Films*, vol. 274, no. 1-2, pp. 35–45, 1996.
- [59] R. Resel and G. Leising, “High resolution x-ray diffraction studies on hexaphenyl thin films,” *Surface science*, vol. 409, no. 2, pp. 302–306, 1998.
- [60] P. Kovacik, “Vacuum deposition of organic molecules for photovoltaic applications,” Thesis, University of Oxford, 2012.
- [61] Y.-J. Kim, S. Lee, M. R. Niazi, K. Hwang, M.-C. Tang, D.-H. Lim, J.-S. Kang, D.-M. Smilgies, A. Amassian, and D.-Y. Kim, “[Systematic study on the morphological development of blade-coated conjugated polymer thin films via in situ measurements](#),” *ACS Applied Materials & Interfaces*, vol. 12, no. 32, pp. 36 417–36 427, 2020.
- [62] H. Zhao, H. B. Naveed, B. Lin, X. Zhou, J. Yuan, K. Zhou, H. Wu, R. Guo, M. A. Scheel, A. Chumakov, S. V. Roth, Z. Tang, P. Müller-Buschbaum, and W. Ma, “[Hot hydrocarbon-solvent slot-die coating enables high-efficiency organic solar cells with temperature-dependent aggregation behavior](#),” *Advanced Materials*, vol. 32, no. 39, p. 2002302, 2020.
- [63] W. Ma, G. Yang, K. Jiang, J. H. Carpenter, Y. Wu, X. Meng, T. McAfee, J. Zhao, C. Zhu, C. Wang, H. Ade, and H. Yan, “[Influence of processing parameters and molecular weight on the morphology and properties of high-performance pffbt4t-2od:pc71bm organic solar cells](#),” *Advanced Energy Materials*, vol. 5, no. 23, p. 1501400, 2015.
- [64] D. M. DeLongchamp, B. M. Vogel, Y. Jung, M. C. Gurau, C. A. Richter, O. A. Kirillov, J. Obrzut, D. A. Fischer, S. Sambasivan, L. J. Richter, and E. K. Lin, “[Variations in semiconducting polymer microstructure and hole mobility with spin-coating speed](#),” *Chemistry of Materials*, vol. 17, no. 23, pp. 5610–5612, 2005.
- [65] J. Clark, J.-F. Chang, F. C. Spano, R. H. Friend, and C. Silva, “[Determining exciton bandwidth and film microstructure in polythiophene films using linear absorption spectroscopy](#),” *Applied Physics Letters*, vol. 94, no. 16, pp. 163 306–163 306, 2009.
- [66] M. Pandey, J. Toyoda, S. Sharma, Y. Cho, H. Benten, S. S. Pandey, and M. Nakamura, “The role of solvents in the microstructure and charge transport of semiconducting polymer films prepared at the air–liquid interface,” *Journal of Materials Chemistry C*, 2023.
- [67] C.-D. Park, T. A. Fleetham, J. Li, and B. D. Vogt, “[High performance bulk-heterojunction organic solar cells fabricated with non-halogenated solvent processing](#),” *Organic Electronics*, vol. 12, no. 9, pp. 1465–1470, 2011.

- [68] E. S. Radchenko, D. V. Anokhin, K. L. Gerasimov, A. I. Rodygin, A. A. Rychkov, E. D. Shabratova, S. Grigorian, and D. A. Ivanov, "Impact of the solubility of organic semiconductors for solution-processable electronics on the structure formation: a real-time study of morphology and electrical properties," *Soft Matter*, vol. 14, pp. 2560–2566, 2018.
- [69] M. Li, A. H. Balawi, P. J. Leenaers, L. Ning, G. H. L. Heintges, T. Marszalek, W. Pisula, M. M. Wienk, S. C. J. Meskers, Y. Yi, F. Laquai, and R. A. J. Janssen, "Impact of polymorphism on the optoelectronic properties of a low-bandgap semi-conducting polymer," *Nature Communications*, vol. 10, no. 1, p. 2867, 2019.
- [70] J. Wang, Y. Liu, L. Hua, T. Wang, H. Dong, H. Li, X. Sun, Z. Ren, and S. Yan, "Oriented conjugated copolymer films with controlled crystal forms and molecular stacking modes for enhanced charge transport and photoresponsivity," *ACS Applied Polymer Materials*, vol. 3, no. 4, pp. 2098–2108, 2021.
- [71] J. Zhao, Y. Li, G. Yang, K. Jiang, H. Lin, H. Ade, W. Ma, and H. Yan, "Efficient organic solar cells processed from hydrocarbon solvents," *Nature Energy*, vol. 1, no. 2, p. 15027, 2016.
- [72] H. W. Ro, J. M. Downing, S. Engmann, A. A. Herzing, D. M. DeLongchamp, L. J. Richter, S. Mukherjee, H. Ade, M. Abdelsamie, L. K. Jagadamma *et al.*, "Morphology changes upon scaling a high-efficiency, solution-processed solar cell," *Energy & Environmental Science*, vol. 9, no. 9, pp. 2835–2846, 2016.
- [73] S. T. e. Reynolds J.R., Thompson B.C., *Conjugated Polymers: Properties, Processing, and Applications*, 4th ed., ser. Handbook of Conducting Polymers. CRC Press, 2019.
- [74] A. Salleo, "Impact of organic semiconductor microstructure on transport: Basic concepts," in *THE WSPC REFERENCE ON ORGANIC ELECTRONICS: ORGANIC SEMICONDUCTORS: Basic Concepts*. World Scientific, 2016, pp. 293–323.
- [75] D. T. Scholes, P. Y. Yee, J. R. Lindemuth, H. Kang, J. Onorato, R. Ghosh, C. K. Luscombe, F. C. Spano, S. H. Tolbert, and B. J. Schwartz, "The effects of crystallinity on charge transport and the structure of sequentially processed f4tcnq-doped conjugated polymer films," *Advanced Functional Materials*, vol. 27, no. 44, p. 1702654, 2017.
- [76] I. E. Jacobs, E. W. Aasen, J. L. Oliveira, T. N. Fonseca, J. D. Roehling, J. Li, G. Zhang, M. P. Augustine, M. Mascal, and A. J. Moulé, "Comparison of solution-mixed and sequentially processed P3HT:F4TCNQ films: Effect of doping-induced aggregation on film morphology," *Journal of Materials Chemistry C*, vol. 4, pp. 3454–3466, 2016.
- [77] J.-L. Brédas, J. P. Calbert, D. da Silva Filho, and J. Cornil, "Organic semiconductors: A theoretical characterization of the basic parameters governing charge transport," *Proceedings of the National Academy of Sciences*, vol. 99, no. 9, pp. 5804–5809, 2002.

- [78] B. Neelamraju, K. E. Watts, J. E. Pemberton, and E. L. Ratcliff, "Correlation of coexistent charge transfer states in f4tcnq-doped p3ht with microstructure," *The Journal of Physical Chemistry Letters*, vol. 9, no. 23, pp. 6871–6877, 2018.
- [79] E. Lim, K. A. Peterson, G. M. Su, and M. L. Chabinyc, "Thermoelectric Properties of Poly(3-hexylthiophene) (P3HT) Doped with 2,3,5,6-Tetrafluoro-7,7,8,8-tetracyanoquinodimethane (F₄ TCNQ) by Vapor-Phase Infiltration," *Chemistry of Materials*, vol. 30, pp. 998–1010, 2018.
- [80] I. E. Jacobs, C. Cendra, T. F. Harrelson, Z. I. Bedolla Valdez, R. Faller, A. Salleo, and A. J. Moulé, "Polymorphism controls the degree of charge transfer in a molecularly doped semiconducting polymer," *Materials Horizons*, vol. 5, pp. 655–660, 2018.
- [81] J. Hynynen, D. Kiefer, L. Yu, R. Kroon, R. Munir, A. Amassian, M. Kemerink, and C. Müller, "Enhanced Electrical Conductivity of Molecularly p-Doped Poly(3-hexylthiophene) through Understanding the Correlation with Solid-State Order," *Macromolecules*, vol. 50, pp. 8140–8148, 2017.
- [82] L. Müller, D. Nanova, T. Glaser, S. Beck, A. Pucci, A. K. Kast, R. R. Schröder, E. Mankel, P. Pingel, D. Neher *et al.*, "Charge-transfer–solvent interaction predefines doping efficiency in p-doped p3ht films," *Chemistry of Materials*, vol. 28, no. 12, pp. 4432–4439, 2016.
- [83] J. Li, C. W. Rochester, I. E. Jacobs, E. W. Aasen, S. Friedrich, P. Stroeve, and A. J. Moulé, "The effect of thermal annealing on dopant site choice in conjugated polymers," *Organic Electronics*, vol. 33, pp. 23–31, 2016.
- [84] Y. Liu, B. Nell, K. Ortstein, Z. Wu, Y. Karpov, T. Beryozkina, S. Lenk, A. Kiriy, K. Leo, and S. Reineke, "High electron affinity molecular dopant cn6-cp for efficient organic light-emitting diodes," *ACS applied materials & interfaces*, vol. 11, no. 12, pp. 11 660–11 666, 2019.
- [85] K. Walzer, B. Maennig, M. Pfeiffer, and K. Leo, "Highly Efficient Organic Devices Based on Electrically Doped Transport Layers," *Chemical Reviews*, vol. 107, pp. 1233–1271, 2007.
- [86] M. Pfeiffer, K. Leo, X. Zhou, J. Huang, M. Hofmann, A. Werner, and J. Blochwitz-Nimoth, "Doped organic semiconductors: Physics and application in light emitting diodes," *Organic Electronics*, vol. 4, no. 2-3, pp. 89–103, 2003.
- [87] I. E. Jacobs and A. J. Moulé, "Controlling Molecular Doping in Organic Semiconductors," *Advanced Materials*, vol. 29, p. 1703063, 2017.
- [88] L. Zhu, E.-G. Kim, Y. Yi, and J.-L. Brédas, "Charge transfer in molecular complexes with 2, 3, 5, 6-tetrafluoro-7, 7, 8, 8-tetracyanoquinodimethane (f4-tcnq): A density functional theory study," *Chemistry of Materials*, vol. 23, no. 23, pp. 5149–5159, 2011.

- [89] P. Pingel, L. Zhu, K. S. Park, J.-O. Vogel, S. Janietz, E.-G. Kim, J. P. Rabe, J.-L. Brédas, and N. Koch, “Charge-Transfer Localization in Molecularly Doped Thiophene-Based Donor Polymers,” *The Journal of Physical Chemistry Letters*, vol. 1, pp. 2037–2041, 2010.
- [90] H. Méndez, G. Heimel, S. Winkler, J. Frisch, A. Opitz, K. Sauer, B. Wegner, M. Oehzelt, C. Röthel, S. Duhm, D. Többens, N. Koch, and I. Salzmann, “Charge-transfer crystallites as molecular electrical dopants,” *Nature Communications*, vol. 6, p. 8560, 2015.
- [91] I. Salzmann and G. Heimel, “Toward a comprehensive understanding of molecular doping organic semiconductors (review),” *Journal of Electron Spectroscopy and Related Phenomena*, vol. 204, pp. 208–222, 2015.
- [92] P. Pingel and D. Neher, “Comprehensive picture of p -type doping of P3HT with the molecular acceptor F₄TCNQ,” *Physical Review B*, vol. 87, 2013.
- [93] H. Hase, M. Berteau-Rainville, S. Charoughchi, W. Bodlos, E. Orgiu, and I. Salzmann, “Critical dopant concentrations govern integer and fractional charge-transfer phases in doped p3ht,” *Journal of Physics: Materials*, vol. 6, no. 1, p. 014004, 2022.
- [94] R. J. Kline, M. D. McGehee, E. N. Kadnikova, J. Liu, J. M. J. Fréchet, and M. F. Toney, “Dependence of regioregular poly(3-hexylthiophene) film morphology and field-effect mobility on molecular weight,” *American Chemical Society*, vol. 38, no. 8, pp. 3312–3319, 03 2005.
- [95] H. Yan and W. Ma, “Molecular doping efficiency in organic semiconductors: Fundamental principle and promotion strategy,” *Advanced Functional Materials*, vol. 32, no. 12, p. 2111351, 2022. [Online]. Available: <https://onlinelibrary.wiley.com/doi/abs/10.1002/adfm.202111351>
- [96] M. Skompska and A. Szkuřat, “The influence of the structural defects and microscopic aggregation of poly (3-alkylthiophenes) on electrochemical and optical properties of the polymer films: discussion of an origin of redox peaks in the cyclic voltammograms,” *Electrochimica Acta*, vol. 46, no. 26-27, pp. 4007–4015, 2001.
- [97] R. Noriega, J. Rivnay, K. Vandewal, F. P. V. Koch, N. Stingelin, P. Smith, M. F. Toney, and A. Salleo, “A general relationship between disorder, aggregation and charge transport in conjugated polymers,” *Nature Materials*, vol. 12, no. 11, pp. 1038–1044, 08 2013.
- [98] V. Untilova, T. Biskup, L. Biniek, V. Vijayakumar, and M. Brinkmann, “Control of chain alignment and crystallization helps enhance charge conductivities and thermoelectric power factors in sequentially doped p3ht:f4tcnq films,” *Macromolecules*, vol. 53, no. 7, pp. 2441–2453, 2020.

- [99] K. Gu, Y. Wang, R. Li, E. Tsai, J. W. Onorato, C. K. Luscombe, R. D. Priestley, and Y.-L. Loo, "Role of postdeposition thermal annealing on intracrystallite and intercrystallite structuring and charge transport in poly (3-hexylthiophene)," *ACS Applied Materials & Interfaces*, vol. 13, no. 1, pp. 999–1007, 2021.
- [100] G. L. Schulz and S. Ludwigs, "Controlled crystallization of conjugated polymer films from solution and solvent vapor for polymer electronics," *Advanced Functional Materials*, vol. 27, no. 1, p. 1603083, 2017.
- [101] A. Hamidi-Sakr, D. Schiefer, S. Covindarassou, L. Biniek, M. Sommer, and M. Brinkmann, "Highly oriented and crystalline films of a phenyl-substituted polythiophene prepared by epitaxy: Structural model and influence of molecular weight," *Macromolecules*, vol. 49, no. 9, pp. 3452–3462, 2016.
- [102] K. Rahimi, I. Botiz, N. Stingelin, N. Kayunkid, M. Sommer, F. P. V. Koch, H. Nguyen, O. Coulembier, P. Dubois, M. Brinkmann, and G. Reiter, "Controllable processes for generating large single crystals of poly(3-hexylthiophene)," *Angewandte Chemie, International Edition*, vol. 51, no. 44, pp. 11 131–11 135, 2012.
- [103] A. Hamidi-Sakr, L. Biniek, S. Fall, and M. Brinkmann, "Precise control of lamellar thickness in highly oriented regioregular poly(3-hexylthiophene) thin films prepared by high-temperature rubbing: Correlations with optical properties and charge transport," *Advanced Functional Materials*, vol. 26, no. 3, pp. 408–420, 2016.
- [104] M. Brinkmann and P. Rannou, "Molecular weight dependence of chain packing and semicrystalline structure in oriented films of regioregular poly (3-hexylthiophene) revealed by high-resolution transmission electron microscopy," *Macromolecules*, vol. 42, no. 4, pp. 1125–1130, 2009.
- [105] T. Djuric, G. Hernandez-Sosa, G. Schwabegger, M. Koini, G. Hesser, M. Arndt, M. Brinkmann, H. Sitter, C. Simbrunner, and R. Resel, "Alternately deposited heterostructures of α -sexithiophene–para-hexaphenyl on muscovite mica(001) surfaces: crystallographic structure and morphology," *Journal of Materials Chemistry*, vol. 22, no. 30, p. 15316, 2012.
- [106] G. Schwabegger, F. Quochi, G. Hernandez-Sosa, T. Djuric, G. Bongiovanni, A. Vollmer, M. Oehzelt, I. Salzmann, R. Resel, N. Koch *et al.*, "White fluorescent nano-fibers prepared by periodic organic hetero-epitaxy," in *Optical Processes in Organic Materials and Nanostructures II*, vol. 8827. SPIE, 2013, pp. 22–28.
- [107] C. Simbrunner, "Epitaxial growth of sexi-thiophene and para-hexaphenyl and its implications for the fabrication of self-assembled lasing nano-fibres," *Semiconductor Science and Technology*, vol. 28, no. 5, p. 31, 2013.
- [108] C. Simbrunner, G. Hernandez-Sosa, M. Oehzelt, R. Resel, F. Quochi, D. Nabok, T. Djuric, L. Romaner, P. Puschnig, C. Draxl, I. Salzmann, G. Schwabegger, I. Watzinger, M. Saba, A. Mura, G. Bongiovanni, and H. Sitter, *Organic–Organic Heteroepitaxy—The Method of Choice to Tune Optical Emission of Organic Nano-fibers?*,

- ser. Springer Series in Materials Science. Berlin, Heidelberg: Springer, 2013, vol. 173, pp. 49–78.
- [109] G. Schwabegger, M. Oehzelt, I. Salzmann, F. Quochi, M. Saba, A. Mura, G. Bongiovanni, A. Vollmer, N. Koch, H. Sitter, and C. Simbrunner, “[Interface Properties of Organic *para*-Hexaphenyl/ \$\alpha\$ -Sexithiophene Heterostructures Deposited on Highly Oriented Pyrolytic Graphite](#),” *Langmuir*, vol. 29, no. 47, pp. 14 444–14 450, 2013.
- [110] F. Quochi, G. Schwabegger, C. Simbrunner, F. Floris, M. Saba, A. Mura, H. Sitter, and G. Bongiovanni, “[Extending the lasing wavelength coverage of organic semiconductor nanofibers by periodic organic-organic heteroepitaxy](#),” *Advanced Optical Materials*, vol. 1, no. 2, pp. 117–122, 2013.
- [111] L. Tavares, M. Cadelano, F. Quochi, C. Simbrunner, G. Schwabegger, M. Saba, A. Mura, G. Bongiovanni, D. A. D. S. Filho, W. F. Da Cunha, H.-G. Rubahn, and J. Kjelstrup-Hansen, “[Efficient Exciton Diffusion and Resonance-Energy Transfer in Multilayered Organic Epitaxial Nanofibers](#),” *The Journal of Physical Chemistry C*, vol. 119, no. 27, pp. 15 689–15 697, 2015.
- [112] J. O. Vogel, I. Salzmann, S. Duhm, M. Oehzelt, J. P. Rabe, and N. Koch, “[Phase-separation and mixing in thin films of co-deposited rod-like conjugated molecules](#),” *Journal of Materials Chemistry*, vol. 20, no. 20, pp. 4055–4066, 2010.
- [113] M. Pope and C. E. Swenberg, *Electronic processes in organic crystals and polymers*. Oxford University Press, 1999.
- [114] A. J. Heeger, “[Semiconducting and Metallic Polymers: The Fourth Generation of Polymeric Materials \(Nobel Lecture\)](#),” *Angewandte Chemie International Edition*, vol. 40, pp. 2591–2611, 2001.
- [115] V. Coropceanu, J. Cornil, D. A. da Silva Filho, Y. Olivier, R. Silbey, and J.-L. Brédas, “Charge transport in organic semiconductors,” *Chemical reviews*, vol. 107, no. 4, pp. 926–952, 2007.
- [116] M. Mas-Torrent and C. Rovira, “Role of molecular order and solid-state structure in organic field-effect transistors,” *Chemical reviews*, vol. 111, no. 8, pp. 4833–4856, 2011.
- [117] O. D. Jurchescu, D. A. Mourey, S. Subramanian, S. R. Parkin, B. M. Vogel, J. E. Anthony, T. N. Jackson, and D. J. Gundlach, “Effects of polymorphism on charge transport in organic semiconductors,” *Physical Review B—Condensed Matter and Materials Physics*, vol. 80, no. 8, p. 085201, 2009.
- [118] P. W. Atkins and R. S. Friedman, *Molecular quantum mechanics*. Oxford University Press, USA, 2011.
- [119] W. Demtröder, *Molecular physics: theoretical principles and experimental methods*. John Wiley & Sons, 2008.

- [120] J.-L. Brédas, S. R. Marder, and J.-M. André, "An introduction to the electronic structure of π -conjugated molecules and polymers, and to the concept of electronic bands," in *THE WSPC REFERENCE ON ORGANIC ELECTRONICS: ORGANIC SEMICONDUCTORS: Basic Concepts*. World Scientific, 2016, pp. 1–18.
- [121] L. Alcácer, *Electronic structure of organic semiconductors: polymers and small molecules*. Morgan & Claypool Publishers, 2018.
- [122] J.-L. Bredas, "Mind the gap!" *Materials Horizons*, vol. 1, no. 1, pp. 17–19, 2014.
- [123] R. E. Peierls, *Quantum theory of solids*. Clarendon Press, 1996.
- [124] D. L. Pavia, G. M. Lampman, G. S. Kriz, J. R. Vyvyan *et al.*, *Introduction to spectroscopy*. Cengage learning Stamford, CT, 2015.
- [125] B. Valeur and M. N. Berberan-Santos, *Molecular fluorescence: principles and applications*. John Wiley & Sons, 2013.
- [126] M. Kasha, "Characterization of electronic transitions in complex molecules," *Discussions of the Faraday society*, vol. 9, pp. 14–19, 1950.
- [127] J. R. Lakowicz and B. R. Masters, "Principles of fluorescence spectroscopy," *Journal of Biomedical Optics*, vol. 13, no. 2, p. 029901, 2008.
- [128] P. A. M. Dirac, "The quantum theory of the emission and absorption of radiation," *Proceedings of the Royal Society of London. Series A, Containing Papers of a Mathematical and Physical Character*, vol. 114, no. 767, pp. 243–265, 1927.
- [129] E. Fermi, *Nuclear physics: a course given by Enrico Fermi at the University of Chicago*. University of Chicago press, 1950.
- [130] M. Kasha, H. R. Rawls, and M. Ashraf El-Bayoumi, "The exciton model in molecular spectroscopy," *Pure and Applied Chemistry VIIIth*, vol. 11, no. 3-4, pp. 371–392, 1965.
- [131] M. Kasha, "Energy transfer mechanisms and the molecular exciton model for molecular aggregates," *Radiation research*, vol. 20, no. 1, pp. 55–70, 1963.
- [132] —, "Relation between exciton bands and conduction bands in molecular lamellar systems," *Reviews of Modern Physics*, vol. 31, no. 1, p. 162, 1959.
- [133] E. G. McRae and M. Kasha, "Enhancement of phosphorescence ability upon aggregation of dye molecules," *The Journal of Chemical Physics*, vol. 28, no. 4, pp. 721–722, 1958.
- [134] N. J. Hestand and F. C. Spano, "[Expanded theory of h-and j-molecular aggregates: the effects of vibronic coupling and intermolecular charge transfer](#)," *Chemical Reviews*, vol. 118, no. 15, pp. 7069–7163, 2018.

- [135] A. S. Davydov, "Theory of molecular excitons," *Theory of Molecular Excitons*, p. 18, 1971.
- [136] M. Kasha, "Characterization of electronic transitions in complex molecules," *Discussions of the Faraday society*, vol. 9, pp. 14–19, 1950.
- [137] E. E. Jelley, "Spectral absorption and fluorescence of dyes in the molecular state," *Nature*, vol. 138, no. 3502, pp. 1009–1010, 1936.
- [138] ———, "Molecular, nematic and crystal states of i: I-diethyl-cyanine chloride," *Nature*, vol. 139, no. 3519, pp. 631–631, 1937.
- [139] G. Scheibe, L. Kandler, and H. Ecker, "Polymerisation und polymere adsorption als ursache neuartiger absorptionsbanden von organischen farbstoffen," *Naturwissenschaften*, vol. 25, no. 5, pp. 75–75, 1937.
- [140] I. Salzmann, G. Heimel, S. Duhm, M. Oehzelt, P. Pingel, B. M. George, A. Schnegg, K. Lips, R.-P. Blum, A. Vollmer, and N. Koch, "[Intermolecular Hybridization Governs Molecular Electrical Doping](#)," *Physical Review Letters*, vol. 108, p. 035502, 2012.
- [141] S.-i. Machida, Y. Nakayama, S. Duhm, Q. Xin, A. Funakoshi, N. Ogawa, S. Kera, N. Ueno, and H. Ishii, "Highest-occupied-molecular-orbital band dispersion of rubrene single crystals as observed by angle-resolved ultraviolet photoelectron spectroscopy," *Physical review letters*, vol. 104, no. 15, p. 156401, 2010.
- [142] J. Rivnay, S. C. Mannsfeld, C. E. Miller, A. Salleo, and M. F. Toney, "Quantitative determination of organic semiconductor microstructure from the molecular to device scale," *Chemical reviews*, vol. 112, no. 10, pp. 5488–5519, 2012.
- [143] H. Bässler, "[Charge Transport in Disordered Organic Photoconductors a Monte Carlo Simulation Study](#)," *physica status solidi (b)*, vol. 175, pp. 15–56, 1993.
- [144] V. Podzorov, E. Menard, A. Borissov, V. Kiryukhin, J. A. Rogers, and M. Gershenson, "Intrinsic charge transport on the surface of organic semiconductors," *Physical review letters*, vol. 93, no. 8, p. 086602, 2004.
- [145] J. Rivnay, R. Noriega, J. E. Northrup, R. J. Kline, M. F. Toney, and A. Salleo, "Structural origin of gap states in semicrystalline polymers and the implications for charge transport," *American Physical Society*, vol. 83, no. 12, 03 2011.
- [146] H. Bässler, D. Kroh, F. Schauer, V. Nádaždy, and A. Köhler, "Mapping the density of states distribution of organic semiconductors by employing energy resolved-electrochemical impedance spectroscopy," *Advanced Functional Materials*, vol. 31, no. 9, p. 2007738, 2021.
- [147] H. F. Haneef, A. M. Zeidell, and O. D. Jurchescu, "Charge carrier traps in organic semiconductors: a review on the underlying physics and impact on electronic devices," *Journal of Materials Chemistry C*, vol. 8, no. 3, pp. 759–787, 2020.

- [148] S. Olthof, S. Mehraeen, S. K. Mohapatra, S. Barlow, V. Coropceanu, J.-L. Brédas, S. R. Marder, and A. Kahn, "Ultralow doping in organic semiconductors: evidence of trap filling," *Physical review letters*, vol. 109, no. 17, p. 176601, 2012.
- [149] W. L. Kalb, S. Haas, C. Krellner, T. Mathis, and B. Batlogg, "Trap density of states in small-molecule organic semiconductors: A quantitative comparison of thin-film transistors with single crystals," *Physical Review B—Condensed Matter and Materials Physics*, vol. 81, no. 15, p. 155315, 2010.
- [150] A. Salleo, T. Chen, A. Völkel, Y. Wu, P. Liu, B. Ong, and R. Street, "Intrinsic hole mobility and trapping in a regioregular poly (thiophene)," *Physical Review B—Condensed Matter and Materials Physics*, vol. 70, no. 11, p. 115311, 2004.
- [151] O. Zapata-Arteaga, B. Dorling, A. Perevedentsev, J. Martín, J. S. Reparaz, and M. Campoy-Quiles, "Closing the stability–performance gap in organic thermoelectrics by adjusting the partial to integer charge transfer ratio," *Macromolecules*, vol. 53, no. 2, pp. 609–620, 2020.
- [152] A. Babuji, A. Cazorla, E. Solano, C. Habenicht, H. Kleemann, C. Ocal, K. Leo, and E. Barrena, "Charge-transfer complexes in organic field-effect transistors: Superior suitability for surface doping," *ACS applied materials & interfaces*, vol. 14, no. 39, pp. 44 632–44 641, 2022.
- [153] M. Cui, H. Rui, X. Wu, Z. Sun, W. Qu, W. Qin, and S. Yin, "Coexistent integer charge transfer and charge transfer complex in f4-tcnq-doped ptaa for efficient flexible organic light-emitting diodes," *The Journal of Physical Chemistry Letters*, vol. 12, no. 35, pp. 8533–8540, 2021.
- [154] H. Hase, K. O'Neill, J. Frisch, A. Opitz, N. Koch, and I. Salzmänn, "[Unraveling the microstructure of molecularly doped poly\(3-hexylthiophene\) by thermally induced dedoping](#)," *The Journal of Physical Chemistry C*, vol. 122, pp. 25 893–25 899, 2018.
- [155] M. Meneghetti and C. Pecile, "Charge–transfer organic crystals: Molecular vibrations and spectroscopic effects of electron–molecular vibration coupling of the strong electron acceptor TCNQF₄," *The Journal of Chemical Physics*, vol. 84, pp. 4149–4162, 1986.
- [156] N. L. Haworth, J. Lu, N. Vo, T. H. Le, C. D. Thompson, A. M. Bond, and L. L. Martin, "Diagnosis of the Redox Levels of TCNQF₄ Compounds Using Vibrational Spectroscopy," *ChemPlusChem*, vol. 79, pp. 962–972, 2014.
- [157] E. Kamar and O. Neilands, "[Degree of Charge Transfer in Donor–Acceptor Systems of the \$\pi\$ – \$\pi\$ Type](#)," *Russian Chemical Reviews*, vol. 55, pp. 334–342, 1986.
- [158] M. Berteau-Rainville, E. Orgiu, and I. Salzmänn, "On validity and limits of deducing the degree of charge transfer from shifts of cyano vibrations," *Electronic Structure*, vol. 5, no. 3, p. 034002, 2023.

- [159] S. Kowarik, A. Gerlach, and F. Schreiber, "Organic molecular beam deposition: fundamentals, growth dynamics, and in situ studies," *Journal of Physics: Condensed Matter*, vol. 20, no. 18, p. 184005, 2008.
- [160] J. Venables, G. Spiller, and M. Hanbucken, "Nucleation and growth of thin films," *Reports on progress in physics*, vol. 47, no. 4, p. 399, 1984.
- [161] T. Derrien, A. Lauritzen, P. Kaienburg, J. Hardigree, C. Nicklin, and M. Riede, "In situ observations of the growth mode of vacuum-deposited α -sexithiophene," *The Journal of Physical Chemistry C*, vol. 124, no. 22, pp. 11 863–11 869, 2020.
- [162] E. Ghanbari, T. Wagner, and P. Zeppenfeld, "Layer-resolved evolution of organic thin films monitored by photoelectron emission microscopy and optical reflectance spectroscopy," *The Journal of Physical Chemistry C*, vol. 119, no. 42, pp. 24 174–24 181, 2015.
- [163] R. Resel, "[Crystallographic studies on hexaphenyl thin films — a review](#)," *Thin Solid Films*, vol. 433, no. 1-2, pp. 1–11, 2003.
- [164] P. Kebarle and L. Tang, "[From ions in solution to ions in the gas phase-the mechanism of electrospray mass spectrometry](#)," *Analytical Chemistry*, vol. 65, pp. 972A–986A, 1993.
- [165] P. Kebarle and U. H. Verkerk, "[Electrospray: from ions in solution to ions in the gas phase, what we know now](#)," *Mass Spectrometry Reviews*, vol. 28, pp. 898–917, 2009.
- [166] G. Taylor, "Disintegration of water drops in an electric field," *Proceedings of the Royal Society of London. Series A. Mathematical and Physical Sciences*, vol. 280, pp. 383–397, 1964.
- [167] M. Birkholz, *Thin Film Analysis by X-Ray Scattering*. Wiley-VCH Verlag GmbH & Co. KGaA, 2006, vol. 252.
- [168] I. K. Robinson and D. J. Tweet, "[Surface X-ray diffraction](#)," *Reports on Progress in Physics*, vol. 55, no. 5, pp. 599–651, 1992.
- [169] M. Neuschitzer, A. Moser, A. Neuhold, J. Kraxner, B. Stadlober, M. Oehzelt, I. Salzmann, R. Resel, and J. Novak, "Grazing-incidence in-plane x-ray diffraction on ultra-thin organic films using standard laboratory equipment," *Journal of Applied Crystallography*, vol. 45, no. 2, pp. 367–370, 2012.
- [170] P. Dutta, "Grazing incidence x-ray diffraction," *Current Science*, pp. 1478–1483, 2000.
- [171] S. C. B. Mannsfeld, A. Virkar, C. Reese, M. F. Toney, and Z. N. Bao, "[Precise structure of pentacene monolayers on amorphous silicon oxide and relation to charge transport](#)," *Advanced Materials*, vol. 21, no. 22, pp. 2294–+, 2009.

- [172] A. Moser, *Crystal structure solution based on grazing incidence X-ray diffraction: software development and application to organic films*. In: Physics, (Graz: Graz University of Technology), 2012.
- [173] B. Schrode, S. Pachmajer, M. Dohr, C. Röthel, J. Domke, T. Fritz, R. Resel, and O. Werzer, “[Gidvis : a comprehensive software tool for geometry-independent grazing-incidence x-ray diffraction data analysis and pole-figure calculations](#),” *Journal of Applied Crystallography*, vol. 52, no. 3, pp. 683–689, 2019.
- [174] W. Kemp, *Organic spectroscopy*. Bloomsbury Publishing, 2017.
- [175] D. Oelkrug, H.-J. Egelhaaf, D. Worrall, and F. Wilkinson, “[Fluorescence yields and molecular orientation of thin organic films: Vapor-deposited oligothiophenes](#),” *Journal of Fluorescence*, vol. 5, no. 2, pp. 165–170, 1995.
- [176] M. Dramićanin, “Luminescence: the basics, methods, and instrumentation,” *Dramićanin, M., Woodhead Publishing*, pp. 33–61, 2018.
- [177] P. R. Griffiths and J. A. De Haseth, *Fourier Transform Infrared Spectrometry*. John Wiley & Sons, 2007.
- [178] T. A. Hoffard, C. A. Kodres, D. R. Polly, and N. F. E. S. C. P. H. CA, “Grazing-angle fourier transform infrared spectroscopy for online surface cleanliness verification. year 1,” 2000.
- [179] G. Haugstad, *Atomic force microscopy: understanding basic modes and advanced applications*. John Wiley & Sons, 2012.
- [180] P. Eaton and P. West, *Atomic force microscopy*. Oxford university press, 2010.
- [181] G. J. Leggett, “Scanning probe microscopy,” *Surface Analysis—The Principal Techniques*, p. 479, 2009.
- [182] W. Zhao, J. Ding, Y. Zou, C.-a. Di, and D. Zhu, “[Chemical doping of organic semiconductors for thermoelectric applications](#),” *Chemical Society Reviews*, vol. 49, pp. 7210–7228, 2020.
- [183] X. Zhao and W. Deng, “[Printing photovoltaics by electrospray](#),” *Opto-Electronic Advances*, vol. 3, pp. 190 038–1–190 038–21, 2020.
- [184] S. Lee, H. Kim, and Y. Kim, “[Progress in organic semiconducting materials with high thermal stability for organic light-emitting devices](#),” *InfoMat*, vol. 3, no. 1, pp. 61–81, 2021.
- [185] Y. Sun, Y. Zhang, Q. Liang, Y. Zhang, H. Chi, Y. Shi, and D. Fang, “Solvent inkjet printing process for the fabrication of polymer solar cells,” *RSC Advances*, vol. 3, no. 30, pp. 11 925–11 934, 2013.

- [186] R. Søndergaard, M. Hösel, D. Angmo, T. T. Larsen-Olsen, and F. C. Krebs, “Roll-to-roll fabrication of polymer solar cells,” *Materials Today*, vol. 15, no. 1-2, pp. 36–49, 2012.
- [187] G. W. Kim, E. H. Kwon, M. Kim, and Y. D. Park, “Uniform and reliable dip-coated conjugated polymers for organic transistors as obtained by solvent vapor annealing,” *The Journal of Physical Chemistry C*, vol. 123, no. 37, pp. 23 255–23 263, 2019.
- [188] C.-C. Chang, C.-L. Pai, W.-C. Chen, and S. A. Jenekhe, “Spin coating of conjugated polymers for electronic and optoelectronic applications,” *Thin Solid Films*, vol. 479, no. 1, pp. 254–260, 2005.
- [189] L. Miozzo, A. Yassar, and G. Horowitz, “Surface engineering for high performance organic electronic devices: the chemical approach,” *Journal of Materials Chemistry*, vol. 20, pp. 2513–2538, 2010.
- [190] G. Heimel, S. Duhm, I. Salzmann, A. Gerlach, A. Strozecka, J. Niederhausen, C. Burkner, T. Hosokai, I. Fernandez-Torrente, G. Schulze, S. Winkler, A. Wilke, R. Schlesinger, J. Frisch, B. Broker, A. Vollmer, B. Detlefs, J. Pflaum, S. Kera, K. J. Franke, N. Ueno, J. I. Pascual, F. Schreiber, and N. Koch, “Charged and metallic molecular monolayers through surface-induced aromatic stabilization,” *Nature Chemistry*, vol. 5, no. 3, pp. 187–194, 2013.
- [191] C. D. Dimitrakopoulos, A. R. Brown, and A. Pomp, “Molecular beam deposited thin films of pentacene for organic field effect transistor applications,” *Journal of Applied Physics*, vol. 80, no. 4, pp. 2501–2508, 1996.
- [192] J. N. O’Shea, J. B. Taylor, J. C. Swarbrick, G. Magnano, L. C. Mayor, and K. Schulte, “Electrospray deposition of carbon nanotubes in vacuum,” *Nanotechnology*, vol. 18, no. 3, p. 035707, 2007.
- [193] R. H. Temperton, J. N. O’Shea, and D. J. Scurr, “On the suitability of high vacuum electrospray deposition for the fabrication of molecular electronic devices,” *Chemical Physics Letters*, vol. 682, pp. 15–19, 2017.
- [194] S. Kowarik, A. Gerlach, A. Hinderhofer, S. Milita, F. Borgatti, F. Zontone, T. Suzuki, F. Biscarini, and F. Schreiber, “Structure, morphology, and growth dynamics of perfluoro-pentacene thin films,” *physica status solidi (RRL) – Rapid Research Letters*, vol. 2, no. 3, pp. 120–122, 2008.
- [195] L. Biniek, S. Pouget, D. Djurado, E. Gonthier, K. Tremel, N. Kayunkid, E. Zaborova, N. Crespo-Monteiro, O. Boyron, N. Leclerc *et al.*, “High-temperature rubbing: a versatile method to align π -conjugated polymers without alignment substrate,” *Macromolecules*, vol. 47, no. 12, pp. 3871–3879, 2014.
- [196] J. Y. Oh, M. Shin, T. I. Lee, W. S. Jang, Y. Min, J.-M. Myoung, H. K. Baik, and U. Jeong, “Self-seeded growth of poly (3-hexylthiophene)(p3ht) nanofibrils by a cycle of cooling and heating in solutions,” *Macromolecules*, vol. 45, no. 18, pp. 7504–7513, 2012.

- [197] S. Förster and W. Widdra, “Structure of single polythiophene molecules on au(001) prepared by in situ uhv electrospray deposition,” *Journal of Chemical Physics*, vol. 141, no. 5, p. 054713, 2014.
- [198] L. Rayleigh, “Xx. on the equilibrium of liquid conducting masses charged with electricity,” *The London, Edinburgh, and Dublin Philosophical Magazine and Journal of Science*, vol. 14, pp. 184–186, 1882.
- [199] S. Ludwigs, *P3HT Revisited: From Molecular Scale to Solar Cell Devices*, ser. Advances in Polymer Science. Springer, 2014, vol. 265.
- [200] M. Brinkmann, “Insights into the structural complexity of semi-crystalline polymer semiconductors: electron diffraction contributions,” *Materials Chemistry Frontiers*, vol. 4, pp. 1916–1929, 2020.
- [201] D. Alberga, A. Perrier, I. Ciofini, G. F. Mangiatordi, G. Lattanzi, and C. Adamo, “Morphological and charge transport properties of amorphous and crystalline p3ht and pbttt: insights from theory,” *Physical Chemistry Chemical Physics*, vol. 17, pp. 18742–18750, 2015.
- [202] K. Xian, Y. Liu, J. Liu, J. Yu, Y. Xing, Z. Peng, K. Zhou, M. Gao, W. Zhao, G. Lu, J. Zhang, J. Hou, Y. Geng, and L. Ye, “Delicate crystallinity control enables high-efficiency p3ht organic photovoltaic cells,” *Journal of Materials Chemistry A*, vol. 10, pp. 3418–3429, 2022.
- [203] H. Sirringhaus, P. J. Brown, R. H. Friend, M. M. Nielsen, K. Bechgaard, B. M. W. Langeveld-Voss, A. J. H. Spiering, R. A. J. Janssen, E. W. Meijer, P. Herwig, and D. M. de Leeuw, “Two-dimensional charge transport in self-organized, high-mobility conjugated polymers,” *Nature*, vol. 401, no. 6754, pp. 685–688, 1999.
- [204] A. Assadi, C. Svensson, M. Willander, and O. Inganäs, “Field-effect mobility of poly(3-hexylthiophene),” *Applied Physics Letters*, vol. 53, no. 3, pp. 195–197, 1988.
- [205] S. K. Sharma, R. Singhal, B. Malhotra, N. Sehgal, and A. Kumar, “Langmuir–blodgett film based biosensor for estimation of galactose in milk,” *Electrochimica Acta*, vol. 49, no. 15, pp. 2479–2485, 2004.
- [206] H. Runfang, Y. Yangfan, L. Leilei, J. Jianlong, Z. Qiang, D. Lifeng, S. Shengbo, and L. Qiang, “P3ht-based organic field effect transistor for low-cost, label-free detection of immunoglobulin g,” *Journal of Biotechnology*, vol. 359, pp. 75–81, 2022.
- [207] R. Meitzner, T. Faber, S. Alam, A. Amand, R. Roesch, M. Büttner, F. Herrmann-Westendorf, M. Presselt, L. Ciammaruchi, I. Visoly-Fisher, S. Veenstra, A. Diaz de Zerio, X. Xu, E. Wang, C. Müller, P. Troshin, M. D. Hager, S. Köhn, M. Duszka, M. Krassas, S. Züfle, E. Kymakis, E. A. Katz, S. Berson, F. Granek, M. Manceau, F. Brunetti, G. Polino, U. S. Schubert, M. Lira-Cantu, and H. Hoppe, “Impact of p3ht materials properties and layer architecture on opv device stability,” *Solar Energy Materials and Solar Cells*, vol. 202, p. 110151, 2019.

- [208] S. Holliday, R. S. Ashraf, A. Wadsworth, D. Baran, S. A. Yousaf, C. B. Nielsen, C.-H. Tan, S. D. Dimitrov, Z. Shang, N. Gasparini, M. Alamoudi, F. Laquai, C. J. Brabec, A. Salleo, J. R. Durrant, and I. McCulloch, “[High-efficiency and air-stable p3ht-based polymer solar cells with a new non-fullerene acceptor](#),” *Nature Communications*, vol. 7, no. 1, p. 11585, 2016.
- [209] J. V. Iribarne and B. A. Thomson, “[On the evaporation of small ions from charged droplets](#),” *Journal of Chemical Physics*, vol. 64, no. 6, pp. 2287–2294, 1976.
- [210] C.-L. Pai, M. C. Boyce, and G. C. Rutledge, “Morphology of porous and wrinkled fibers of polystyrene electrospun from dimethylformamide,” *Macromolecules*, vol. 42, no. 6, pp. 2102–2114, 2009.
- [211] B. Almería, W. Deng, T. M. Fahmy, and A. Gomez, “Controlling the morphology of electro-spray-generated plga microparticles for drug delivery,” *Journal of Colloid and Interface Science*, vol. 343, no. 1, pp. 125–133, 2010.
- [212] M. H. Amad, N. B. Cech, G. S. Jackson, and C. G. Enke, “Importance of gas-phase proton affinities in determining the electro-spray ionization response for analytes and solvents,” *Journal of Mass Spectrometry*, vol. 35, no. 7, pp. 784–789, 2000.
- [213] M. Ali, M. Abbas, S. K. Shah, E. Bontempi, P. Colombi, A. Di Cicco, and R. Gunnella, “[Variability of physical characteristics of electro-sprayed poly\(3-hexylthiophene\) thin films](#),” *Journal of Applied Physics*, vol. 110, no. 5, p. 054515, 2011.
- [214] H. Hu, K. Zhao, N. J. Fernandes, P. Boufflet, J. Bannock, L. Yu, J. Mello, N. Stingelin, M. Heeney, E. Giannelis, and A. Amassian, “Entanglements in marginal solutions: a means of tuning pre-aggregation of conjugated polymers with positive implications for charge transport,” *Journal of Materials Chemistry*, vol. 3, pp. 7394–7404, 2015.
- [215] E. W. Aldrich and D. W. Querfeld, “Freezing and boiling points of the ternary system ethanol-methanol-water,” *Industrial & Engineering Chemistry*, vol. 23, no. 6, pp. 708–711, 1931.
- [216] N. Bock, T. R. Dargaville, and M. A. Woodruff, “Electrospraying of polymers with therapeutic molecules: State of the art,” *Progress in Polymer Science*, vol. 37, no. 11, pp. 1510–1551, 2012.
- [217] M. G. Ikonou, A. T. Blades, and P. Kebarle, “Electrospray mass spectrometry of methanol and water solutions suppression of electric discharge with sf6 gas,” *Journal of the American Society for Mass Spectrometry*, vol. 2, pp. 497–505, 1991.
- [218] A. T. Blades, M. G. Ikonou, and P. Kebarle, “[Mechanism of electro-spray mass spectrometry. electro-spray as an electrolysis cell](#),” *Analytical Chemistry*, vol. 63, pp. 2109–2114, 1991.

- [219] J. K. Keum, K. Xiao, I. N. Ivanov, K. Hong, J. F. Browning, G. S. Smith, M. Shao, K. C. Littrell, A. J. Rondinone, E. A. Payzant, J. Chen, and D. K. Hensley, "Solvent quality-induced nucleation and growth of parallelepiped nanorods in dilute poly (3-hexylthiophene)(p3ht) solution and the impact on the crystalline morphology of solution-cast thin film," *CrystEngComm*, vol. 15, no. 6, pp. 1114–1124, 2013.
- [220] M. Roesing, J. Howell, and D. Boucher, "Solubility characteristics of poly (3-hexylthiophene)," *Journal of Polymer Science Part B: Polymer Physics*, vol. 55, no. 14, pp. 1075–1087, 2017.
- [221] S. Rughooputh, S. Hotta, A. Heeger, and F. Wudl, "Chromism of soluble polythienylenes," *Journal of Polymer Science Part B: Polymer Physics*, vol. 25, no. 5, pp. 1071–1078, 1987.
- [222] P. J. Brown, D. S. Thomas, A. Köhler, J. S. Wilson, J.-S. Kim, C. M. Ramsdale, H. Sirringhaus, and R. H. Friend, "Effect of interchain interactions on the absorption and emission of poly (3-hexylthiophene)," *Physical Review B*, vol. 67, no. 6, p. 064203, 2003.
- [223] N. Kayunkid, S. Uttiya, and M. Brinkmann, "[Structural model of regioregular poly\(3-hexylthiophene\) obtained by electron diffraction analysis](#)," *Macromolecules*, vol. 43, no. 11, pp. 4961–4967, 2010.
- [224] N. Murthy and H. Minor, "[General procedure for evaluating amorphous scattering and crystallinity from x-ray diffraction scans of semicrystalline polymers](#)," *Polymer*, vol. 31, no. 6, pp. 996–1002, 1990.
- [225] J. Mårdalen, E. J. Samuelsen, O. R. Gautun, and P. H. Carlsen, "X-ray scattering from oriented poly (3-alkylthiophenes)," *Synthetic Metals*, vol. 48, no. 3, pp. 363–380, 1992.
- [226] J. Mårdalen, E. J. Samuelsen, and A. Ø. Pedersen, "The nucleation process and the crystalline structure of poly (3-alkylthiophenes) precipitated from marginal solvents," *Synthetic Metals*, vol. 55, no. 1, pp. 378–383, 1993.
- [227] T. Wu, S. Chandran, Y. Zhang, T. Zheng, T. Pfohl, J. Xu, and G. Reiter, "[Primary nucleation in metastable solutions of poly\(3-hexylthiophene\)](#)," *Macromolecules*, vol. 55, no. 8, pp. 3325–3334, 2022.
- [228] S. Joshi, P. Pingel, S. Grigorian, T. Panzner, U. Pietsch, D. Neher, M. Forster, and U. Scherf, "[Bimodal temperature behavior of structure and mobility in high molecular weight p3ht thin films](#)," *Macromolecules*, vol. 42, no. 13, pp. 4651–4660, 2009.
- [229] R. Peng, J. Zhu, W. Pang, Q. Cui, F. Wu, K. Liu, M. Wang, and G. Pan, "Thermal annealing effects on the absorption and structural properties of regioregular poly (3-hexylthiophene) films," *Journal of Macromolecular Science, Part B*, vol. 50, no. 3, pp. 624–636, 2011.

- [230] R. D. Deegan, O. Bakajin, T. F. Dupont, G. Huber, S. R. Nagel, and T. A. Witten, “Capillary flow as the cause of ring stains from dried liquid drops,” *Nature*, vol. 389, pp. 827–829, 1997.
- [231] R. D. Deegan, “Pattern formation in drying drops,” *Physical review E*, vol. 61, p. 475, 2000.
- [232] E. Bodnár, J. Grifoll, and J. Rosell-Llompart, “Polymer solution electrospraying: A tool for engineering particles and films with controlled morphology,” *Journal of Aerosol Science*, vol. 125, pp. 93–118, 2018.
- [233] C. H. Park and J. Lee, “Electrosprayed polymer particles: effect of the solvent properties,” *Journal of Applied Polymer Science*, vol. 114, no. 1, pp. 430–437, 2009.
- [234] B. Mahaling and D. S. Katti, “Fabrication of micro-structures of poly [(r)-3-hydroxybutyric acid] by electro-spraying/-spinning: understanding the influence of polymer concentration and solvent type,” *Journal of Materials Science*, vol. 49, no. 12, pp. 4246–4260, 2014.
- [235] W. Graupner, G. Grem, F. Meghdadi, C. Paar, G. Leising, U. Scherf, K. Müllen, W. Fischer, and F. Stelzer, “Electroluminescence with conjugated polymers and oligomers,” *Molecular Crystals and Liquid Crystals*, vol. 256, no. 1, pp. 549–554, 1994.
- [236] E. Zojer, N. Koch, P. Puschnig, F. Meghdadi, A. Niko, R. Resel, C. Ambrosch-Draxl, M. Knupfer, J. Fink, J. L. Bredas, and G. Leising, “Structure, morphology, and optical properties of highly ordered films of para-sexiphenyl,” *Physical Review B*, vol. 61, no. 24, pp. 16 538–16 549, 2000.
- [237] S. Tasch, C. Brandstatter, F. Meghdadi, G. Leising, G. Froyer, and L. Athouel, “Red-green-blue light emission from a thin film electroluminescence device based on parahexaphenyl,” *Advanced Materials*, vol. 9, no. 1, pp. 33–36, 1997.
- [238] G. D’Avino, L. Muccioli, and C. Zannoni, “From chiral islands to smectic layers: A computational journey across sexithiophene morphologies on c-60,” *Advanced Functional Materials*, vol. 25, no. 13, pp. 1985–1995, 2015.
- [239] L. Bormann, F. Nehm, N. Weiß, V. C. Nikolis, F. Selzer, A. Eychmüller, L. Müller-Meskamp, K. Vandewal, and K. Leo, “Degradation of sexithiophene cascade organic solar cells,” *Advanced Energy Materials*, vol. 6, p. 1502432, 2016.
- [240] K. Cnops, B. P. Rand, D. Cheyns, B. Verreert, M. A. Empl, and P. Heremans, “8.4% efficient fullerene-free organic solar cells exploiting long-range exciton energy transfer,” *Nature Communications*, vol. 5, no. 1, p. 3406, 2014.
- [241] M. Halik, H. Klauk, U. Zschieschang, G. Schmid, S. Ponomarenko, S. Kirchmeyer, and W. Weber, “Relationship between molecular structure and electrical performance of oligothiophene organic thin film transistors,” *Advanced Materials*, vol. 15, no. 11, pp. 917–922, 2003.

- [242] A. Dodabalapur, L. Torsi, and H. E. Katz, “Organic transistors: two-dimensional transport and improved electrical characteristics,” *Science*, vol. 268, no. 5208, pp. 270–271, 1995.
- [243] G. Horowitz, F. Deloffre, F. Garnier, R. Hajlaoui, M. Hmyene, and A. Yassar, “All-organic field-effect transistors made of π -conjugated oligomers and polymeric insulators,” *Synthetic Metals*, vol. 54, no. 1-3, pp. 435–445, 1993.
- [244] J. O. Vogel, I. Salzmann, R. Opitz, S. Duhm, B. Nickel, J. P. Rabe, and N. Koch, “Subnanometer control of the interlayer spacing in thin films of intercalated rodlike conjugated molecules,” *Journal of Physical Chemistry B*, vol. 111, no. 51, pp. 14 097–14 101, 2007.
- [245] S. Plimpton, “Fast parallel algorithms for short-range molecular dynamics,” *Journal of Computational Physics*, vol. 117, no. 1, pp. 1–19, 1995.
- [246] B. R. Brooks, C. L. Brooks III, A. D. Mackerell Jr., L. Nilsson, R. J. Petrella, B. Roux, Y. Won, G. Archontis, C. Bartels, S. Boresch, A. Caflisch, L. Caves, Q. Cui, A. R. Dinner, M. Feig, S. Fischer, J. Gao, M. Hodoscek, W. Im, K. Kuczera, T. Lazaridis, J. Ma, V. Ovchinnikov, E. Paci, R. W. Pastor, C. B. Post, J. Z. Pu, M. Schaefer, B. Tidor, R. M. Venable, H. L. Woodcock, X. Wu, W. Yang, D. M. York, and M. Karplus, “Charmm: The biomolecular simulation program,” *Journal of Computational Chemistry*, vol. 30, no. 10, pp. 1545–1614, 2009.
- [247] R. Resel, N. Koch, F. Meghdadi, G. Leising, L. Athouel, G. Froyer, and F. Hofer, “A Polymorph Crystal Structure of Hexaphenyl Observed in Thin Films,” *Crystal Research and Technology*, vol. 36, no. 1, pp. 47–54, 2001.
- [248] J. Fauvarque, M. Petit, A. Digua, and G. Froyer, “Electrochemical synthesis of poly(1,4-phenylene) films,” *Die Makromolekulare Chemie*, vol. 188, no. 8, pp. 1833–1839, 1987.
- [249] M. Kramer and V. Hoffmann, “Infrared spectroscopic characterization of orientation and order of thin oligothiophene films,” *Optical Materials*, vol. 9, no. 1-4, pp. 65–69, 1998.
- [250] G. Louarn, J. Buisson, S. Lefrant, and D. Fichou, “Vibrational studies of a series of alpha-oligothiophenes as model systems of polythiophene,” *The Journal of Physical Chemistry*, vol. 99, no. 29, pp. 11 399–11 404, 1995.
- [251] I. Salzmann, S. Duhm, G. Heimel, M. Oehzelt, R. Kniprath, R. L. Johnson, J. P. Rabe, and N. Koch, “Tuning the Ionization Energy of Organic Semiconductor Films: The Role of Intramolecular Polar Bonds,” *Journal of the American Chemical Society*, vol. 130, no. 39, pp. 12 870–12 871, 2008.
- [252] M. Schwarze, W. Tress, B. Beyer, F. Gao, R. Scholz, C. Poelking, K. Ortstein, A. A. Günther, D. Kasemann, D. Andrienko, and K. Leo, “Band structure engineering in organic semiconductors,” *Science*, vol. 352, no. 6292, pp. 1446–1449, 2016.

- [253] K. Broch, U. Heinemeyer, A. Hinderhofer, F. Anger, R. Scholz, A. Gerlach, and F. Schreiber, “[Optical evidence for intermolecular coupling in mixed films of pentacene and perfluoropentacene](#),” *Physical Review B*, vol. 83, no. 24, p. 245307, 2011.
- [254] K. Broch, C. Bürker, J. Dieterle, S. Krause, A. Gerlach, and F. Schreiber, “[Impact of molecular tilt angle on the absorption spectra of pentacene:perfluoropentacene blends](#),” *physica status solidi (RRL) – Rapid Research Letters*, vol. 7, no. 12, pp. 1084–1088, 2013.
- [255] I. Salzmänn, S. Duhm, G. Heimel, J. P. Rabe, N. Koch, M. Oehzelt, Y. Sakamoto, and T. Suzuki, “[Structural Order in Perfluoropentacene Thin Films and Heterostructures with Pentacene](#),” *Langmuir*, vol. 24, no. 14, pp. 7294–7298, 2008.
- [256] G. D’Avino, S. Duhm, R. G. Della Valle, G. Heimel, M. Oehzelt, S. Kera, N. Ueno, D. Beljonne, and I. Salzmänn, “[Electrostatic Interactions Shape Molecular Organization and Electronic Structure of Organic Semiconductor Blends](#),” *Chemistry of Materials*, vol. 32, no. 3, pp. 1261–1271, 2020.
- [257] A. Hinderhofer, C. Frank, T. Hosokai, A. Resta, A. Gerlach, and F. Schreiber, “[Structure and morphology of coevaporated pentacene-perfluoropentacene thin films](#),” *The Journal of Chemical Physics*, vol. 134, no. 10, p. 104702, 2011.
- [258] V. O. Kim, K. Broch, V. Belova, Y. S. Chen, A. Gerlach, F. Schreiber, H. Tamura, R. G. Della Valle, G. D’Avino, I. Salzmänn, D. Beljonne, A. Rao, and R. Friend, “[Singlet exciton fission via an intermolecular charge transfer state in coevaporated pentacene-perfluoropentacene thin films](#),” *The Journal of Chemical Physics*, vol. 151, no. 16, p. 164706, 2019.
- [259] A. Andreev, G. Matt, C. J. Brabec, H. Sitter, D. Badt, H. Seyringer, and N. Sariciftci, “[Highly anisotropically self-assembled structures of para-sexiphenyl grown by hot-wall epitaxy](#),” *Advanced Materials*, vol. 12, no. 9, pp. 629–633, 2000.
- [260] A. Niko, F. Meghdadi, C. Ambrosch-Draxl, P. Vogl, and G. Leising, “[Optical absorbance of oriented thin films](#),” *Synthetic Metals*, vol. 76, no. 1-3, pp. 177–179, 1996.
- [261] A. Niko, E. Zojer, F. Meghdadi, C. Ambrosch-Draxl, and G. Leising, “[Geometry-dependent absorption, and emission of para-hexaphenyl](#),” *Synthetic Metals*, vol. 101, no. 1-3, pp. 662–663, 1999.
- [262] F. Kouki, P. Spearman, P. Valat, G. Horowitz, and F. Garnier, “[Experimental determination of excitonic levels in \$\alpha\$ -oligothiophenes](#),” *The Journal of Chemical Physics*, vol. 113, no. 1, pp. 385–391, 2000.
- [263] K. Hamano, T. Kurata, S. Kubota, and H. Koezuka, “[Organic molecular beam deposition of \$\alpha\$ -sexithienyl](#),” *Japanese Journal of Applied Physics*, vol. 33, no. 7B, p. L1031, 1994.

- [264] R. Colditz, D. Grebner, M. Helbig, and S. Rentsch, "Theoretical studies and spectroscopic investigations of ground and excited electronic states of thiophene oligomers," *CP*, vol. 201, no. 2-3, pp. 309–320, 1995.
- [265] B. Servet, G. Horowitz, S. Ries, O. Lagorsse, P. Alnot, A. Yassar, F. Deloffre, P. Srivastava, R. Hajlaoui, P. Lang, and F. Garnier, "Polymorphism and charge-transport in vacuum-evaporated sexithiophene films," *Chemistry of Materials*, vol. 6, no. 10, pp. 1809–1815, 1994.
- [266] D. Fichou, G. Horowitz, B. Xu, and F. Garnier, "Low temperature optical absorption of polycrystalline thin films of α -quaterthiophene, α -sexithiophene and α -octithiophene, three model oligomers of polythiophene," *Synthetic Metals*, vol. 48, no. 2, pp. 167–179, 1992.
- [267] L. Blinov, S. Palto, G. Ruani, C. Taliani, A. Tevosov, S. Yudin, and R. Zamboni, "Location of charge transfer states in α -sexithienyl determined by the electroabsorption technique," *Chemical Physics Letters*, vol. 232, no. 4, pp. 401–406, 1995.
- [268] C. Taliani and W. Gebauer, *Electronic Excited States of Conjugated Oligothiophenes*, 1st ed. Wiley-VCH, 1998, pp. 361–404.
- [269] F. Garnier, G. Horowitz, P. Valat, F. Kouki, and V. Wintgens, "Stimulated emission in sexithiophene single crystals," in *Optical Probes of Conjugated Polymers*, vol. 3145. SPIE, 1997, pp. 340–349.
- [270] X. Leng, H. Yin, D. Liang, and Y. Ma, "Excitons and davydov splitting in sexithiophene from first-principles many-body green's function theory," *The Journal of Chemical Physics*, vol. 143, no. 11, p. 114501, 2015.
- [271] G. Horowitz, B. Bachet, A. Yassar, P. Lang, F. Demanze, J. L. Fave, and F. Garnier, "Growth and characterization of sexithiophene single-crystals," *Chemistry of Materials*, vol. 7, no. 7, pp. 1337–1341, 1995.
- [272] M. A. Loi, E. da Como, F. Dinelli, M. Murgia, R. Zamboni, F. Biscarini, and M. Mucini, "Supramolecular organization in ultra-thin films of α -sexithiophene on silicon dioxide," *Nature Materials*, vol. 4, no. 1, pp. 81–85, 2005.
- [273] A. Moser, I. Salzmann, M. Oehzelt, A. Neuhold, H. G. Flesch, J. Ivanco, S. Pop, T. Toader, D. R. T. Zahn, D. M. Smilgies, and R. Resel, "A disordered layered phase in thin films of sexithiophene," *Chemical Physics Letters*, vol. 574, pp. 51–55, 2013.
- [274] B. Servet, S. Ries, M. Trotel, P. Alnot, G. Horowitz, and F. Garnier, "X-ray determination of the crystal-structure and orientation of vacuum-evaporated sexithiophene films," *Advanced Materials*, vol. 5, no. 6, pp. 461–464, 1993.
- [275] H.-J. Egelhaaf, P. Bäuerle, K. Rauer, V. Hoffmann, and D. Oelkrug, "Uv/vis and ir spectroscopic studies on molecular orientation in ultrathin films of polythiophene model compounds," *Journal of Molecular Structure*, vol. 293, pp. 249–252, 1993.

- [276] P. Lang, G. Horowitz, P. Valat, F. Garnier, J. Wittmann, and B. Lotz, “Spectroscopic evidence for a substrate dependent orientation of sexithiophene thin films deposited onto oriented ptfe,” *The Journal of Physical Chemistry B*, vol. 101, no. 41, pp. 8204–8211, 1997.
- [277] E. Da Como, M. A. Loi, M. Murgia, R. Zamboni, and M. Muccini, “J-aggregation in α -sexithiophene submonolayer films on silicon dioxide,” *Journal of the American Chemical Society*, vol. 128, no. 13, pp. 4277–4281, 2006.
- [278] P. A. Lane, M. Liess, Z. V. Vardeny, J. Partee, B. Uhlhorn, J. Shinar, M. Ibrahim, and A. J. Frank, “Optical studies of ordered and disordered alpha-sexithiophene films,” in *Optical Probes of Conjugated Polymers*, vol. 3145. SPIE, 1997, pp. 475–482.
- [279] B. Reisz, S. Weimer, R. Banerjee, C. Zeiser, C. Lorch, G. Duva, J. Dieterle, K. Yonezawa, J. P. Yang, N. Ueno, S. Kera, A. Hinderhofer, A. Gerlach, and F. Schreiber, “Structural, optical, and electronic characterization of perfluorinated sexithiophene films and mixed films with sexithiophene,” *Journal of Materials Research*, vol. 32, no. 10, pp. 1908–1920, 2017.
- [280] C. Simbrunner, F. Quochi, G. Hernandez-/Sosa, M. Oehzelt, R. Resel, G. Hesser, M. Arndt, M. Saba, A. Mura, G. Bongiovanni, and H. Sitter, “Organic-/organic heteroepitaxy of red-//, green-/, and blue-/emitting nanofibers,” *ACS Nano*, vol. 4, no. 10, pp. 6244–6250, 2010.
- [281] K. Kreger, H.-W. Schmidt, and R. Hildner, “Tailoring the excited-state energy landscape in supramolecular nanostructures,” *Electronic Structure*, vol. 3, no. 2, p. 023001, 2021.
- [282] H. Yamagata, C. M. Pochas, and F. C. Spano, “Designing J- and H-Aggregates through Wave Function Overlap Engineering: Applications to Poly(3-hexylthiophene),” *The Journal of Physical Chemistry B*, vol. 116, no. 49, pp. 14 494–14 503, 2012.
- [283] T. Eder, T. Stangl, M. Gmelch, K. Remmerssen, D. Laux, S. Höger, J. M. Lupton, and J. Vogelsang, “Switching between h- and j-type electronic coupling in single conjugated polymer aggregates,” *Nature Communications*, vol. 8, no. 1, p. 1641, 2017.
- [284] D. Fichou, “Structural order in conjugated oligothiophenes and its implications on opto-electronic devices,” *Journal of Materials Chemistry*, vol. 10, no. 3, pp. 571–588, 2000.
- [285] P. Bäuerle, T. Fischer, B. Bidlingmeier, J. P. Rabe, and A. Stabel, “Oligothiophenes—yet longer? synthesis, characterization, and scanning tunneling microscopy images of homologous, isomerically pure oligo (alkylthiophene) s,” *Angewandte Chemie International Edition in English*, vol. 34, no. 3, pp. 303–307, 1995.

- [286] M. Melucci, M. Gazzano, G. Barbarella, M. Cavallini, F. Biscarini, P. Maccagnani, and P. Ostojica, "Multiscale self-organization of the organic semiconductor α -quinquethiophene," *Journal of the American Chemical Society*, vol. 125, no. 34, pp. 10 266–10 274, 2003.
- [287] P. Wolfer, C. Müller, P. Smith, M. A. Baklar, and N. Stingelin-Stutzmann, " α -quaterthiophene–polyethylene blends: Phase behaviour and electronic properties," *Synthetic metals*, vol. 157, no. 21, pp. 827–833, 2007.
- [288] D. A. Stanfield, Y. Wu, S. H. Tolbert, and B. J. Schwartz, "[Controlling the formation of charge transfer complexes in chemically doped semiconducting polymers](#)," *Chemistry of Materials*, vol. 33, no. 7, pp. 2343–2356, 2021.
- [289] M. Comin, V. Lemaur, A. Giunchi, D. Beljonne, X. Blase, and G. d'Avino, "Doping of semicrystalline conjugated polymers: dopants within alkyl chains do it better," *Journal of Materials Chemistry C*, vol. 10, no. 37, pp. 13 815–13 825, 2022.
- [290] J. Li, I. Duchemin, O. M. Roscioni, P. Friederich, M. Anderson, E. Da Como, G. Kociok-Köhn, W. Wenzel, C. Zannoni, D. Beljonne *et al.*, "Host dependence of the electron affinity of molecular dopants," *Materials Horizons*, vol. 6, no. 1, pp. 107–114, 2019.
- [291] A. Hamidi-Sakr, L. Biniek, J.-L. Bantignies, D. Maurin, L. Herrmann, N. Leclerc, P. Lévêque, V. Vijayakumar, N. Zimmermann, and M. Brinkmann, "[A versatile method to fabricate highly in-plane aligned conducting polymer films with anisotropic charge transport and thermoelectric properties: The key role of alkyl side chain layers on the doping mechanism](#)," *Advanced Functional Materials*, vol. 27, no. 25, p. 1700173, 2017.
- [292] E. M. Thomas, E. C. Davidson, R. Katsumata, R. A. Segalman, and M. L. Chabinyc, "[Branched side chains govern counterion position and doping mechanism in conjugated polythiophenes](#)," *ACS Macro Letters*, vol. 7, pp. 1492–1497, 2018.
- [293] S. Nagamatsu and S. S. Pandey, "[Ordered arrangement of f4tcnq anions in three-dimensionally oriented p3ht thin films](#)," *Scientific Reports*, vol. 10, no. 1, p. 20020, 2020.
- [294] S. S. Zade and M. Bendikov, "[From oligomers to polymer: Convergence in the homo-lumo gaps of conjugated oligomers](#)," *Organic Letters*, vol. 8, pp. 5243–5246, 2006.
- [295] A. Facchetti, M.-H. Yoon, C. L. Stern, G. R. Hutchison, M. A. Ratner, and T. J. Marks, "Building blocks for n-type molecular and polymeric electronics. perfluoroalkyl-versus alkyl-functionalized ligothiophenes (nts; n=2-6). systematic synthesis, spectroscopy, electrochemistry, and solid-state organization," *Journal of the American Chemical Society*, vol. 126, pp. 13 480–13 501, 2004.

- [296] J. A. Van Haare, E. E. Havinga, J. L. Van Dongen, R. A. Janssen, J. Cornil, and J.-L. Brédas, "Redox states of long oligothiophenes: two polarons on a single chain," *Chemistry—A European Journal*, vol. 4, no. 8, pp. 1509–1522, 1998.
- [297] W. Salaneck, O. Inganäs, J.-O. Nilsson, J.-E. Österholm, B. Thémans, and J.-L. Brédas, "Thermochromism in the poly(3-alkylthiophene)s: A study of conformational defects by photoelectron spectroscopy," *Synthetic Metals*, vol. 28, pp. 451–460, 1989.
- [298] A. M. Valencia and C. Cocchi, "Electronic and optical properties of oligothiophene-f4tcnq charge-transfer complexes: The role of the donor conjugation length," *Journal of Physical Chemistry C*, vol. 123, pp. 9617–9623, 2019.
- [299] D. A. Dixon, J. C. Calabrese, and J. S. Miller, "Crystal and molecular structure of the 2: 1 charge-transfer salt of decamethylferrocene and perfluoro-7, 7, 8, 8-tetracyano-p-quinodimethane:[[fe (c5me5) 2]+. cntdot.] 2 [tcnqf4] 2-. the electronic structure of [tcnqf4] n (n= 0, 1-, 2-)," *The Journal of Physical Chemistry*, vol. 93, no. 6, pp. 2284–2291, 1989.
- [300] J. Torrance, J. Mayerle, K. Bechgaard, B. Silverman, and Y. Tomkiewicz, "Comparison of two isostructural organic compounds, one metallic and the other insulating," *Physical Review B*, vol. 22, no. 10, p. 4960, 1980.
- [301] G. Heimel, "The Optical Signature of Charges in Conjugated Polymers," *ACS Central Science*, vol. 2, pp. 309–315, 2016.
- [302] H. Méndez, G. Heimel, A. Opitz, K. Sauer, P. Barkowski, M. Oehzelt, J. Soeda, T. Okamoto, J. Takeya, J.-B. Arlin, J.-Y. Balandier, Y. Geerts, N. Koch, and I. Salzmann, "Doping of Organic Semiconductors: Impact of Dopant Strength and Electronic Coupling," *Angewandte Chemie International Edition*, vol. 52, pp. 7751–7755, 2013.
- [303] J. S. Chappell, A. N. Bloch, W. A. Bryden, M. Maxfield, T. O. Poehler, and D. O. Cowan, "Degree of charge transfer in organic conductors by infrared absorption spectroscopy," *Journal of the American Chemical Society*, vol. 103, pp. 2442–2443, 1981.
- [304] F. Ghani, A. Opitz, P. Pingel, G. Heimel, I. Salzmann, J. Frisch, D. Neher, A. Tsami, U. Scherf, and N. Koch, "Charge transfer in and conductivity of molecularly doped thiophene-based copolymers," *Journal of Polymer Science Part B: Polymer Physics*, vol. 53, pp. 58–63, 2015.
- [305] S. Duhm, I. Salzmann, B. Broker, H. Glowatzki, R. L. Johnson, and N. Koch, "Interdiffusion of molecular acceptors through organic layers to metal substrates mimics doping-related energy level shifts," *Applied Physics Letters*, vol. 95, no. 9, p. 093305, 2009.

- [306] G. C. Welch, R. Coffin, J. Peet, and G. C. Bazan, “[Band gap control in conjugated oligomers via lewis acids](#),” *Journal of the American Chemical Society*, vol. 131, no. 31, p. 10802, 2009.
- [307] G. C. Welch and G. C. Bazan, “[Lewis acid adducts of narrow band gap conjugated polymers](#),” *Journal of the American Chemical Society*, vol. 133, no. 12, pp. 4632–4644, 2011.
- [308] P. Pingel, M. Arvind, L. Kölln, R. Steyrlleuthner, F. Kraffert, J. Behrends, S. Janietz, and D. Neher, “[p-type doping of poly\(3-hexylthiophene\) with the strong lewis acid tris\(pentafluorophenyl\)borane](#),” *Advanced Electronic Materials*, vol. 2, no. 10, pp. 1600204–n/a, 2016.
- [309] K. Kanai, K. Akaike, K. Koyasu, K. Sakai, T. Nishi, Y. Kamizuru, T. Nishi, Y. Ouchi, and K. Seki, “[Determination of electron affinity of electron accepting molecules](#),” *Applied Physics A*, vol. 95, pp. 309–313, 2009.
- [310] P. Zalar, M. Kuik, Z. B. Henson, C. Woellner, Y. Zhang, A. Sharenko, G. C. Bazan, and T.-Q. Nguyen, “[Increased mobility induced by addition of a lewis acid to a lewis basic conjugated polymer](#),” *Advanced Materials*, vol. 26, no. 5, pp. 724–727, 2014.
- [311] B. Yurash, D. X. Cao, V. V. Brus, D. Leifert, M. Wang, A. Dixon, M. Seifrid, A. E. Mansour, D. Lungwitz, T. Liu, P. J. Santiago, K. R. Graham, N. Koch, G. C. Bazan, and T.-Q. Nguyen, “[Towards understanding the doping mechanism of organic semiconductors by lewis acids](#),” *Nature Materials*, vol. 18, no. 12, pp. 1327–1334, 2019.
- [312] P. S. Marqués, G. Londi, B. Yurash, T.-Q. Nguyen, S. Barlow, S. R. Marder, and D. Beljonne, “[Understanding how lewis acids dope organic semiconductors: a “complex” story](#),” *Chemical Science*, vol. 12, no. 20, pp. 7012–7022, 2021.
- [313] C. W. Tang and S. A. VanSlyke, “[Organic electroluminescent diodes](#),” *Applied Physics Letters*, vol. 51, pp. 913–915, 1987.

Appendix A

Chemical Structures of Supplementary Materials

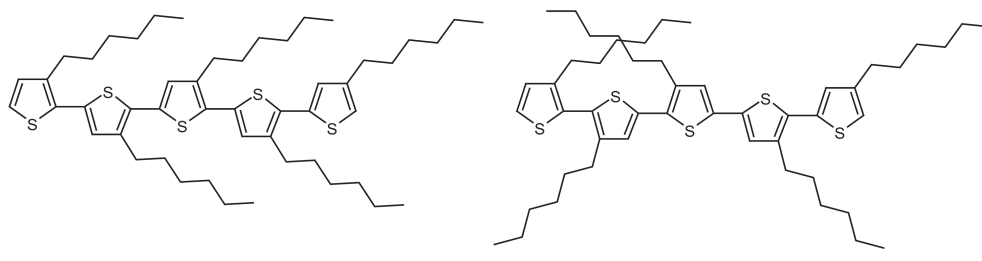


Figure A.1: Chemical structure of [left] regioregular P3HT versus [right] regiorandom P3HT.

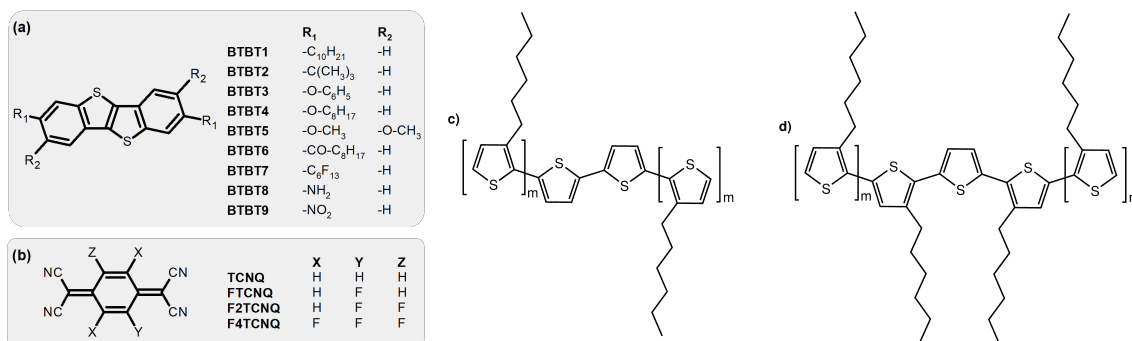


Figure A.2: Sketetal structure of (a) benzothieno[3,2-b][1]benzothiophene (BTBT) derivatives, (b) p-dopant 7,7,8,8-tetracyanoquinodimethane (TCNQ) and its flourinated derivatives (FxTCNQ), (c) hexylated oligothiophenes (HxT) with even number of thiophene repeat units, with $m=1$ to 4, (d) hexylated oligothiophenes (HxT) with odd number of thiophene repeat units, with $m=1$ to 4.

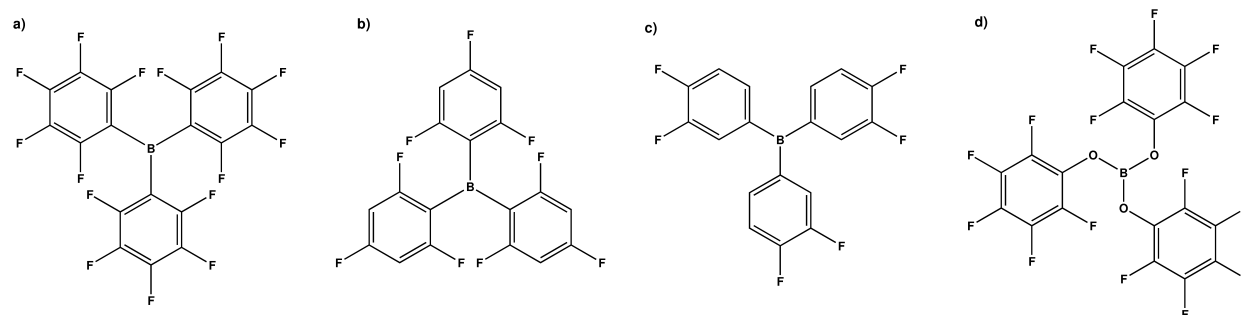


Figure A.3: Skeletal structure of a series of Lewis acids, (a) tris(pentafluorophenyl)borane (BCF), (b) tris(trifluorophenyl)borane (BC₃F), (c) tris(diafluorophenyl)borane (BC₂F) and (d) tris(pentafluorophenyl)borate (BCOF)